Zur Theorie der Lichtausbreitung und Spin-Optik in Halbleitern

Dissertation

zur
Erlangung des Doktorgrades
der Naturwissenschaften
(Dr. rer. nat.)

dem Fachbereich Physik
der Philipps-Universität Marburg
vorgelegt

von

HANS CHRISTIAN SCHNEIDER
aus Kirchheim/Wstr.

Marburg/Lahn 1999

Vom Fachbereich Physik der Philipps-Universität Marburg
als Dissertation am 13.01.2000 angenommen.

Erstgutachter: Prof. Dr. S. W. Koch
Zweitgutachter: Prof. Dr. W. W. Rühle

Tag der mündlichen Prüfung: 17.01.2000

Zusammenfassung

Die Wechselwirkung von Halbleitern mit elektromagnetischen Feldern ist seit mehreren Jahrzehnten Gegenstand intensiver theoretischer und experimenteller Grundlagenforschung. Das Hauptgewicht der Untersuchung von Halbleitern als „passive“ Materialien mit Hilfe optischer Methoden lag dabei lange Zeit auf der Bestimmung von intrinsischen Materialeigenschaften. Mit der Entwicklung immer besserer Technologien zur Herstellung von Halbleiterstrukturen hat sich dieses Gewicht auf die Untersuchung von speziell ausgelegten Proben verschoben, mit denen man maßgeschneiderte optische Eigenschaften erzielen möchte. Im Gegensatz zu diesem passiven Verhalten hat die Bedeutung von Halbleiterstrukturen als „aktives“ Material in Halbleiterlasern stark zugenommen, da Halbleiterlaser und mit ihnen die optische Kommunikation eine immer weitere Verbreitung finden.

Die vorliegende Arbeit behandelt sowohl einen passiven als auch einen aktiven Aspekt der Wechselwirkung von Halbleitern mit dem Lichtfeld. Der beherrschende Einfluß dieser Kopplung wird dabei einheitlich durch Kohärenzen beschrieben, die von äußeren Feldern im Material erzeugt werden.

Polariton-Propagation mit räumlicher Dispersion

Im ersten Teil der Arbeit wird eines der konzeptionell einfachsten und dabei wichtigsten Probleme der Halbleiteroptik aufgegriffen: die Lichtausbreitung. Es spielt ja keine Rolle, ob man bei einem optischen Experiment an den intrinsischen Materialeigenschaften oder den durch Herstellungsprozesse veränderbaren Eigenschaften interessiert ist; es ist immer von Bedeutung, welche Rückschlüsse auf die untersuchte Probe durch die Wechselwirkung mit dem Lichtfeld möglich sind. Schon im Fall sehr schwacher Lichtinsitäten ist die Untersuchung der Licht-Materie-Wechselwirkung und Bestimmung des transmittierten und reflektierten Signals außerhalb der Probe aus den Probeneigenschaften theoretisch sehr kompliziert.[1–4] Auch experimentell ergeben sich dabei erhebliche Schwierigkeiten, zu wirklich aussagekräftigen Resultaten zu gelangen.

Theoretisch rührt diese Komplexität daher, daß die Dynamik der Polarisation, die durch das elektromagnetische Feld im Halbleiter angeregt wird, durch Exzi-

tonen bestimmt wird, d. h. durch Paarzustände aus Elektronen und Löchern, die über die Coulomb-Wechselwirkung korreliert sind.[5] Solche Elektron-Loch-Paare, die den Zuständen des Wasserstoff-Atoms entsprechen, können nun mit dem Lichtfeld Impuls austauschen, und deshalb breitet sich das Licht im Material unter ständigem Austausch mit der Materialpolarisation aus. Für dieses Wechselspiel wurde von Hopfield[6] das Wort „Polariton" geprägt. Die eigentliche Schwierigkeit besteht nun darin, daß die exzitonischen Bindungszustände durch die Anwesenheit der Materialoberflächen verändert werden und dann nicht mehr Wasserstoff-ähnlich sind. Man muß also zur theoretischen Beschreibung die komplizierte Wechselwirkung zwischen dem *makroskopischen* Lichtfeld und den *mikroskopischen* Elektron-Loch-Zuständen inklusive der Kopplung von Elektronen und Löchern über das Coulomb-Potential behandeln. Dieses Problem ist seit über 40 Jahren bekannt und wurde bisher nur im Rahmen von Näherungen oder Vereinfachungen behandelt. Die vorliegende Arbeit stellt die erste Lösung des gesamten mikroskopischen Selbstkonsistenz-Problems dar.

Auf Grund der experimentellen Schwierigkeiten, die Kopplung der Polarisation im Material und dem Lichtfeld im Detail zu studieren, waren die experimentellen Untersuchungen zu diesem Problem lange Zeit wenig aussagekräftig. Erst im letzten Jahr konnten hier Ergebnisse[7] erzielt werden, die deutliche Abweichungen von den Erwartungen brachten, die man auf Grund der bestehenden, näherungsweisen Behandlungen des Polariton-Problems hegte. Die neuen experimentellen Resultate konnten mit Hilfe der hier vorgestellten Theorie eindeutig und quantitativ als polaritonische Effekte erklärt werden.

Die oben erwähnten Näherungslösungen haben wegen ihrer vergleichsweise einfachen Handhabung eine weite Verbreitung gefunden. Allerdings existieren nach der erstmaligen Einführung einer solchen Näherung durch Pekar[8] 1957 verschiedene ähnliche Ansätze, die mit sog. zusätzlichen Randbedingungen (Additional Boundary Conditions, oder ABC im Englischen) arbeiten, aber zu widersprüchlichen Ergebnissen führen. Eine aktuelle theoretische Arbeit[9] von K. Henneberger hat erneut die fehlenden mikroskopischen Grundlagen der ABC-Näherungen betont und eine neue Näherung vorgeschlagen, was zu einer lebhaften Debatte in Fachzeitschriften führte. Da die hier vorgestellte Theorie das Polariton-Problem vollständig mikroskopisch löst, können mit ihrer Hilfe zum ersten Mal die verschiedenen Näherungsverfahren kontrolliert theoretisch untersucht und verglichen werden. Dies wird nach einer kurzen Vorstellung der ABC-Näherungen und des Henneberger-Zuganges in der vorliegenden Arbeit ebenfalls durchgeführt. Als Resultat ergibt sich zum Beispiel, daß für Materialparameter, die dünne GaAs-Volumenmaterialien beschreiben, keine der Näherungen die Ergebnisse der mikroskopischen Theorie reproduzieren kann. Die Näherung von Pekar gibt dabei qualitativ immer bessere Übereinstimmung als die ABC von Ting et al.[10] und der Henneberger-Zugang.

Über das Polariton-Problem hinaus, für das die mikroskopische Theorie ausgearbeitet wurde, kann sie ohne Veränderung ebenfalls auf aktuelle Probleme im Zusammenhang mit resonantem Tunneln[11] durch Halbleiterstrukturen angewandt werden.

Spin-Dynamik im Magnetfeld

Die theoretische Untersuchung der Polarisation wie hier vorgestellt benutzt als wesentliche Größe die mikroskopische Kohärenz zwischen Elektronen und Löchern, die durch das Lichtfeld induziert wird. Eine solche Kohärenz kann auch zwischen energetisch entarteten Elektronenbändern durch ein *transversales* Magnetfeld erzeugt werden, da dieses am magnetischen Moment der Elektronen angreift, das mit dem Spin verknüpft ist. Diese kohärente Kopplung der Elektronenbänder mit unterschiedlichem Spin wird im zweiten Teil der Arbeit mit Hilfe der elektronischen Kohärenz untersucht. Obwohl die theoretische Betrachtungsweise der elektronischen Kohärenz sehr ähnlich der Elektron-Loch-Kohärenz ist, die vom Lichtfeld getrieben wird, sind die experimentellen und technologischen Realisierungen sehr unterschiedlich. Dies ist dadurch bedingt, daß das Lichtfeld Elektronen vom Valenz- ins Leitungsband anregt, während das Magnetfeld rein elektronische Übergänge zwischen Zuständen mit verschiedenen Spins induziert.

Als erste Anwendung der Theorie wird ein neuartiges Experiment analysiert, das die Proportionalität zwischen Spin und magnetischem Moment der Elektronen zu untersuchen erlaubt. Dieser Proportionalitätsfaktor, der Landé-Faktor, ist für Elektronen in Festkörpern nämlich keine Naturkonstante wie für das Elektron im Vakuum, sondern probenabhängig, d. h. der Landé-Faktor wird durch die verwendete Materialzusammensetzung und die Probengeometrie bestimmt, wobei sich für verschieden Probengeometrien sogar verschiedene Vorzeichen des Landé Faktors ergeben. Zur Messung dieses Vorfaktors, dessen Bestimmung bisher große Schwierigkeiten bereitet hat, wurde eine neue Methode[12] entwickelt, die ein transversales Magnetfeld benutzt und sich die optischen Auswahlregeln im Halbleitermaterial zunutze macht. Für dieses Experiment wurden die Anregungsbedingungen und die Spin-Dynamik bestimmt, die sich in der Lumineszenz der Probe niederschlägt und damit für den Landé-Faktor eine direkte Bestimmung des Vorzeichens ermöglicht.

Wie oben schon angedeutet, erlauben die elektronischen Übergänge, die durch das Magnetfeld induziert werden, eine Anwendung als Kontrollmechanismus für elektronische Spins. Da die Elektronen mit Löchern rekombinieren können und dabei Licht einer definierten Polarisation aussenden, kann die quantenmechanische Dynamik der Spins im Magnetfeld auf diese Weise in der makroskopischen Lichtemission von Halbleitern sichtbar gemacht werden. Für diesen Zweck

sind Halbleiter-Mikrolaser, wie in Abbildung 5.1 schematisch dargestellt, besonders geeignet. Die Resonatorlänge dieser Laser beträgt typischerweise nur wenige Mikrometer, so daß nur eine longitudinale Resonatormode im Spektralbereich liegt, in dem optische Verstärkung durch das aktive Material, das aus Halbleiter-Quantenfilmen besteht, erreicht werden kann. Die Lichtemission aus diesen Bauteilen ist dabei senkrecht zu den aktiven Quantenfilmen, so daß das elektromagnetische Feld im Resonator nur auf einer viel kürzeren Distanz mit dem aktiven Material überlappt, als dies bei herkömmlichen Halbleiterlasern der Fall ist. Aus diesem Grund müssen die Spiegel besonders hohe Reflektivitäten aufweisen, damit trotz der dünnen aktiven Schicht die optische Verstärkung für die Laseremission ausreicht. Diese hohen Resonatorgüten werden erreicht durch die Verwendung von Bragg-Spiegeln (distributed Bragg-reflectors, oder DBR im Englischen), deren Reflektivitäten mehr als 99.9% im Spektralbereich um die Resonatorresonanz betragen können. Wegen des Einmodenbetriebs und der hohen Resonatorgüte reagieren diese Laser besonders empfindlich auf die Ladungsträgerdynamik im aktiven Material, die mit dem transversalen Magnetfeld beeinflußt wird.

Mit Hilfe dieser Mikrolaser kann so das quantenmechanische Phänomen der Spin-Dynamik makroskopisch als *Modulation* der Lichtemission sichtbar gemacht werden. Dieser Effekt ist nicht nur von grundlegender, sondern auch von technologischer Bedeutung, da solche Laser wichtige Anwendungen in optischen Netzwerken und als zweidimensionale Anordnungen in Displays finden. In beiden Fällen kommt der schnellen Modulation der Laseremission entscheidende Bedeutung zu, wobei die hier berechneten Effekte, die im Experiment[13] nachgewiesen wurden, bereits die Modulationsfrequenz übertreffen, die mit herkömmlicher elektrischer Modulation erreichbar ist. Die Physik dieses Modulationseffekts der Laseremission wird in der vorliegenden Arbeit auf der Basis der Spin-Dynamik erklärt, die für diese Anwendung mit einer Lasertheorie für den Mikrolaser verbunden wird.

Contents

1. Introduction

The interaction of semiconductors with electromagnetic fields continues to be a subject of active theoretical and experimental basic research. The investigation of semiconductors as a "passive" material using optical fields is already several decades old. Whereas the emphasis used to be on probing intrinsic material properties it has shifted to the use of optical experiments for the characterization of newly fabricated semiconductor structures whose optical properties are almost entirely determined by their design. On the other hand, the importance of semiconductors used as "active" media in semiconductor lasers has grown tremendously, as semiconductor lasers take over ever more applications in the field of optical communication.

The present work will theoretically discuss two instances of semiconductors used as active and passive material for optical fields. The striking consequences of the coupling of the semiconductor material to external fields is analyzed in both cases using the coherence introduced into the material by the external fields.

Polariton Propagation with Spatial Dispersion

We will first focus on one of the conceptually simplest problems in semiconductor optics: the light propagation through samples with surfaces. Regardless of whether one is interested in determining intrinsic or design properties of semiconductors using optical experiments it is important what information can actually be extracted from the interaction of the optical field with the sample. A very schematic picture of a transmission experiment is shown in figure 1.1. An incident light field propagates through the sample resulting in a transmitted and reflected beam. The question considered here is what we can learn about the semiconducting material and the sample design using such experiments. Even in the case of weak optical pulses the determination of the transmitted and reflected fields from the incident beam presents considerable theoretical difficulties and precision measurements face experimental problems; overviews are presented, for instance, in Refs. 1–4. We will illustrate the theoretical difficulty first by approaching the problem in three steps of increasing complexity. Only the last of these steps is a model suitable to describe real transmission experiments for bulk semiconductors.

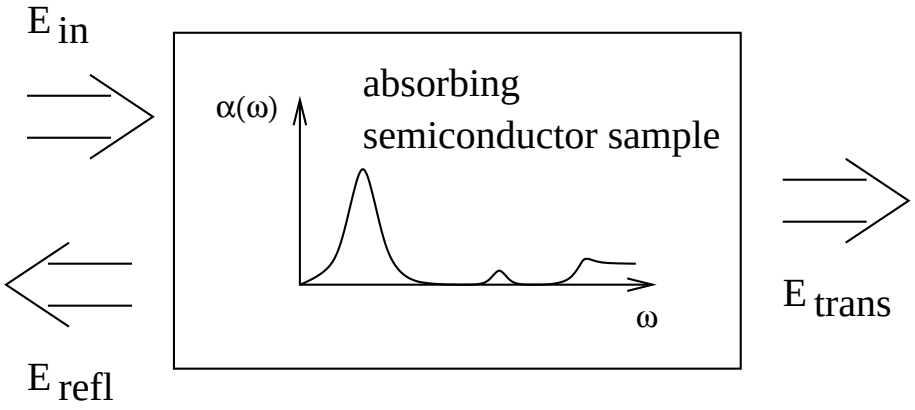

Figure 1.1.: Typical theoretician's view of transmission experiment. The absorption spectrum $\alpha(\omega)$ indicated inside the sample shows the excitonic resonances in an *infinitely extended semiconductor material*.

Since we are concerned here with weak optical fields the polarization induced in the material by the electromagnetic field is formed by excitons, that is, Coulomb-correlated electron-hole states. If we neglect the center-of-mass motion of the electron-hole pairs in the sample, we obtain the well-known absorption spectrum $\alpha(\omega)$, see, e.g., Ref. 5. This is indicated schematically in figure 1.1: The resonances are due to Coulomb-bound electron-hole states, i.e., the excitons, and their absorption lineshapes in a perfect system (without disorder) are Lorentzian.

As a next step we consider spatial dispersion. Generally speaking, spatial dispersion refers to the fact that elementary excitations in the semiconducting material can exchange momentum with the electromagnetic field, that is, both the excitation and the electromagnetic field interact with each other and propagate inside the semiconductor. *If no surfaces are present* the excitonic states are unchanged and still like hydrogen-atom states, only the center-of-mass degree of freedom exchanges momentum with the optical field.* Hopfield introduced the name polariton[6] for this interplay of the light field coupled to its excitonic polarization, both of which propagate through the infinitely extended material.

As the last step, the actual complication is introduced when one analyzes spatial dispersion in a *bounded* sample. Then the surfaces influence the formation of the *microscopic* excitonic states and the picture of an exciton moving with a center-of-mass momentum is no longer valid. Instead the complicated coupling between macroscopic optical field and microscopic electron-hole states in the presence of surfaces and Coulomb interaction has to be solved self-consistently. Excepting the approach presented here, the full microscopic self-consistency prob-

*The mathematical details of this argument which allow an analytical solution are reviewed in chapter 3.

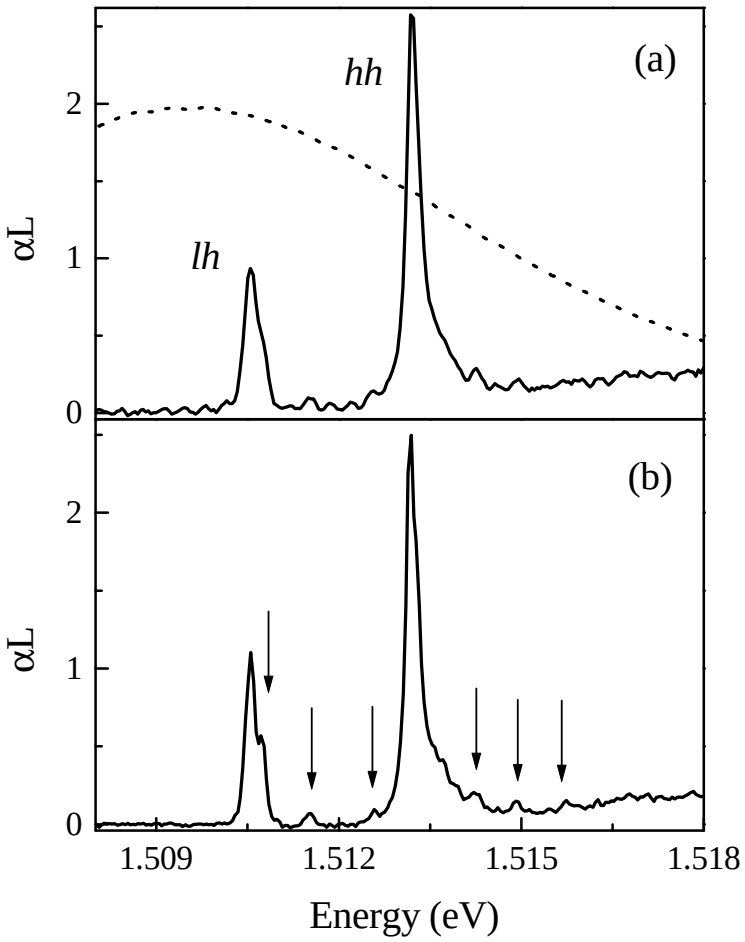

Figure 1.2.: Experimental absorption spectra[14] before (a) and after (b) anti-reflection coating together with the excitation pulse spectrum (dotted line), calculated from the measured intensity transmission spectrum $T(\omega)$ according to $\alpha L \equiv -\log T(\omega)$. The features which emerge in the spectrum after anti-reflection coating are marked by arrows. The light-hole (lh) excitonic resonance lies below the heavy-hole (hh) resonance due to a strain-induced energy shift.

lem, whose exact mathematical statement is contained in chapter 2, has not been solved without further approximations or simplifications.

The investigation of genuine exciton-polariton effects also poses experimental problems if one wishes to observe the details of the coupling between optical field and material polarization because the decay of the excitonic coherence must be small enough to conserve the coherence over the macroscopic lengthscales of the electromagnetic field. If the material quality is not extremely high the dephasing processes are too fast and the polaritonic effects are blurred by the energetic

broadening of the excitonic states. Even for very high-quality samples ultrashort-pulse techniques are required. These conditions are so severe that direct experimental evidence of polariton effects in the transmission spectrum of bulk GaAs remained completely unsatisfactory[15] for a long time. Recent precision measurements, however, have made the investigation of polaritonic effects in GaAs transmission spectra possible. These experiments on a very high-quality bulk GaAs sample yielded drastic deviations from the well-known textbook exciton absorption spectrum.[7] Figure 1.2(b) shows the absorption spectrum obtained from the transmission measured on a sample that was carefully anti-reflection coated. The spectrum differs from the one in figure 1.1 at first sight chiefly by the presence of two excitonic peaks belonging to heavy-hole and light-hole transitions, which are discussed in chapter 2. The important emergent features different from the usual Lorentzian excitonic lineshapes are a double-peak structure on the light-hole resonance together with two high-energy replicas and a clear asymmetry of the heavy-hole resonance together with three replicas.

Attempts to explain these additional structures using approximative treatments did not yield satisfactory results and we have therefore developed a treatment of polariton propagation in semiconductors which is applicable to light propagation through arbitrary semiconductor heterostructures. It solves the polariton problem completely by treating the Coulomb interaction and surfaces on a microscopic footing, as well as describing correctly the coupling between microscopic electron-hole states and macroscopic electromagnetic field. Our theoretical results can quantitatively and unambiguously explain the experimental spectra by polaritonic effects. Moreover, because of the formal simililarity between the Coulomb-bound electron-hole states included in our approach and the correlated electron-hole pairs used in resonant tunneling problems, the theory is also applicable there without modifications.[11]

Approximative treatments as mentioned above have been applied to the polariton problem since Pekar[8] proposed a macroscopic approximation which is now known as Pekar's additional boundary condition.[†] Recently Henneberger[9] stressed again the lack of a microscopic foundation for these approximations and suggested a new macroscopic approach causing a renewed debate[16–18] as to whether a general approximate description of the polariton problem with spatial dispersion can be achieved. Since the theory developed in chapter 2 solves the polariton problem completely all these approaches can be regarded as approximations to the microscopic solution. Therefore the full theory serves also as a measure for the quality of these approximations. We review some of the best-known macroscopic approaches in chapter 3 and compare numerical results obtained in the framework of the various approximative approaches to our microscopic calculation. This allows a critical assessment of the macroscopic approximations.

[†]Additional boundary conditions are discussed in chapter 3.

Spin Dynamics in Magnetic Fields

As will be shown in detail in chapter 2 the key ingredient in the theoretical analysis of propagation effects is the microscopic electron-hole coherence induced by the optical field. The light field drives this coherence via the electric dipole moment and the semiconductor dynamics is dominated by this interaction for the whole range of carrier densities. Such a coherence can also be driven between the two electron bands, but only by a *transverse* magnetic field which couples the carriers via their magnetic dipole moment. This coherent coupling will be analyzed in the second part of this work, also from the point of view of coherence introduced into the system by external fields.

Though the theoretical descriptions of the electron-hole and electron-electron coherences have a lot in common, their experimental and technological realization is very different. Whereas the optical field excites electrons from the valence to the conduction band, the magnetic field interacts with the electrons' magnetic dipole moment, which is connected to their spin, and thus induces electronic transitions from, say, "spin up" to "spin down" states while the electronic energy remains unchanged. For these electron-electron transitions in magnetic fields a microscopic theory is developed here.

To illustrate the theory we first include an application to the analysis of experiments which probe the proportionality between microscopic magnetic moments and electron spin. This relation, the Landé factor, is not a fundamental physical quantity for electrons in semiconductors as it is for the free electron. In semiconductors, it is only a material property which can be strongly influenced by the design of semiconductor heterostructures, even its sign is determined by the specific heterostructure. A new method[12] for the determination of the Landé factor using the selective optical excitation of electronic spins has been developed recently. This approach works particularly well for heterostructures of reduced dimensionality. We use the selection rules for the optical excitation to obtain the initial carrier distributions and determine their dynamics under the influence of the magnetic field. Signatures of this dynamics are visible in the luminescence and make it possible to extract the sign of the Landé factor.

The observation that the magnetic field introduces transitions between electron bands already suggests that the magnetic field can also work as a control mechanism for electron spins. Since the electrons can undergo optical recombination with a specific light polarization the dynamics of the quantum-mechanical spin degree of freedom can be transferred to the macroscopic emission of electromagnetic fields. For this purpose, semiconductor microlasers are especially well suited. The cavity lengths of these lasers are very small, typically only a few micrometers, so that only one longitudinal laser mode can experience optical gain from the active material which is formed by one or several quantum wells in the cavity. Furthermore, the emission direction is perpendicular to the quantum-

well plane so that the electromagnetic field in the cavity only overlaps with the quantum wells over a much shorter distance than in conventional semiconductor lasers. Therefore mirrors with very high reflectivities are needed in order to achieve laser action. These are provided by the distributed Bragg reflectors which reach reflectivities of more than 99.9% in a spectral region ("stop band") around the cavity resonance. Because of the single longitudinal-mode operation and the high cavity quality the light emission of the semiconductor microlaser is very sensitive to the carrier dynamics in the active material, and a modulation of their output can be achieved from the carrier dynamics in magnetic fields. In addition to the visualization of a truely microscopic phenomenon the modulation of microlaser emission has a technological impact since these lasers are used in optical fiber networks and in two-dimensional arrays as displays due to their smallness and emission characteristics.[19] In both these applications the switching of the individual lasers with high frequencies is essential. The modulation calculated here and actually achieved in experiments[13] already exceeds the frequency limit which can be reached with electrical modulation. The physics of this modulation effect for the microlaser emission is explained using the general theoretical description of electron spin dynamics in transverse magnetic fields together with a microlaser theory.

Overview

In chapter 2 the general theory for linear light propagation in semiconductor bulk materials in the presence of surfaces is described. Details about the treatment of the band structure and the numerics of the coupled system of partial differential equations are given in Appendices A and B. Numerical results are used for a detailed discussion of polariton spectra. A comparison to transmission experiments on high-quality GaAs which constitute the first unambiguous evidence of polaritonic effects in the GaAs transmission is also included here. In chapter 3 the assumptions for various ABC schemes are first discussed and a comparison of the full solution with results obtained in the framework of these approximations is presented.

Chapter 4 introduces the microscopic theory of conduction electrons in semiconductors under the influence of transverse magnetic fields. Here, a simplified version of the theory is applied to work out the spin dynamics after optical excitation in a novel geometry. Chapter 5 uses the theory of chapter 4 to model the dynamics of microlasers in transverse magnetic fields. The necessary information about the description of microlasers is gathered in Appendix C.

2. Polariton Propagation

In this chapter we first describe a full solution of the propagation problem for bulk materials with boundaries in the progation direction. On a microscopic level we determine the semiconductor polarization, which is self-consistently coupled to the propagating light field, without phenomenological assumptions other than a dephasing rate. The theory is then applied to a key experiment to prove unambiguously the influence of polaritonic effects in GaAs transmission spectra.

2.1. Microscopic Theory of Polaritons

So far microscopic approaches to the polariton problem have been limited to specific geometries or the full complexity of the problem has been reduced by approximations. Direct calculations of the microscopic polarization coupled to the propagating field have been applied to a half space geometry using a one-dimensional contact interaction instead of the Coulomb interaction between electrons and holes.[20,21] A similiar direct calculation has been carried out for thin samples using an expansion of the polarization in quantum-well envelope functions.[22] Other approaches have used various approximations to construct excitonic wave functions in slab and half-space geometries to obtain the non-local semiconductor response function,[23–25] or have analyzed the half-space problem in wave-vector-space.[26]

In this section we treat the polariton problem by directly solving the coupled equations for the semiconductor polarization and the electromagnetic field. For a derivation of the basic equations for a multi-band semiconductor we start with a discussion of the nonlocal electron-hole amplitude in momentum space and derive its equations of motion. We then turn to a slab geometry, i.e., an electromagnetic field propagating through a material which has surfaces in the direction of propagation but is infinitely extended in the transverse direction.

2.1.1. Momentum-space formulation

The equations of motion for the nonlocal electron-hole polarizations are derived from the non-relativistic many-body Hamiltonian

$$\widehat{H}_{\text{tot}} = \widehat{H}_{\text{kin}} + \widehat{H}_{\text{Coul}} + \widehat{H}_{\text{int}}. \tag{2.1}$$

The operators are expressed using electron and hole band spinor wavefunctions at the zone center ($\mathbf{k} = 0$). Measuring energies from the bottom of the hole band and denoting the band-gap energy by E_{G}, one has for the kinetic part

$$\widehat{H}_{\text{kin}} = \sum_{\mathbf{k},s} [E_G + \varepsilon_{\text{e}}(k)]\, c_s^\dagger(\mathbf{k}) c_s(\mathbf{k}) + \sum_{\mathbf{k},j} \mathscr{H}_{jj'}(\mathbf{k}) c_j^\dagger(\mathbf{k}) c_j(\mathbf{k}). \tag{2.2}$$

Here, s refers to the z component of the electron spin and is used to label the electron bands, which are assumed to be degenerate. Their energy dispersion is described by an effective mass m_{e}^*

$$\varepsilon_{\text{e}}(k_\perp, k_z) = \frac{\hbar^2}{2m_{\text{e}}^*}(k_\perp^2 + k_z^2). \tag{2.3}$$

The hole bands are described by a 4×4 Kohn-Luttinger Hamiltonian $\mathscr{H}$ which is discussed in more detail in Appendix A. The hole states have a total angular momentum quantum number of $J = \frac{3}{2}$; they are labelled by the z component of the angular momentum $j = \pm\frac{3}{2}, \pm\frac{1}{2}$ for all $\mathbf{k}$ values though they are only eigenstates with well-defined angular momentum projection number at the zone center $\mathbf{k} = 0$. The Coulomb Hamiltonian in this basis reads

$$\begin{aligned} \widehat{H}_{\text{Coul}} = \frac{1}{2\mathscr{V}} \sum_{\mathbf{q}\neq 0} V(q) \sum_{\mathbf{k}\mathbf{k}'} \Bigg[& \sum_{ss'} c_s^\dagger(\mathbf{k}+\mathbf{q}) c_{s'}^\dagger(\mathbf{k}'-\mathbf{q}) c_{s'}(\mathbf{k}') c_s(\mathbf{k}) \\ & + \sum_{jj'} c_j^\dagger(\mathbf{k}+\mathbf{q}) c_{j'}^\dagger(\mathbf{k}'-\mathbf{q}) c_{j'}(\mathbf{k}') c_j(\mathbf{k}) \\ & - 2\sum_{sj} c_s^\dagger(\mathbf{k}+\mathbf{q}) c_j^\dagger(\mathbf{k}'-\mathbf{q}) c_j(\mathbf{k}') c_s(\mathbf{k}) \Bigg] \end{aligned} \tag{2.4}$$

with the quantization volume $\mathscr{V}$ and the 3D Coulomb potential in momentum space

$$V(q) = \frac{e^2}{\varepsilon_0 n_{\text{bg}}^2} \frac{1}{q^2}. \tag{2.5}$$

We will work here only in the MKS unit system and have included the background refractive index n_{bg} of the semiconducting material. The light-matter interaction Hamiltonian in dipole approximation is given by

$$\widehat{H}_{\mathrm{int}} = \sum_{\mathbf{k}\mathbf{k}'} \sum_{sj} \mathbf{d}_{sj} \cdot \mathbf{E}(\mathbf{k}-\mathbf{k}')\, c_s^\dagger(\mathbf{k}) c_j^\dagger(-\mathbf{k}') + \mathrm{H.\,c.} \tag{2.6}$$

with the dipole matrix elements $\mathbf{d}_{sj}$ for the transition from hole band j to electron band s.

The nonlocal electron-hole transition amplitude is expressed in terms of electron and hole annihilation operators

$$\Psi_{js}(\mathbf{k}_{\mathrm{h}}, \mathbf{k}_{\mathrm{e}}) = \langle c_j(-\mathbf{k}_{\mathrm{h}}) c_s(\mathbf{k}_{\mathrm{e}}) \rangle \,. \tag{2.7}$$

We will use the electron-hole picture throughout this work but we will continue to label the hole band states with the valence band angular momentum j and crystal momentum $\mathbf{k}_{\mathrm{h}}$. The time evolution of the transition amplitude is determined in a time-dependent Hartree-Fock decoupling scheme. In the linear case, the electron-hole transition amplitude is the only dynamical variable which describes the excitation of the semiconductor. We start from the Heisenberg equations of motion for the annihilation operators c_j and c_s to obtain

$$\begin{aligned} i\hbar \frac{\partial}{\partial t} \Psi_{js}(\mathbf{k}_{\mathrm{h}}, \mathbf{k}_{\mathrm{e}}, t) = & \sum_{j'} \mathscr{H}_{jj'}(\mathbf{k}_{\mathrm{h}}) \Psi_{j's}(\mathbf{k}_{\mathrm{h}}, \mathbf{k}_{\mathrm{e}}, t) + [E_{\mathrm{G}} + \varepsilon_{\mathrm{e}}(k_{\mathrm{e}})] \Psi_{js}(\mathbf{k}_{\mathrm{h}}, \mathbf{k}_{\mathrm{e}}, t) \\ & + \frac{1}{\mathscr{V}} \sum_{\mathbf{q}\neq 0} V(q)\, \Psi_{js}(\mathbf{k}_{\mathrm{h}} - \mathbf{q}, \mathbf{k}_{\mathrm{e}} + \mathbf{q}, t) + \mathbf{d}_{sj} \cdot \mathbf{E}(\mathbf{k}_{\mathrm{h}} - \mathbf{k}_{\mathrm{e}}, t) \end{aligned} \tag{2.8}$$

where the dipole matrix element $\mathbf{d}_{sj} \equiv \langle s|\mathbf{d}|j\rangle$ has been assumed to be $\mathbf{k}$ independent. Equation (2.8) combines the nonlocal electron-hole transition amplitude[27] with multiple valence bands.[28]

We wish to study the influence of surfaces extended perpendicular to the direction of propagation and for definiteness we take this direction as the z direction. Therefore, it is assumed in equation (2.8) that the exciting laser field is spatially homogenous in transverse direction, i.e., in the x-y plane. Then we have $\mathbf{E}(\mathbf{k}_{\mathrm{h}} - \mathbf{k}_{\mathrm{e}}) = \mathbf{E}(k_{\mathrm{hz}} - k_{\mathrm{ez}})$ and this homogeneous excitation in the plane perpendicular to the z axis leads to a conserved center-of-mass momentum

$$\mathbf{K}_\perp \equiv \mathbf{k}_{\mathrm{h}\perp} + \mathbf{k}_{\mathrm{e}\perp} = 0 \tag{2.9}$$

in that plane. Consequently,

$$\mathbf{k}_\perp \equiv \frac{m_{\mathrm{e}} \mathbf{k}_{\mathrm{h}\perp} - m_{\mathrm{h}} \mathbf{k}_{\mathrm{e}\perp}}{m_{\mathrm{h}} + m_{\mathrm{e}}} \tag{2.10}$$

can be set

$$\mathbf{k}_\perp = \mathbf{k}_{\mathrm{h}\perp} = -\mathbf{k}_{\mathrm{e}\perp}. \tag{2.11}$$

Hence $\mathbf{K}_\perp$ will be dropped and only the dependence on the relative momentum $\mathbf{k}_\perp$ will be kept as indicated in the transition amplitude $\Psi(\mathbf{k}_\perp; k_\mathrm{h}, k_\mathrm{e})$.

Since the transition amplitude still depends on the two dimensional vector $\mathbf{k}_\perp$, that is on the modulus $k_\perp$ and phase $\phi_\perp$, we analyze the $\phi_\perp$ dependence using the expansion

$$\Psi^{(m)}(k_\perp, k_\mathrm{h}, k_\mathrm{e}) = \frac{1}{2\pi}\int_0^{2\pi} d\phi_\perp\, e^{-im\phi_\perp}\Psi(\mathbf{k}_\perp; k_\mathrm{h}, k_\mathrm{e})\ . \tag{2.12}$$

Then the expansion of equation (2.8) using equation (2.12) becomes

$$\begin{aligned} i\hbar\frac{\partial}{\partial t}\Psi^{(m)}_{js}(k_\perp; k_{\mathrm{hz}}, k_{\mathrm{ez}}) &= \mathbf{d}_{sj}\cdot\mathbf{E}(k_{\mathrm{hz}} - k_{\mathrm{ez}})\,\delta_{m,m'} \\ &+ [E_\mathrm{G} + \varepsilon_\mathrm{e}(k_\perp, k_z)]\Psi^{(m)}_{js}(k_\perp; k_{\mathrm{hz}}, k_{\mathrm{ez}}) + \sum_{j',m'}\mathscr{H}^{(m-m')}_{jj'}(k_\perp, k_z)\Psi^{(m')}_{j's}(k_\perp; k_{\mathrm{hz}}, k_{\mathrm{ez}}) \\ &+ \frac{1}{\mathscr{V}}\sum_{\mathbf{k}'_\perp,\, q_z}\sum_{m'} V_{m,m'}(k_\perp, k'_\perp, q_z)\Psi^{(m')}_{js}(k_\perp; k_{\mathrm{hz}} + q_z, k_{\mathrm{ez}} + q_z) \end{aligned} \tag{2.13}$$

where the Coulomb matrix element is given by

$$V_{m,m'}(k_\perp, k'_\perp, q_z) = \frac{e^2}{\varepsilon_0 n_\mathrm{bg}^2}\int_0^{2\pi} d\phi_\perp \int_0^{2\pi} d\phi'_\perp \frac{e^{-im\phi_\perp}e^{im'\phi'_\perp}}{(\mathbf{k}_\perp - \mathbf{k}'_\perp)^2 + q_z^2}\ . \tag{2.14}$$

Here, the integrand depends on the angular variables through

$$(\mathbf{k}_\perp - \mathbf{k}'_\perp)^2 = k_\perp^2 + k_\perp'^2 - 2k_\perp k'_\perp\cos\phi_\perp. \tag{2.15}$$

By transforming to $\widetilde{\phi} = \phi - \phi'$ it can be seen that the Coulomb potential (2.14) is proportional to $\delta_{m,m'}$. The $m - m'$ components of the $\mathscr{H}_{jj'}$ matrix are determined from equations (A.3)–(A.6). Because of the phase factors only the diagonal terms are proportional to $\delta_{m-m',0}$. The off-diagonal terms, couple m to $m' = m \pm 2$ and $m' = m \pm 1$, respectively. Because neither the driving term nor the Coulomb potential couple different ms, only the $m = 0$ components of the transition amplitudes are appreciable when the system is driven by a weak electric field.[29] Therefore the $m \neq 0$ components can be neglected to a very good approximation and we will consider only the $m = 0$ coefficient

$$\Psi(k_\perp, k_{\mathrm{hz}}, k_{\mathrm{ez}}) \equiv \Psi^{(0)}(k_\perp; k_{\mathrm{hz}}, k_{\mathrm{ez}}) \tag{2.16}$$

in the following. Since the restriction of the Hamiltonian $\mathscr{H}$ to its $m = m' = 0$ components is *diagonal* in the hole band indices, cf. equation(A.10), the different bands are effectively decoupled.

We assume in the following polarized excitation $\mathbf{E}(\mathbf{r},t) = E(z,t)\boldsymbol{\sigma}_+$. The dipole matrix elements

$$d_{\uparrow,+3/2} = \sqrt{3}d_{\downarrow,+1/2} = -d_{\mathrm{cv}}\boldsymbol{\sigma}_+ \tag{2.17}$$

$$d_{\downarrow,-3/2} = \sqrt{3}d_{\uparrow,-1/2} = d_{\mathrm{cv}}\boldsymbol{\sigma}_- \tag{2.18}$$

then yield that only the $j = -\frac{3}{2} \to s = \downarrow$ and the $j = -\frac{1}{2} \to s = \uparrow$ transitions are driven. We have used here the definition for the complex polarization vectors

$$\boldsymbol{\sigma}_\pm = \frac{1}{\sqrt{2}}(\mathbf{e}_x \pm i\mathbf{e}_y) \tag{2.19}$$

using the real Cartesian basis vectors $\mathbf{e}_x$ and $\mathbf{e}_y$. Therefore only two interband transition amplitudes remain which will be designated by $\nu = \mathrm{HH}$ and $\nu = \mathrm{LH}$, respectively. In particular, we have $\Psi_{\mathrm{LH}} \equiv \Psi_{-\frac{1}{2},\uparrow}$ and $\Psi_{\mathrm{HH}} \equiv \Psi_{-\frac{3}{2},\downarrow}$. The corresponding dipole matrix elements are defined by

$$d_{\mathrm{HH}} = \sqrt{3}d_{\mathrm{LH}} \equiv d_{\mathrm{cv}}\,. \tag{2.20}$$

Therefore we can combine the contributions to the kinetic energy of equation (2.13) into

$$\widetilde{\varepsilon}_{\mathrm{HH}}(k_\perp, k_{\mathrm{ez}}, k_{\mathrm{hz}}) \equiv E_G + \Delta E + \varepsilon_{\mathrm{HH}}(k_\perp, k_z) + \varepsilon_{\mathrm{e}}(k_\perp, k_z), \tag{2.21}$$

$$\widetilde{\varepsilon}_{\mathrm{LH}}(k_\perp, k_{\mathrm{ez}}, k_{\mathrm{hz}}) \equiv E_G - \Delta E + \varepsilon_{\mathrm{LH}}(k_\perp, k_z) + \varepsilon_{\mathrm{e}}(k_\perp, k_z), \tag{2.22}$$

where the anisotropic HH and LH energies and the energy shift ΔE due to strain are the diagonal Elements of $\mathscr{H}^{(0)}$ as given in equation (A.10). They are defined by

$$\varepsilon_\nu(k_\perp, k_z) \equiv \frac{\hbar^2}{2m_{\nu\perp}}k_\perp^2 + \frac{\hbar^2}{2m_{\nu z}}k_z^2 \tag{2.23}$$

cf. equations (A.8) and (A.9), and the isotropic electron dispersion is given in equation (2.3). Note that in equations (2.21) and (2.22) a z dependent band-gap energy can be introduced which allows the modelling of heterostructures.

2.1.2. Real space representation

In z direction the real space dependence is obtained after Fourier transformation in the z_{h} and z_{e} coordinates

$$\Psi_\nu(k_\perp, z_{\mathrm{e}}, z_{\mathrm{h}}) \equiv \int_{-\infty}^{\infty} dk_{\mathrm{h}} \int_{-\infty}^{\infty} dk_{\mathrm{e}}\, e^{ik_{\mathrm{hz}}z_{\mathrm{h}}}\, e^{ik_{\mathrm{ez}}z_{\mathrm{e}}}\, \Psi_\nu(k_\perp; k_{\mathrm{hz}}, k_{\mathrm{ez}}). \tag{2.24}$$

and supplying the appropriate boundary conditions which will be discussed below. The equation of motion for the "wave functions" $\Psi_\nu(k_\perp, z_e, z_h)$

$$\begin{aligned} i\hbar\frac{\partial}{\partial t}\Psi_\nu(k_\perp, z_h, z_e) = &\widetilde{\varepsilon}_\nu(k_\perp, \widehat{k}_{hz}, \widehat{k}_{ez})\Psi_\nu(k_\perp, z_e, z_h) \\ &+ \frac{1}{(2\pi)^2}\int k'_\perp dk'_\perp V(k_\perp, k'_\perp, |z_h - z_e|)\,\Psi_\nu(k'_\perp, z_h, z_e) \\ &+ d_\nu E(z,t)\;\delta(z_h - z_e) \end{aligned} \tag{2.25}$$

where $z = (z_e + z_h)/2$. Here, we have assumed a local dependence of the dipole matrix element on the relative variable $d_{cv}(z_e - z_h) \propto \delta(z_e - z_h)$ because it is localized on a length scale of a few percent of an excitonic Bohr radius.

The Fourier-transformed Coulomb potential is given by

$$V(k_\perp, k'_\perp, |z_h - z_e|) = \frac{e^2}{2\varepsilon_0 n_{bg}^2}\int_0^{2\pi} d\phi_\perp \frac{e^{-|\mathbf{k}_\perp - \mathbf{k}'_\perp||z_h - z_e|}}{|\mathbf{k}_\perp - \mathbf{k}'_\perp|} \tag{2.26}$$

together with equation (2.15) and the sum over $\mathbf{k}_\perp$ with 2D normalization area $\mathscr{A}$ has been replaced by the sum is replaced by an integral according to

$$\frac{1}{\mathscr{A}}\sum_{\mathbf{k}_\perp} \to \frac{1}{(2\pi)^2}\int_0^\infty k_\perp dk_\perp \int_0^{2\pi} d\phi_\perp\,, \tag{2.27}$$

which reduces to the $k_\perp$ integration because all quantities are $\phi_\perp$ independent. The transformation (2.24) also transforms the k_{hz} and k_{ez} dependence of the kinetic energy into differential operators via the replacememts

$$k_z \to \widehat{k}_z = -i\frac{\partial}{\partial z} \tag{2.28}$$

for k_{ez} and k_{hz}, respectively, which gives equation (2.25) the form of a Schrödinger equation. Since we have obtained a differential equation for the electron-hole transition amplitude Ψ a boundary condition must be specified. This is the essential difference to formulations using the macroscopic polarization calculated from the transition amplitude because the macroscopic polarization does not obey a differential equation. In our model calculations we assume

$$\Psi(z_e, z_h) = 0 \qquad \text{for } z_e \text{ or } z_h \text{ on one of the surfaces.} \tag{2.29}$$

More complex heterostructures can easily be handled by including a z dependent band gap energy.

With the definition of the transverse reduced masses

$$\frac{1}{\mu_{\nu\perp}} = \frac{1}{m_{\nu\perp}} + \frac{1}{m_e^*} \tag{2.30}$$

for $\nu =$ LH, HH we obtain

$$\begin{aligned} i\hbar\frac{\partial}{\partial t}\Psi_\nu(k_\perp,z_\mathrm{e},z_\mathrm{h}) = &\left(E_\mathrm{G}\pm\Delta E - i\gamma + \frac{\hbar^2}{2\mu_{\nu\perp}}k_\perp^2\right)\Psi_\nu(k_\perp,z_\mathrm{e},z_\mathrm{h}) \\ &+\left(\frac{\hbar^2}{2m_\mathrm{e}^*}\frac{\partial^2}{\partial z_\mathrm{e}^2}+\frac{\hbar^2}{2m_{\nu z}}\frac{\partial^2}{\partial z_\mathrm{h}^2}\right)\Psi_\nu(k_\perp,z_\mathrm{e},z_\mathrm{h}) \\ &+\frac{1}{(2\pi)^2}\int dk'_\perp k'_\perp\, V_{k_\perp,k'_\perp}(|z_\mathrm{e}-z_\mathrm{h}|)\,\Psi_\nu(k'_\perp,z_\mathrm{e},z_\mathrm{h}) \\ &+d_\nu E(z,t)\,\delta(z_\mathrm{e}-z_\mathrm{h}). \end{aligned} \tag{2.31}$$

for HH and LH parameters, respectively. In equation (2.31) we have also included a phenomenological damping constant γ.

The macroscopic polarization $\mathbf{P}$ is computed by summing the contributions from all transition amplitudes.

$$\mathbf{P}(z) = \sum_{sj}\sum_{\mathbf{k}_\perp} d_{sj}^*\Psi_{js}(\mathbf{k}_\perp,z,z) \tag{2.32}$$

where we have again assumed that the spatial dependence of the dipole matrix element on the relative variable $d_\mathrm{cv}(z_\mathrm{e}-z_\mathrm{h}) \propto \delta(z_\mathrm{e}-z_h)$ is local.

2.1.3. Electromagnetic Field

The evolution of the electromagnetic field will be determined directly from Maxwell's equations

$$\boldsymbol{\nabla}\times\mathbf{B} = \frac{n^2}{c_0^2}\frac{\partial}{\partial t}\mathbf{E} + \frac{1}{\varepsilon_0 c_0^2}\left(\mathbf{J}+\frac{\partial}{\partial t}\mathbf{P}\right) \tag{2.33}$$

$$\boldsymbol{\nabla}\times\mathbf{E} = -\frac{\partial}{\partial t}\mathbf{B} \tag{2.34}$$

and

$$\boldsymbol{\nabla}\cdot\mathbf{B} = 0 \tag{2.35}$$

$$\boldsymbol{\nabla}\cdot(n^2\mathbf{E}) = \rho_\mathrm{free} - \boldsymbol{\nabla}\cdot\mathbf{P}\,. \tag{2.36}$$

Here, c_0 and ε_0 are the vacuum speed of light and the permittivity of the vacuum, respectively. For the case of circularly polarized transverse fields propagating in z direction, $\mathbf{E}(\mathbf{r},t) = E(z,t)\boldsymbol{\sigma}_+$ and $\mathbf{B}(\mathbf{r},t) = B(z,t)\boldsymbol{\sigma}_+$, equations (2.33) and (2.34) lead to

$$n^2(z)\frac{\partial}{\partial t}E(z,t) = -c_0^2\frac{\partial}{\partial z}B(z,t) - \frac{1}{\varepsilon_0}\frac{\partial}{\partial t}P(z,t) - J(z,t), \tag{2.37}$$

$$\frac{\partial}{\partial t}B(z,t) = -\frac{\partial}{\partial z}E(z,t). \tag{2.38}$$

where $n(z)$ is the nonresonant (background) refractive index profile along the propagation direction. Within the homogeneous slab, $n(z) = n_{\mathrm{bg}}$. Also, there are no free charges, $\rho_{\mathrm{free}} \equiv 0$, and equations (2.35) and (2.36) are automatically satisfied in this configuration.

Via the source term in equation (2.37) the electromagnetic field is coupled to the macroscopic polarization $\mathbf{P}(\mathbf{r},t) = P(z,t)\boldsymbol{\sigma}_+$. Using equation (2.32) this can be expressed as

$$P(z,t) = 2\pi \sum_{\nu=\mathrm{LH,HH}} \int_0^\infty dk_\perp k_\perp \, d_\nu^* \Psi_\nu(k_\perp, z, z, t). \tag{2.39}$$

In equation (2.39) we have neglegected nonresonant contributions. The current $J(z,t)$ in equation (2.37) acts as additional source term which is localized outside of the sample. It is introduced in our numerical scheme as a convenient device to generate the external electromagnetic driving field.

Equation (2.31) constitutes a partial integro-differential equation which has to be solved together with equations (2.37) and (2.38) where the coupling is given by equation (2.39). The numerical treatment of these coupled partial differential equations is very involved and is only possible on present-day supercomputers. Details about the approach used here are discussed in Appendix B.

2.2. Experiment

This section is devoted to the analysis of a key experiment conducted in the group of Daniel Chemla (Berkeley) which, for the first time, proves the influence of polariton propagation on GaAs transmission spectra. Since the experiment has several distinctive features and led to close collaboration between experiment and theory, we first review these briefly before turning to the comparison with theoretical results.

The measurements were performed on a very high quality $0.25\,\mu$m thick GaAs layer, clad between a $Al_{0.3}Ga_{0.7}As$ cap layer and a $Al_{0.7}Ga_{0.3}As$ stop-etch layer. In order to allow transmission experiments, the GaAs substrate has been etched and the sample has been anti-reflection (AR) coated on both sides before being mounted on a sapphire disk. The sample was immersed in superfluid He and the transmission was obtained by exciting the system with a 100-fs Ti:sapphire laser. The absorption spectrum at $T = 2\,$K was already introduced in chapter 1 in figure 1.2(a), where also the laser profile (dotted line) is shown. The light-hole/heavy-hole (LH/HH) exciton degeneracy is lifted due to the strain induced by the difference in thermal expansion between the sapphire substrate and the sample itself. Additionally, the transition linewidths are very small (below 0.25

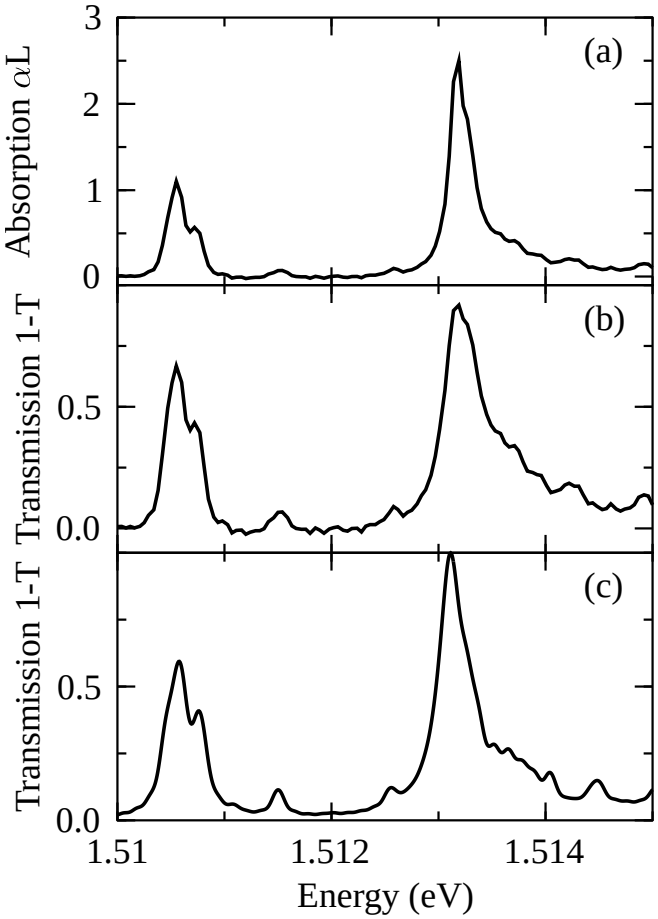

Figure 2.1.: Experimental absorption[14] (a) and transmission (b) spectra for a high-quality 0.25 μm GaAs sample and corresponding calculated transmission spectrum (c).

meV), showing the high quality of the sample. Nevertheless, the sapphire substrate is responsible for the small Fabry-Pérot fringes, which appear close to the base-line of the spectrum in figure 1.2(a). Thus, in a second step, the sapphire substrate was AR-coated, too. For comparison, the absorption spectrum obtained using this technique and with the same excitation conditions as above is displayed in figure 1.2(b). The AR-coating allows the unambiguous resolution of the important features marked by arrows.

Figure 2.1(a–b) and figure 2.2(a) show respectively the retrieved absorption and phase spectra at $T = 2\,\mathrm{K}$ and very low carrier density which were performed using Fourier-transform spectral interferometry, in a Mach-Zender interferometer.[30] In order to allow an easy comparison with other works, we display in

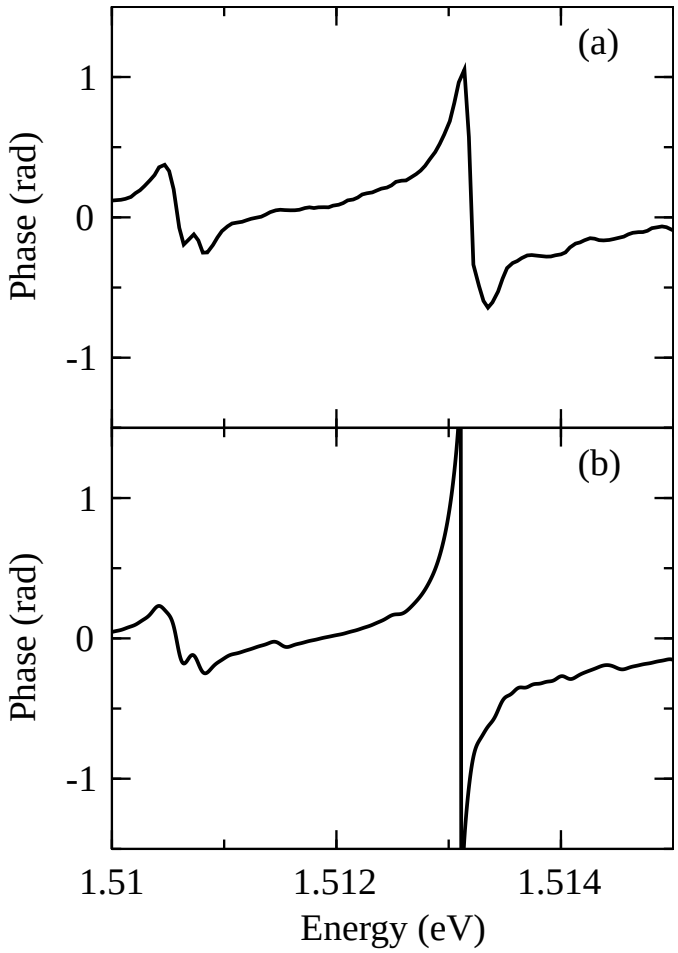

Figure 2.2.: Experimental[14] (a) and calculated (b) phase spectra corresponding to figure 2.1.

figure 2.1(a) the conventional absorption $\alpha(\omega)L = -\log T(\omega)$ calculated from the transmission $T(\omega) = |t(\omega)|^2$ which is given in terms of the incident and transmitted electromagnetic fields by

$$t(\omega) = \frac{E_{\text{trans}}(\omega)}{E_{\text{in}}(\omega)}. \tag{2.40}$$

But in the context of the analysis presented here, the use of $\alpha(\omega)L$ is not physically satisfying since a simple exponential absortion law for the transmitted and incident intensities,

$$I_{\text{trans}}(\omega) = I_{\text{in}}(\omega)e^{-\alpha(\omega)L}, \tag{2.41}$$

is no longer valid. Instead, the comparison presented here is based on the transmission $1 - T(\omega)$, shown in figure 2.1(b), where small features are more pronounced than in the $\alpha(\omega)L$ spectrum.

The high experimental resolution shows that the excitonic lineshapes cannot be described by Lorentzians: the HH transition at 1.5132 eV is asymmetric with a shoulder on the high energy side and the LH transition at 1.5105 eV reveals a clear fine structure. It is split in two components and followed by several reproducible features at higher energy, all of which have a counterpart in the phase spectrum $\phi(\omega)$, figure 2.2(a).

The information contained in the phase $\phi(\omega)$, which also characterizes the optical response of the system, is usually neglected. In a linear absorption experiment and if there are no zeros in the real part of the complex transmission $t(\omega)$, the phase is related to the absorption via a variant of the Kramers-Kronig transformation. However, this relation has to be modified if there are zeros in the real part of $t(\omega)$. In this case, $\phi(\omega)$ is given by

$$\phi(\omega) = \frac{1}{\pi}\,\mathscr{P}\!\int_{-\infty}^{\infty} d\omega'\,\frac{\log|t(\omega')|}{\omega-\omega'} + \sum_i \arg\left(\frac{\omega-\omega_i}{\omega-\omega_i^*}\right) \tag{2.42}$$

where the first term on the right-hand side is a Hilbert transform ($\mathscr{P}$ denotes the principal value) of $\log|t(\omega)|$ which is reminiscent of the usual Kramers-Kronig relation. The second term, related to Blaschke factors in complex analysis,[31] contains the complex zeros of $|t(\omega)|$ at ω_i. These contributions are expected to occur for stronger absorption or thicker samples than in the case discussed presently.

Generally, a mere computation of the phase spectrum through the Hilbert transform of the absorption data suffers from conceptual as well as practical difficulties. First, it is not possible, in the most general case, to infer the zeros of the real part of $t(\omega)$ from the knowledge of $|t(\omega)|$ alone. Second, the transmission spectrum is always experimentally measured with a finite resolution and within a finite window of frequencies, which results in a loss of resolution and divergence at the boundaries in the computed phase spectrum. Moreover, as will be shown below and in chapter 3, a complete comparison with theoretical models must always include both amplitude and phase spectra.

2.3. Theoretical Results

For a comparison of experimental results we directly apply the theory discussed in section 2.1. The parameters used in the following are collected in Table 2.1. As a phenomenonlogical parameter we only use the dephasing γ which corresponds to a dephasing time $T = 10\,\mathrm{ps}$ and a broadening of $0.06\,\mathrm{meV}$. The dipole matrix element is given by the microscopic position operator matrix element r_{cv} via $d_{\mathrm{cv}} =$

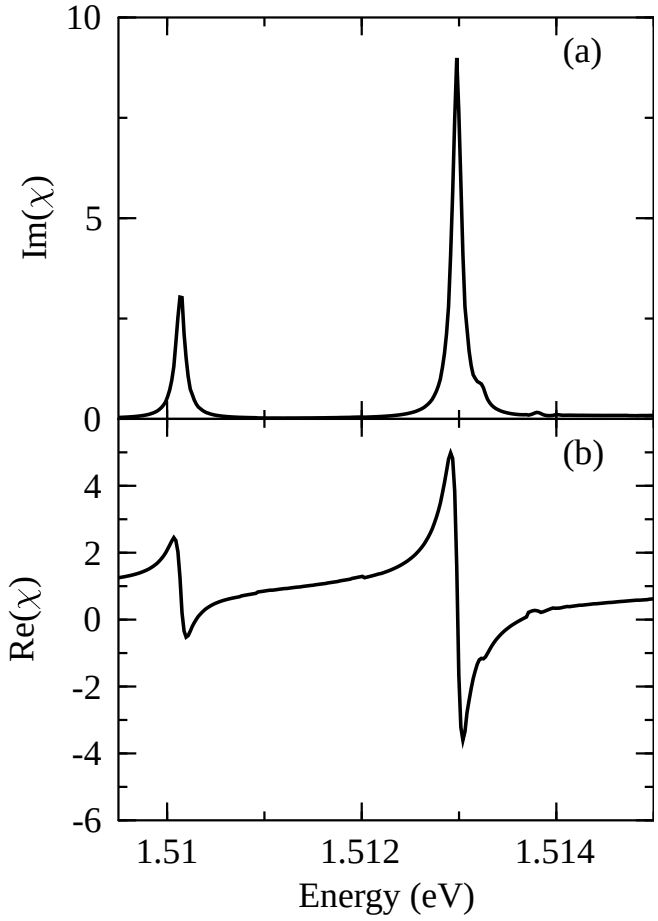

Figure 2.3.: Imaginary (a) and real (b) part of the calculated susceptibility belonging to the transmission and phase spectra in Figs 2.1 and 2.2.

er_{cv} yielding a LT-splitting energy of $\Delta_{LT} = 8\pi r_{cv}^2/a_B^2 E_B = 0.17\,\text{meV}$. The energetic shift of the LH and HH peaks due to strain is read off from the experimental spectrum to be $2\Delta E = 0.6 E_B = 2.4\,\text{meV}$. We include the anti-reflection coating in our model by using the same background refractive index inside and outside of the sample since this suppresses all effects due to Fabry-Pérot resonances.

In figure 2.1 the experimental transmission spectrum (b) is shown together with the calculated result (c). The characteristic splitting of the LH exciton resonance and the asymmetric broadening of the HH exciton line are present in the experiment and in the calculation. Both features can be explained unambigously by the interplay of polaritonic effects and center-of-mass (COM) quantization (small peaks on the high-energy side of the resonances) of the excitonic motion, as discussed in detail in section 3.3. Also, the energetically higher COM replicas for

Symbol	Value	Description
E_B	4.2 meV	excitonic binding energy
a_B	125 Å	excitonic Bohr radius
m_e^*	$0.067\,m_0$	effective electron mass
m_{LHz}	$0.08\,m_0$	LH z mass
$m_{LH\perp}$	$0.23\,m_0$	LH transverse mass
m_{HHz}	$0.53\,m_0$	HH z mass
$m_{HH\perp}$	$0.11\,m_0$	HH transverse mass
n_{bg}	3.61	background refractive index
r_{cv}	5 Å	microscopic dipole coupling
γ	$0.015\,E_B$	phenomenological dephasing

Table 2.1.: GaAs parameters used for numerical computations.

the LH and HH excitonic resonances are present in the experimental and the calculated result. Fig 2.2 shows the measured (a) and calculated (b) phase of the transmitted field. We obtain an excellent overall agreement between the experimental and theoretical results for transmission and phase spectra.

As a next step, we would like to contrast the linear susceptibility spectrum in figure 2.3 with the corresponding transmission and phase spectra shown in Figs. 2.1 and 2.2. One notices first that the energetic shift between both excitonic resonances is almost entirely due to the strain contribution $2\Delta E = 2.4\,\text{meV}$. This is related to the mass reversal, i.e., the fact that the HH has a lighter z mass and the LH a heavier z mass which makes the exciton binding energy very similar for HH and LH excitons. More importantly, in semiconductors one often approximates the intensity absorption coefficient

$$\alpha(\omega) \simeq -\frac{\omega}{n_{bg}c_0}\,\mathrm{Im}\,\chi(\omega) \tag{2.43}$$

from equation (2.41) and the phase change

$$\frac{d\phi}{dz}(\omega) \simeq -\frac{\omega}{2n_{bg}c_0}\,\mathrm{Re}\,\chi(\omega) \tag{2.44}$$

by the imaginary and real parts of the susceptibility. Though these relations can only be obtained in a slowly varying amplitude approximation[32] they often serve as a "rule of thumb" for the absorption and phase changes in situations where they rigorously do not apply. Based on these relations, one would expect in the present case the absorption lineshape to be approximately Lorentzian and the phase spectrum to show a simple anomalous dispersion. But the features like the double-peak structure of the LH and the replicas are completely absent from the susceptibility spectra; thus the approximate equations (2.43) and (2.44) drastically fail to describe polariton propagation.

3. Microscopic Theory vs. ABCs

It has been the subject of a recently renewed debate[9,16–18] how an approximate description of polariton propagation can be obtained using only the expression for the macroscopic polarization of an infinitely extended medium. Since the microscopic excitonic structure, which determines how the macroscopic polarization falls off at the surface, cannot be calculated in such an approach, various assumptions have been proposed to describe the spatial behavior of the polarization near surfaces. The first of these approximations was introduced by Pekar[8] who imposed as an additional boundary condition (ABC) the vanishing of the macroscopic polarization on all surfaces. Pekar's ABC has been subsequently augmented by other parameters, e.g., exciton-free dead layers at the surfaces and surface potentials.[33] The influence of the choice of dead-layer thickness[34] and surface potentials[35] has also been studied.

Attempts have been made to justify macroscopic approaches which lead to contradicting results: Zeyher and co-workers[36,37] conclude that the excitonic polarization should vanish at the surfaces according to Pekar's ABC. With other arguments, Ting et. al.[10] suggest as a new ABC the vanishing polarization flux at surfaces, and a different method has been presented recently.[9]

In the following we first review the simple case of polaritons in homogenous media, where an analytical solution of the propagation problem including spatial dispersion is possible. The separation of excitonic relative and center-of-mass motion is introduced in this context. We then describe some macroscopic approaches which attack the problem by working only with the excitonic center-of-mass motion and compare numerical results obtained from the approximations to our calculations and to experimental data.

3.1. Polaritons in Homogenous Media

For the homogeneous, infinitely extended sample, the solution of the propagation problem can be simplified considerably because it is possible to separate relative and center-of-mass (COM) motion of the excited electron-hole pairs. For better comparison with the general case where this separability is lost, we recall some

facts about the treatment of polariton propagation in homogeneous media briefly.

We start from the equation of motion for the interband-transition amplitude (2.8) in Hartree-Fock approximation. A transformation from electron and hole momenta to spatial coordinates leads to a partial differential equation of the Schrödinger type. For simplicity we assume in the following isotropic electron and hole masses m_e and m_h, respectively. Using relative

$$\boldsymbol{\rho} = \mathbf{r}_\mathrm{e} - \mathbf{r}_\mathrm{h} \tag{3.1}$$

and COM coordinates

$$\mathbf{r} = \frac{m_\mathrm{e}\mathbf{r}_\mathrm{e} + m_\mathrm{h}\mathbf{r}_\mathrm{h}}{m_\mathrm{e} + m_\mathrm{h}} \tag{3.2}$$

one obtains instead of equation (2.8)

$$\left[i\hbar\frac{\partial}{\partial t} - E_\mathrm{G} + \frac{\hbar^2}{2M}\nabla_\mathbf{r}^2 + \frac{\hbar^2}{2\mu}\nabla_{\boldsymbol{\rho}}^2 + V(|\boldsymbol{\rho}|) \right] \Psi(\mathbf{r},\boldsymbol{\rho},t) = \mathbf{d}(\boldsymbol{\rho})\cdot\mathbf{E}(\mathbf{r},t) \tag{3.3}$$

with total mass M and reduced mass μ, respectively. The LHS of equation (3.3) contains Hamiltonians for the excitonic relative and COM motion which define eigenvalue equations

$$H_\mathrm{rel}\,\varphi_i(\boldsymbol{\rho}) = -\left[\frac{\hbar^2}{2\mu}\nabla_{\boldsymbol{\rho}}^2 + V(|\boldsymbol{\rho}|)\right]\varphi_i(\boldsymbol{\rho}) = \varepsilon_i\,\varphi_i(\boldsymbol{\rho}), \tag{3.4}$$

$$H_\mathrm{com}\,\Phi_q(\mathbf{r}) = -\frac{\hbar^2}{2M}\nabla_\mathbf{r}^2\Phi_q(\mathbf{r}) = \hbar\omega_q\,\Phi_q(\mathbf{r}). \tag{3.5}$$

The Wannier equation (3.4) , which contains the Coulomb interaction between electron and hole

$$V(\rho) = \frac{e^2}{4\pi\varepsilon_0 n_\mathrm{bg}^2}\,\frac{1}{\rho}\,, \tag{3.6}$$

describes bound and scattering states with eigenvalues ε_i and eigenfunctions $\varphi_i(\boldsymbol{\rho})$ whereas equation (3.5) leads to plane wave solutions

$$\Phi_\mathbf{q}(\mathbf{r}) = e^{i\mathbf{q}\cdot\mathbf{r}} \tag{3.7}$$

for the COM motion with the energy

$$\hbar\omega_q = \frac{\hbar^2 q^2}{2M}\,. \tag{3.8}$$

The complete set of eigenfunctions can be used to expand the solution of the Schrödinger equation for the combined electron-hole motion, equation (3.3),

$$\Psi(\mathbf{r},\boldsymbol{\rho},t) = \sum_n \int d^3q\, \Psi_{\mathbf{q},n}(t)\, \varphi_i(\boldsymbol{\rho})\, \Phi_{\mathbf{q}}(\mathbf{r}), \tag{3.9}$$

which leads to

$$\left(i\bar{h}\frac{\partial}{\partial t} - \varepsilon_i - \bar{h}\omega_q\right) \Psi_{\mathbf{q},n}(t) = d_i E_{\mathbf{q}}(t). \tag{3.10}$$

Here we have introduced the components of the dipole matrix element

$$d_i = \int d^3\rho\ \varphi_i^*(\boldsymbol{\rho})\, d(\boldsymbol{\rho}) \tag{3.11}$$

and of the optical field

$$E_{\mathbf{q}}(\omega) = \int d^3r\, \Phi_{\mathbf{q}}(\mathbf{r},\omega)\, E(\mathbf{r},\omega) \tag{3.12}$$

interacting with the corresponding excitonic states. The solution of equation (3.10) can be found directly after Fourier-transforming from time to frequency arguments:

$$\Psi_{\mathbf{q},n}(\omega) = \frac{d_i}{\bar{h}\omega - \varepsilon_i - \bar{h}\omega_q + i\gamma} E_{\mathbf{q}}(\omega). \tag{3.13}$$

This solution allows us to determine the macroscopic polarization defined by equation (2.32). With equation (3.9) we obtain

$$P(\mathbf{r},\omega) = \sum_i \int \frac{d^3q}{(2\pi)^3}\, d_i^*\, \Psi_{\mathbf{q},n}(\omega)\, \Phi_{\mathbf{q}}(\mathbf{r}) \tag{3.14}$$

$$= \sum_i \int \frac{d^3q}{(2\pi)^3}\, |d_i|^2 \frac{\int d^3r' \Phi_{\mathbf{q}}^*(\mathbf{r}') E(\mathbf{r}',\omega)}{\bar{h}\omega - \varepsilon_i - \bar{h}\omega_q + i\gamma} \Phi_{\mathbf{q}}(\mathbf{r},\omega) \tag{3.15}$$

where the definitions (3.11) and (3.12) have been used. Clearly equation (3.14) has the form

$$P(\mathbf{r},\omega) = \int d^3r'\, \chi(\mathbf{r},\mathbf{r}',\omega) E(\mathbf{r}',\omega)\ , \tag{3.16}$$

which defines a macroscopic susceptibility,

$$\chi(\mathbf{r},\mathbf{r}',\omega) = \sum_i |d_i|^2 \int \frac{d^3q}{(2\pi)^3}\, \frac{e^{i\mathbf{q}\cdot(\mathbf{r}-\mathbf{r}')}}{\bar{h}\omega - \varepsilon_i - \bar{h}\omega_q + i\gamma}. \tag{3.17}$$

As expected for the homogeneous case, the translational invariance in the COM, $\chi(\mathbf{r},\mathbf{r}',\omega) = \chi(\mathbf{r}-\mathbf{r}',\omega)$ coordinate allows the introduction of the COM momentum $\mathbf{q}$ by a Fourier transformation in $\mathbf{r}-\mathbf{r}'$. In momentum space, we directly obtain

$$P_{\mathbf{q}}(\omega) = \chi(\mathbf{q},\omega)E_{\mathbf{q}}(\omega)\ . \tag{3.18}$$

The corresponding susceptibility

$$\chi(\mathbf{q},\omega) = \sum_i \frac{|d_i|^2}{\hbar\omega - \varepsilon_i - \hbar\omega_q + i\gamma} \tag{3.19}$$

describes excitonic resonances at ε_i due to the influence of the Coulomb interaction on the electron-hole relative motion as well as the energetic contribution $\hbar\omega_q$ of the COM motion. Since the boundary condition for the homogeneous case,

$$\Psi(\mathbf{r},\boldsymbol{\rho}) \to 0 \qquad \text{for } |\boldsymbol{\rho}| \to \infty, \tag{3.20}$$

involves only the relative variable $\boldsymbol{\rho}$, the excitonic relative and COM motion are decoupled.

A propagating electromagnetic wave in an infinitely extended medium whose response is described by equation (3.19) must be a solution of the EM field equations (2.37) and (2.38). Defining the dimensionless dielectric function

$$\varepsilon(q,\omega) = n_{\mathrm{bg}}^2 + \frac{\chi(q,\omega)}{\varepsilon_0} \tag{3.21}$$

the Fourier-transformed wave equation for E becomes[5]

$$\left[\frac{\omega^2}{c_0^2}\varepsilon(q,\omega) - q^2\right] E_q(\omega) = 0\ . \tag{3.22}$$

For a propagating solution the difference in the brackets must vanish. If only a 1s-exciton resonance is considered ($n = 1$) one obtains from equations (3.22) and (3.19) two *complex* solutions

$$q_{1,2}^2(\omega) = \frac{1}{2}(q_{\mathrm{bg}}^2 + q_X^2) \pm \sqrt{\frac{1}{4}\left(q_{\mathrm{bg}}^2 - q_X^2\right)^2 + \kappa^4}. \tag{3.23}$$

Here we have defined

$$q_{\mathrm{bg}}^2 = \frac{\omega^2}{c_0^2} n_{\mathrm{bg}}^2\ , \tag{3.24}$$

$$q_X^2 = \frac{2M}{\hbar^2}(\hbar\omega - \varepsilon_1 + i\gamma)\ , \tag{3.25}$$

$$\kappa^4 = \frac{\omega^2}{c_0^2}\frac{2M}{\hbar^2\varepsilon_0}|d_1|^2. \tag{3.26}$$

Assuming $d(\boldsymbol{\rho}) \equiv d_{\mathrm{cv}}\delta(\boldsymbol{\rho})$ as always in this work, the dipole matrix element (3.11) takes the form

$$|d_1|^2 = \frac{|d_{\mathrm{cv}}|^2}{\pi a_{\mathrm{B}}^3} \tag{3.27}$$

due to the normalization of the excitonic wavefunctions. The complex wavevectors (3.23) form the two polariton dispersion branches. The real part of these wave-vector frequency dispersions describe the propagation of polaritons in the infinitely extended medium and the imaginary part is associated with the damping of the polariton waves. The propagating solutions from the infinitely extended medium have been used in various forms in the construction of macroscopic approximations for finite samples, some of which are discussed in the next section.

3.2. Macroscopic Approaches

We discuss in this section how approximations use the propagating solutions for *homogeneous* media from section 3.1 to describe nonlocal (spatially inhomogeneous) situations.

If we consider a finite sample with surfaces in the propagation direction, the system becomes spatially inhomogeneous and more complicated boundary conditions for the interband transition amplitude apply. For the case of a slab geometry we have the boundary condition that

$$\Psi(\mathbf{r}_{\mathrm{e}}, \mathbf{r}_{\mathrm{h}})\big|_{\text{at surface}} = 0, \tag{3.28}$$

i.e., that the transition amplitude vanishes whenever $\mathbf{r}_{\mathrm{e}}$ or $\mathbf{r}_{\mathrm{h}}$ are on one of the surfaces. This boundary condition introduces an entanglement between the excitonic relative and COM motion which was not present in the case of an infinitely extended medium where the boundary condition simply required the vanishing of Ψ at infinity, cf. equation (3.20).

Since the direct computation of the transition amplitude from the two-particle Schrödinger equation and the boundary condition (3.28) for the inhomogenous case, as discussed in chapter 2, is numerically very demanding, in the past many approaches have been based on the approximate separation of the excitonic relative and COM motion, even though the slab boundary conditon makes this impossible in a rigorous way. Instead of applying equation (3.28), boundary conditions are imposed on the eigenvalue equation (3.5) of the COM Hamiltonian

$$H_{\mathrm{com}}\,\Phi_q(\mathbf{r}) = -\frac{\hbar^2}{2M}\nabla_{\mathbf{r}}^2\Phi_q(\mathbf{r}) = \hbar\omega_q\,\Phi_q(\mathbf{r}), \tag{3.29}$$

$$\Phi_q(\mathbf{r})\big|_{\mathbf{r}\text{ at surface}} = \Phi_{\mathrm{surf}} \tag{3.30}$$

by specifying the value Φ_{surf} at the boundaries. This leads to eigenfunctions and eigenenergies which are strikingly different from the solutions of equation (3.5) without boundary condition. For the excitonic relative motion, however, the solutions of the Wannier equation (3.4) for the homogeneous system are used. Thus postulating boundary conditions for equation (3.29) results in approximations that cannot account for the modification of the excitonic relative motion at the boundaries which strongly influences the reduction of the macroscopic polarization near the surfaces. Moreover, different boundary conditions for the COM problem lead to qualitatively different macroscopic approximations because the spatial behavior of the macroscopic polarization near the surfaces critically influences the propagating solutions even in large samples.

In the following, we briefly outline approximation schemes based on the assumptions discussed in the previous paragraph. Taking into account only the interaction with the 1s exciton resonance, one uses the two complex polariton wavevectors (3.23),for the propagating electromagnetic field inside the finite semiconductor domain

$$E_{\text{mat}}(z,\omega) = \sum_{p=1,2} E_p^+(\omega) e^{iq_p(\omega)z} + E_p^-(\omega) e^{-iq_p(\omega)z}. \tag{3.31}$$

Here, propagating (E^+) and counterpropagating waves (E^-) are considered for the slab geometry. Equation (3.31) describes the propagation of an optical field in the infinitely extended system. The same equation (3.31) is now used as an *ansatz* for the spatially inhomogeneous case. Then one applies Maxwell's boundary conditions to connect the polariton solutions inside the slab (3.31) to free solutions of Maxwell's equations outside the domain. The simplest possible geometry involves an incident wave from the left and the reflected and transmitted components, E_{r} and E_{t}, respectively,

$$E_{\text{left}}(\omega,z) = e^{iq_{\text{left}}z} + E_{\text{r}}(\omega) e^{-iq_{\text{left}}z}, \tag{3.32}$$

$$E_{\text{right}}(\omega,z) = E_{\text{t}}(\omega) e^{iq_{\text{right}}z} \tag{3.33}$$

where

$$q_{\text{left}} \equiv n_{\text{left}} \frac{\omega}{c_0} \tag{3.34}$$

and a respective definition for q_{right} holds. The continuity of E and $\partial E/\partial z$ on both boundaries determines only four of the six unknown coefficients $E_{\text{r}}(\omega)$, $E_{\text{t}}(\omega)$, $E_1^{\pm}(\omega)$, and $E_2^{\pm}(\omega)$. The remaining two conditions are fixed by prescribing macroscopic boundary conditions for the excitonic COM wavefunctions in equation (3.30). This prescription together with equation (3.31) can be used to

determine an additional boundary condition (ABC) for the macroscopic polarization. For instance, the choice $\Phi_{\text{surf}} = 0$ at the boundary of a half-space geometry[36] leads to the additional boundary condition for the macrocopic polarization

$$P(z,\omega)|_{z \text{ at boundary}} = 0, \tag{3.35}$$

originally introduced by Pekar.[8] The choice $\Phi_{\text{surf}} = 1$ in the same geometry results in the Ting-Frankel-Birman (TFB) additional boundary condition[10]

$$\left[\frac{\partial}{\partial z} P(z,\omega)\right]_{z \text{ at boundary}} = 0. \tag{3.36}$$

In both conditions (3.35) and (3.36) the macroscopic polarization is given by the result valid in an infinitely extended material. For this special case it can be obtained by using equations (3.17) and (3.31) in equation (3.16)

$$P(z,\omega) = \sum_{p=1,2} \chi(q,\omega)|_{q=q_p(\omega)} \left[E_p^+(\omega) e^{iq_p(\omega)z} + E_p^-(\omega) e^{-iq_p(\omega)z}\right]. \tag{3.37}$$

In the past, equations (3.35) or (3.36) together with equation (3.37) used to be regarded as a boundary-condition problem because one can also obtain them by using the expression for the macroscopic polarization (3.37), which is valid in an infinitely extended medium, and simply *specifying* equation (3.35) or (3.36) or even a linear combination of equations (3.35) and (3.36) as a boundary condition. As emphasized previously this does not define a mathematical boundary-value problem since $P(z,t)$ itself is not determined by a differential equation.

In a recent paper,[9] Henneberger combined the macroscopic dielectric function of an infinitely extended medium with a new analysis of surface effects to describe light propagation with spatial dispersion in finite samples. The assumption underlying this approach is that only in a thin transition layer near a surface deviations from the bulk properties are important. The key idea is to describe the influence of surfaces via source layers with strength s_i in the wave equation for the infinitely extended medium, written in momentum space as

$$\left[\frac{\omega^2}{c_0^2}\varepsilon(q,\omega) - q^2\right] E(q,\omega) = \sum_i s_i(q,\omega)\ , \tag{3.38}$$

cf. equation (3.22). The solutions of equation (3.38) for source terms within an infinitely extended medium are used to describe finite samples ending at the position of the source layers. By matching the material solution to the outside solution, the source terms can be determined. The validity of this matching procedure has to be checked because here one connects solutions for infinitely extended media at the surface, even though these solutions can only be a valid approximation

away from the surface. Therefore, matching the two solutions at a boundary can be a good approximation only if the difference between the outside solution E_0 and material solution E_{mat} is small. Following the original analysis,[9] both fields are expanded up to second order in the distance from the surface. For a wave propagating in z direction through a boundary at $z = 0$ one obtains

$$\begin{aligned} E_0(z) - E_{\mathrm{mat}}(z) &= \left[\left.\frac{\partial^2}{\partial z^2}\right|_{z=0} E_0 - \left.\frac{\partial^2}{\partial z^2}\right|_{z=0} E_{\mathrm{mat}} \right] \frac{z^2}{2} + O(z^3) \\ &\approx \left[(q_1^2 - q_0^2) E_1^+ + (q_2^2 - q_0^2) E_2^+ \right] \frac{z^2}{2} \end{aligned} \tag{3.39}$$

where the continuity of the fields and their first derivatives have been used. In equation (3.39) q_0 is the wave number of the external field and $q_{1,2}$ are the complex polariton solutions for the 1s exciton resonance, cf. equation (3.23). At resonances of the optical susceptibility of the semiconductor, the modulus of $q_{1,2}^2(\omega)$ becomes large and the thickness of the transition layer, which has to be used for z in equation (3.39) is not clear. Hence it is difficult to show that the last line in equation (3.39) is small enough to ensure a good approximation.

3.3. Comparison of Results

In this section we compare approximative treatments for the light-propagation in bulk semiconductors under the influence of sample boundaries with the full solution of the propagation problem. We focus on samples of intermediate thickness where the geometrical confinement for the material polarization as well as genuine polaritonic effects due to the propagation of the optical field over distances on the order of a wavelength are present. The combination of these mechanisms leads to several interesting features in the optical transmission spectra.

Whereas for the description of experimental results in chapter 2 it is necessary to include separate heavy and light-hole bands as well as anisotropic masses, for clarity of the comparison we work with a two-band semiconductor model in the present section. We use a single hole mass of $m_{\mathrm{h}} \equiv m_{\mathrm{hz}} = m_{\mathrm{h}\perp} = 0.46\, m_0$ and a dephasing rate $\gamma = 0.01 E_{\mathrm{B}} = 0.04\,\mathrm{meV}$, which corresponds to a decay time of $T = 15.7\,\mathrm{ps}$. For the other parameters we use the values given in table 2.1. We again use the same background refractive index inside and outside of the sample since this eliminates Fabry-Pérot resonances. As explained in chapter 2 the corresponding experimental situation can be realized in semiconductor heterostructures where one sandwiches the semiconductor material, which resonantly interacts with the optical field, between buffer layers having a similar refractive index but larger band-gap energies.

Approximative solutions using ABC models and the Henneberger approach are determined only for the contribution of the 1s-exciton resonance as usually done in the literature even though the extension to other bound excitonic states is possible in principle. The full solution always includes both excitonic bound and continuum states.

Figure 3.1 shows transmission spectra for a sample thickness $L = 10\,a_{\mathrm{B}}$ obtained from the microscopic calculation together with transmission spectra based on the Henneberger approach and the Ting-Frankel-Birman ABC. In the full calculation the 1s-excitonic resonance exhibits a clear splitting ($n = 1,2$). Also additional peaks at higher energies ($n \geq 3$) occur. To analyze the multiple-peak structure in the transmission spectrum we consider the quantization of the excitonic COM motion[25,38] as given by the approximate equations (3.29) and (3.30) which neglect the coupling between the relative and COM exciton motion. The choice of $\Phi_{\mathrm{surf}} = 0$ in equation (3.30) for a finite sample of length L then leads to discrete energies for the COM motion,

$$E_n = \frac{\hbar^2}{2M}\left(\frac{\pi}{L}\right)^2 n^2, \tag{3.40}$$

where $M = m_{\mathrm{e}} + m_{\mathrm{h}}$ is the excitonic mass. Only peaks with lower oscillator strength (n =4, 5, 6) can be roughly fitted with $L \simeq 9\,a_{\mathrm{B}}$ as COM quantization resonances. The smaller effective length that has to be used in equation (3.40) is a result of a "dead layer" effect.[33] Due to the finite extension of the excitonic relative motion the macroscopic polarization remains small in regions near the surface. In the "dead layer" picture the excitonic COM motion is confined to a reduced slab length. Note that the odd numbered peaks have a much weaker oscillator strength, for instance, $n = 5$ at $\hbar\omega = -0.61\,E_B$ is almost indiscernible. The detailed structure of the double peak with the high oscillator strength, on the other hand, is dominated by polaritonic effects: Using equation (3.40) to fit the double peak leads to $L \simeq 25\,a_{\mathrm{B}}$ which clearly illustrates that the concept of excitons with mass M confined to an effective length is not applicable near the main resonance.

The Henneberger approach does not account for the additional maxima above the excitonic resonance in the transmission spectrum. Instead of a multiple peak structure a single asymmetric lineshape is predicted. The ABC of Ting et al. leads to only one very small replica; no satisfactory agreement is obtained with the full calculation regarding the lineshape of the main resonance. Furthermore, it is not possible to fit the results of Henneberger and Ting et al. to the full calculation by artificially increasing the dipole coupling as shown by the dashed lines in figure 3.1 where $r_{\mathrm{cv}} = 10$ Å has been used.

Figure 3.2 shows the corresponding transmission spectra calculated with Pekar's ABC. The sample length is varied to account for an exciton-free dead layer. Transmission spectrum (a) is obtained without assuming a dead layer, i.e., using

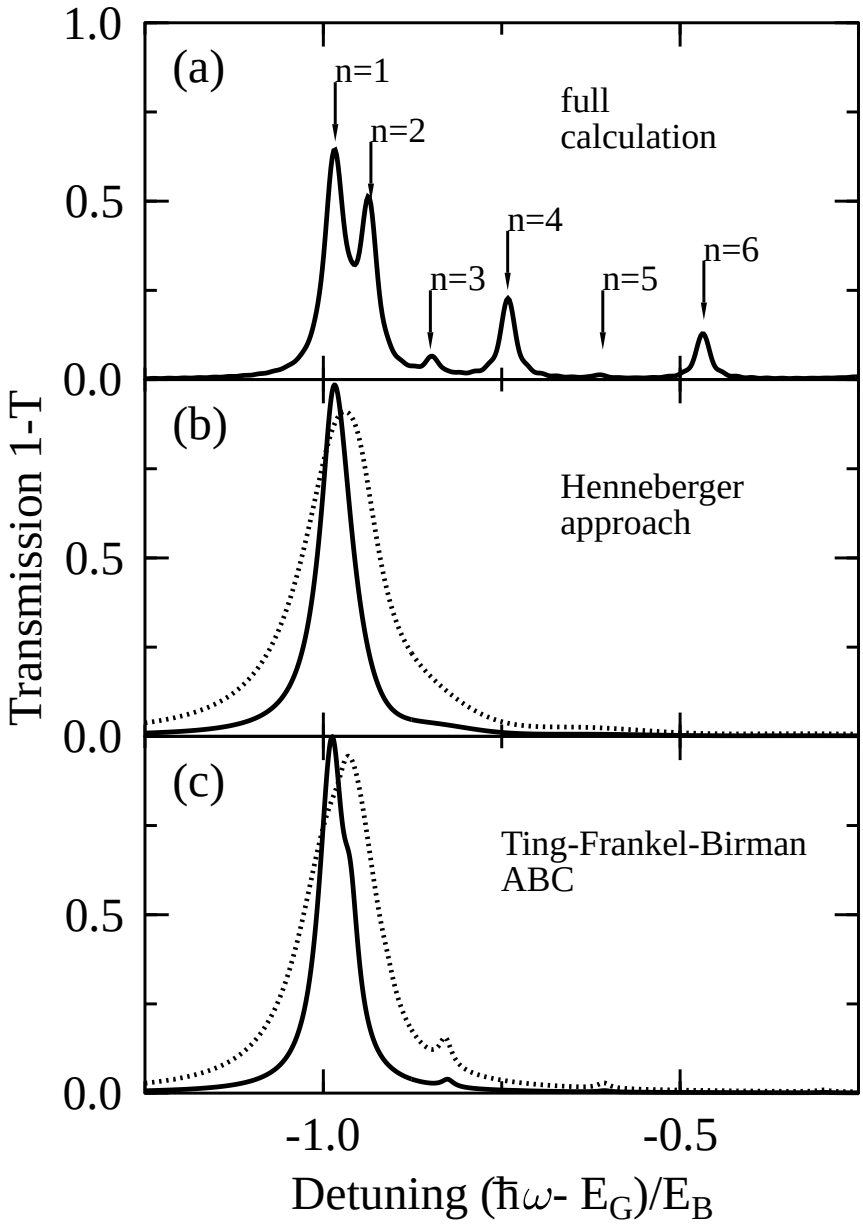

Figure 3.1.: Calculated transmission for a sample length $L = 10\,a_{\mathrm{B}}$ using the full calculation (a), the Henneberger approach (b), and the additional boundary condition (ABC) of Ting, Frankel, and Birman (c). The detuning is relative to the bulk semiconductor band-gap energy E_G in units of the three-dimensional exciton Rydberg energy E_B. Solid lines correspond to a dipole coupling of $r_{\mathrm{cv}} = 5\,\text{Å}$ and dotted lines to $r_{\mathrm{cv}} = 10\,\text{Å}$.

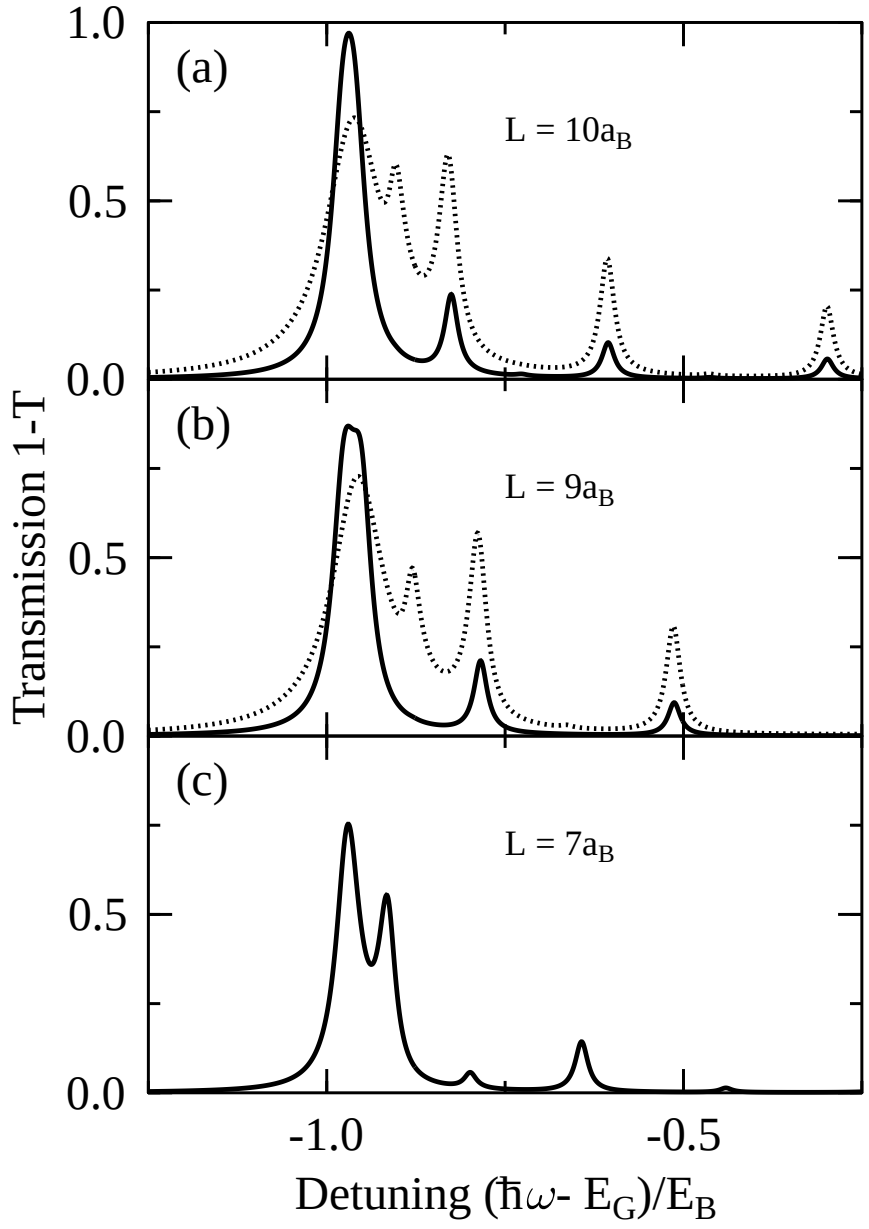

Figure 3.2.: Calculated transmission using Pekar's ABC with effective sample lengths $10\,a_{\mathrm{B}}$ (a), $9,a_{\mathrm{B}}$ (b), and $8.5\,a_{\mathrm{B}}$ (c) for otherwise the same parameters as in figure 3.1. Solid lines correspond to $r_{\mathrm{cv}} = 5\,\text{Å}$ and dotted lines to $r_{\mathrm{cv}} = 10\,\text{Å}$.

Pekar's ABC in their original form with $L = 10\,a_B$. This gives a qualitatively different picture compared to the full calculation because the double-peak structure of the main resonance is not reproduced and the spacing of the higher replicas is different. For figure 3.2(b) the effective length extracted from the full calculation, $L = 9\,a_B$, has been used. Then the high-energy replicas are reproduced but the agreement for the lineshape of the main peak remains unsatisfactory. Curve (c) is a fit which is aimed at reproducing the typical double-peak structure of the main resonance as well as possible. This requirement leads to the choice $L = 7\,a_B$ and does give a good agreement with the lineshape of the full calculation. However, it does not reproduce the full spectrum because the COM replicas are now shifted.

When the effective sample length is regarded as a fitting parameter, Pekar's ABC allows qualitatively better fits to the full calculation than the Henneberger or TFB approach. It is impossible, though, to obtain an overall agreement with the full calculation because the choice of the effective sample length works in different ways. First, it influences the COM quantization energies of the replicas. Second, it is important for the interference of the propagating polaritons in the sample. Optimizing the lineshape of the main peak, which is dominated by propagation effects, leads to less satisfactory results for the energetical spacing of the COM replicas, and vice versa. It is also impossible to improve the agreement by artificially increasing the dipole coupling as illustrated by the dotted lines in figure 3.2.

Figure 3.3(a) shows again the full calculation for the same parameters as above and sample lengths of $L = 10\,a_B$, $3\,a_B$, and $2\,a_B$. For decreasing sample length we obtain a pronounced energy shift of the whole spectrum due to the confinement of the electrons and holes which effectively shifts the entire electron and hole bands. Furthermore the spacing of the exciton replica at higher energies increases. For $L = 3\,a_B$ and $L = 2\,a_B$ the light-matter coupling results mainly in a broadening of the exciton line. Figure 3.3 (b) contains the corresponding spectra obtained with the same parameters using Pekar's ABC. In this approximation the energy shifts are caused only by the COM quantization of ideal 3D excitons formed from electron and hole bands unaffected by a geometrical confinement. Thus for the smaller samples the lineshapes obtained from Pekar's ABC are qualitatively correct but the energy shifts due to carrier confinement are not reproduced.

The series of results for decreasing sample length in figure 3.3 also reveals the nature of the splitting of the exciton resonance for $L = 10a_B$ and especially the $n = 2$ peak in figure 3.1(a). As mentioned above, the peak position cannot be explained as a replica due to COM quantization if one treats the COM motion independently of the exciton relative motion. On the other hand, the $n = 2$ peak shifts away from the exciton resonance to higher energies ($\hbar\omega - E_G = 0.23E_B$) if the sample length is decreased to $L = 3\,a_B$. The corresponding peak for $L = 2\,a_B$

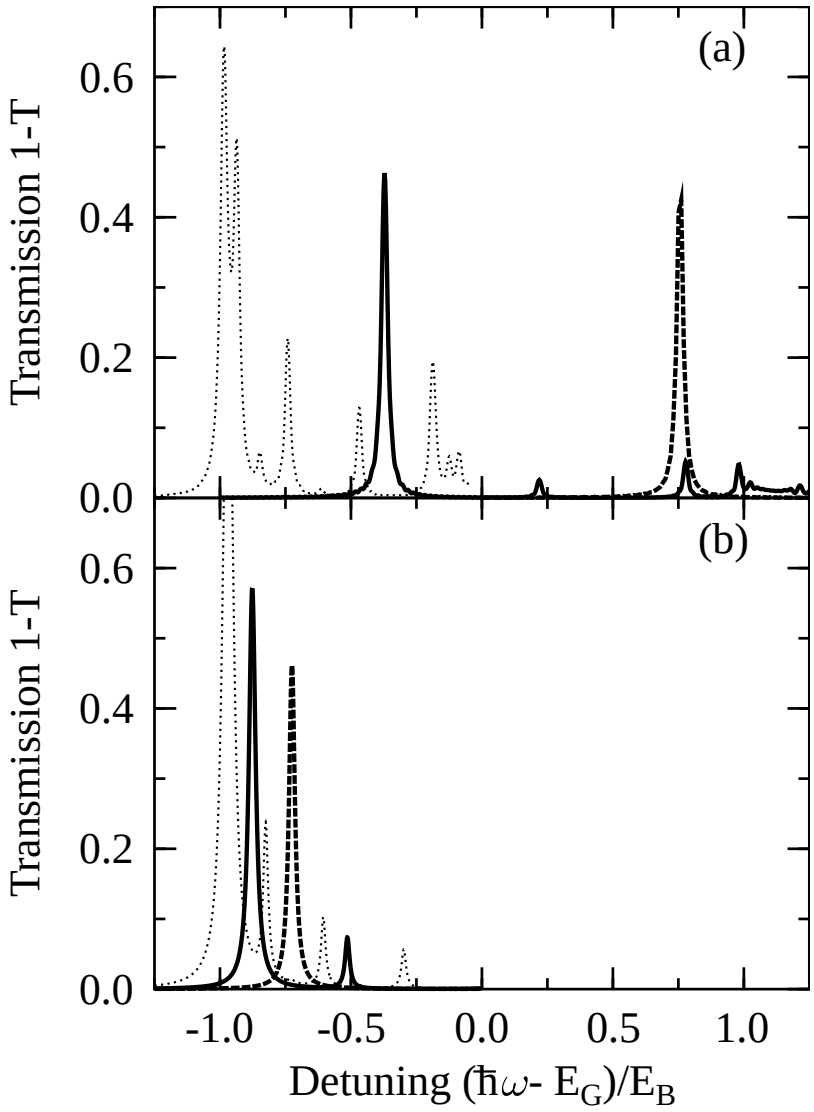

Figure 3.3.: Calculated transmission for various sample lengths using the full calculation (a) and Pekar's ABC (b): $L = 10\,a_{\mathrm{B}}$ (thin line), $L = 3\,a_{\mathrm{B}}$ (solid line), and $L = 2\,a_{\mathrm{B}}$(dashed line). The dipole coupling is $r_{\mathrm{cv}} = 5\,\text{Å}$.

at $\hbar\omega - E_G = 1.9E_B$ is not shown in figure 3.3. Hence, for $L = 10\,a_B$, the $n = 2$ resonance is due to the combined influence of the COM quantization and the energy dressing of the coupled exciton-photon states which is described for the spatially homogeneous system in section 3.1 in terms of polariton states. Clearly, for $L = 3\,a_B$ and $L = 2\,a_B$ the COM quantization energies are already so large that the $n = 2$ replica does not interfere with the remaining radiatively broadened exciton resonance.

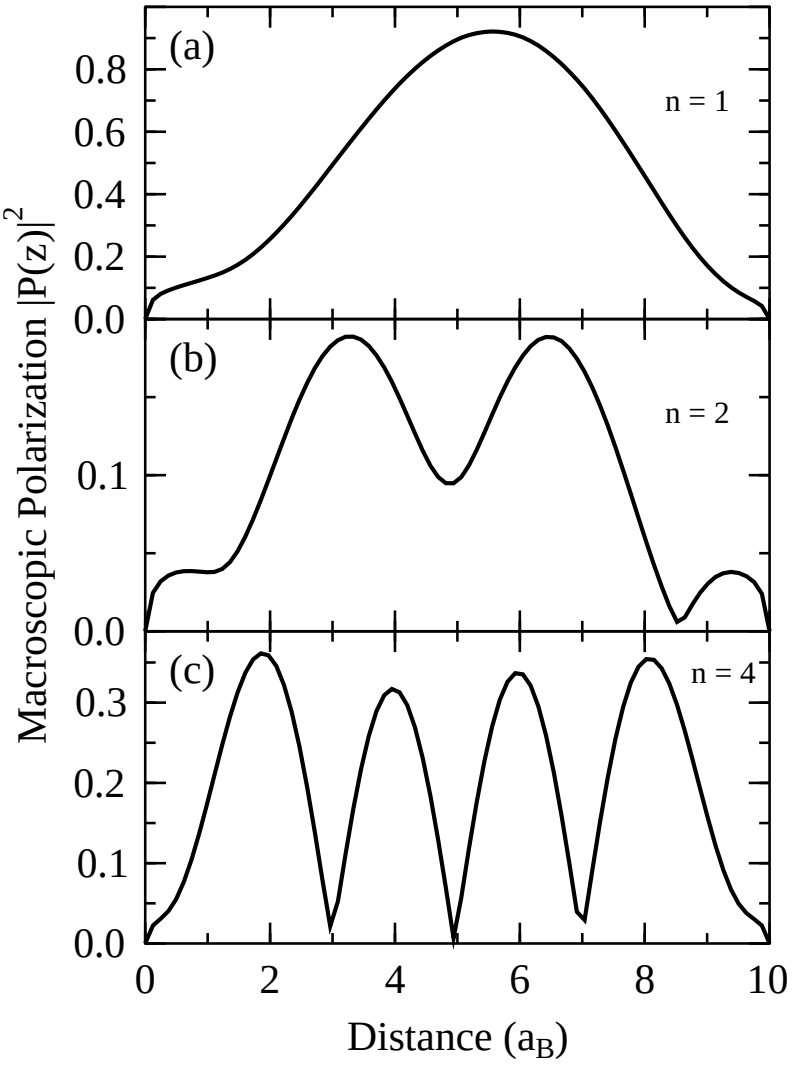

Figure 3.4.: Spatial distribution of the macroscopic polarization for stationary, monochromatic excitation at the absorption peaks corresponding to $n = 1, 2$ and 4 in figure 3.1(a).

The features in the transmission spectrum have their counterparts in the spatial distribution of the macroscopic polarization. Using the full numerical solution of the propagaton problem, which determines the electron-hole transition amplitude, we directly obtain from equation (2.32) the spatial distribution of the macroscopic polarization which also enters Maxwell's equations. For a stationary monochromatic driving field, we find different spatial distributions of the macroscopic polarization depending on the driving field frequency. Figure 3.4

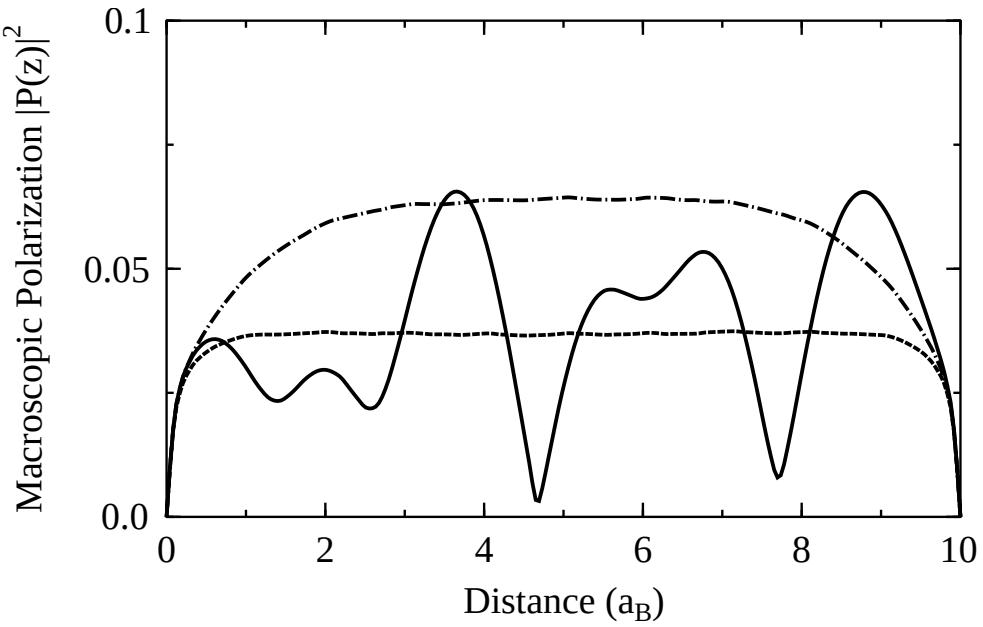

Figure 3.5.: Spatial distribution of the macroscopic polarization for optical excitation below ($\hbar\omega - E_G = -2.5E_B$, dashed line) and near ($\hbar\omega - E_G = -1.25E_B$, dash-dotted line) the main absorption peak, as well as above the $n = 4$ peak ($\hbar\omega - E_G = -0.6E_B$, solid line), corresponding to figure 3.1(a).

shows the distribution of $|P(z)|^2$ over a sample of length $L = 10\,a_B$. The curves (a), (b), and (c) correspond to excitation energies at the $n = 1$, 2 and 4 peaks in figure 3.1(a), respectively. The spatial distribution further supports the connection of the peaks to the COM quantization. If, for comparison, the COM motion is considered independent of the relative motion, equation (3.29) together with the boundary condition (3.30) and $\Phi_{\text{surf}} = 0$ determines eigenfunctions $\Phi_n(z)$, which belong to the eigenvalues given by equation (3.40), as standing sine waves with n maxima. Deviations of the full calculation in figure 3.4 from this behavior show how the relative excitonic motion near the surface influences the macroscopic polarization. Also the concept of a uniform polarization-free region (dead layer) near the surface can be now be investigated. Clearly, the thickness of layers with reduced polarization is *different* for the $|P(z)|$ distributions corresponding to energies in figure 3.1(a). For $n = 1$ and $n = 2$, there is a region of roughly $\ell = 1.5\,a_B$ thickness at both surfaces, in agreement with the fitting procedure in figure 3.2(c) to reproduce the features around the exciton resonance using an effective length $L_{\text{eff}} = L - 2\ell = 7\,a_B$. In figure 3.4(c), which corresponds to the $n = 4$ peak, this dead layer is reduced to $\ell = 0.5\,a_B$ which also explains the deviation of the effective length $L_{\text{eff}} = L - 2\ell = 9a_B$ to fit the corresponding peak position in fig-

ure 3.2(b). With the exception of Ref. 39 dealing with superlattices, approaches which attempt to justify the dead-layer assumption usually predict that the quantity $\ell/(ia_B)$, where i denotes the principal exciton quantum number, be constant for any given material and usually lead to numerical values in the range of 2–3 for this quantity.[3] This is violated here because all COM replicas belong to the same 1s resonance but lead to *different* dead layers for different energies.

For completeness, we show in figure 3.5 the spatial distribution of $|P(z)|$ for the same configuration as figure 3.4 but excitation energies tuned away from the resonances. In all cases we find a rapid growth of the polarization from the surface into the sample without a dead layer.

The spatial distributions of the macroscopic polarization in the $L = 3a_B$ sample, whose linear spectrum is shown as solid line in figure 3.3, are given in figure 3.6. Only small regions of reduced polarization at the surfaces are obtained for the two resonances at detunings $\hbar\omega - E_G = -0.38E_B$ and $+0.22E_B$ whereas below the resonances ($-0.9E_B$) these regions are completely absent.

After this comparison of macroscopic approaches to our microscopic results we now return to the experimental results presented in chapter 2 for a comparison of the macroscopic approaches. In figure 3.7 we show transmission spec-

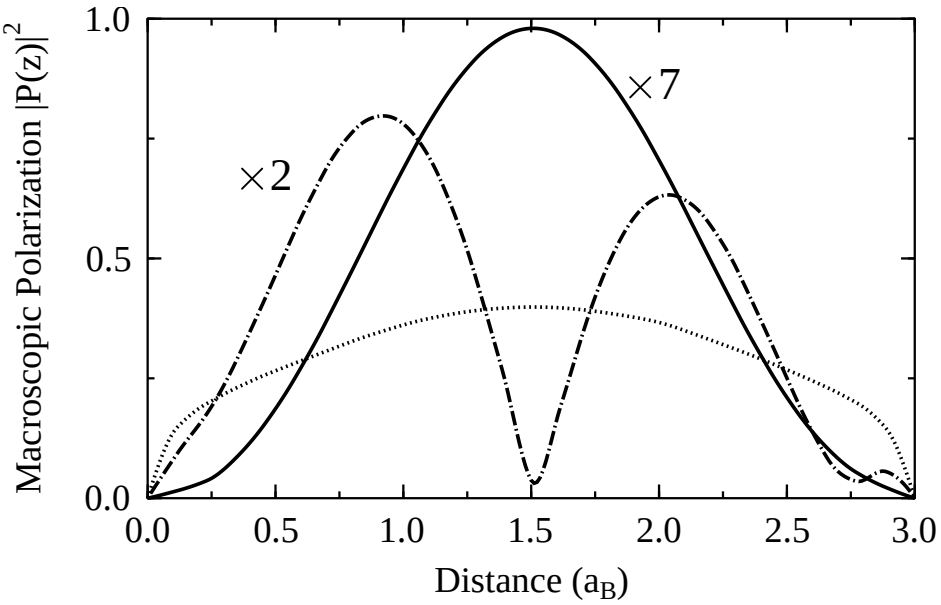

Figure 3.6.: Spatial distribution of the macroscopic polarization for a sample length $L = 3a_B$. The optical driving field is tuned below the main resonance ($\hbar\omega - E_G = -0.9E_B$, dotted line), and to the first ($\hbar\omega - E_G = -0.38E_B$, solid line) and second ($\hbar\omega - E_G = 0.22E_B$, dash-dotted line) peak in the transmission spectrum shown as solid line in figure 3.3(a).

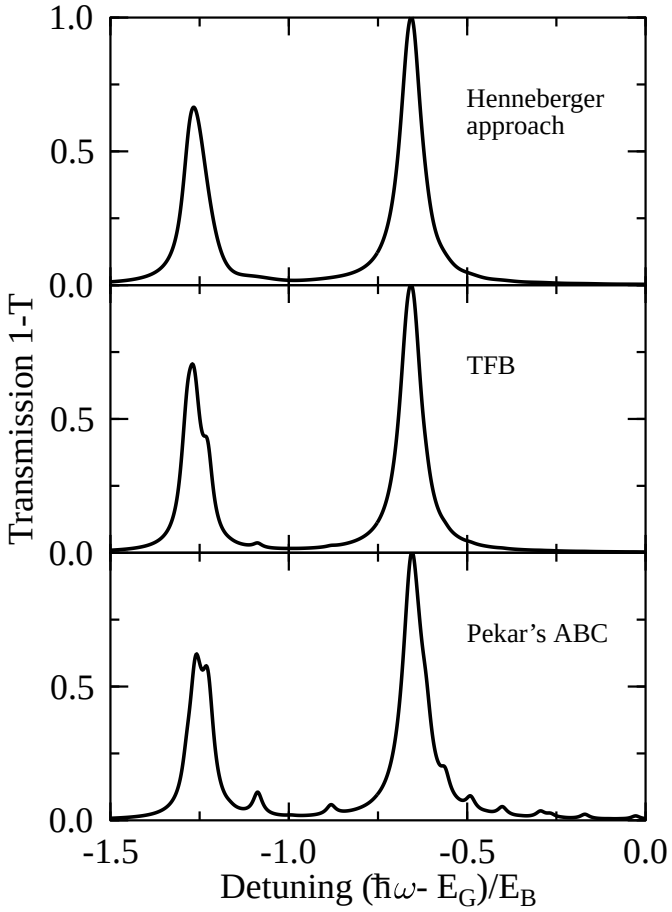

Figure 3.7.: Transmission spectra obtained from the Henneberger approach (top), Ting-Frankel-Birman (middle) and Pekar's ABC (bottom), using the same parameters as for the full calculation, figure 2.1(c).

tra obtained from the approaches due to Pekar, Ting et al. and Henneberger. In the numerical calculations for the approximations we used the 1s-contribution of the numerically calculated suceptibility including band-structure effects, which is shown in figure 2.3. The Henneberger approach neither reproduces the characteristic features of HH and LH excitonic lineshapes nor the COM replicas. The Ting-Frankel-Birman ABC exhibits the characteristic double-peak structure of the of the LH exciton line but the HH lineshape remains symmetrical and there are no pronounced COM replicas as in the experimental spectrum. In comparison to the other approaches, Pekar's original ABC yields qualitatively the best results. The detailed energy spacing of the features present in the spectra, however, cannot be reproduced using this approach, as will be examined in detail in chapter 3.

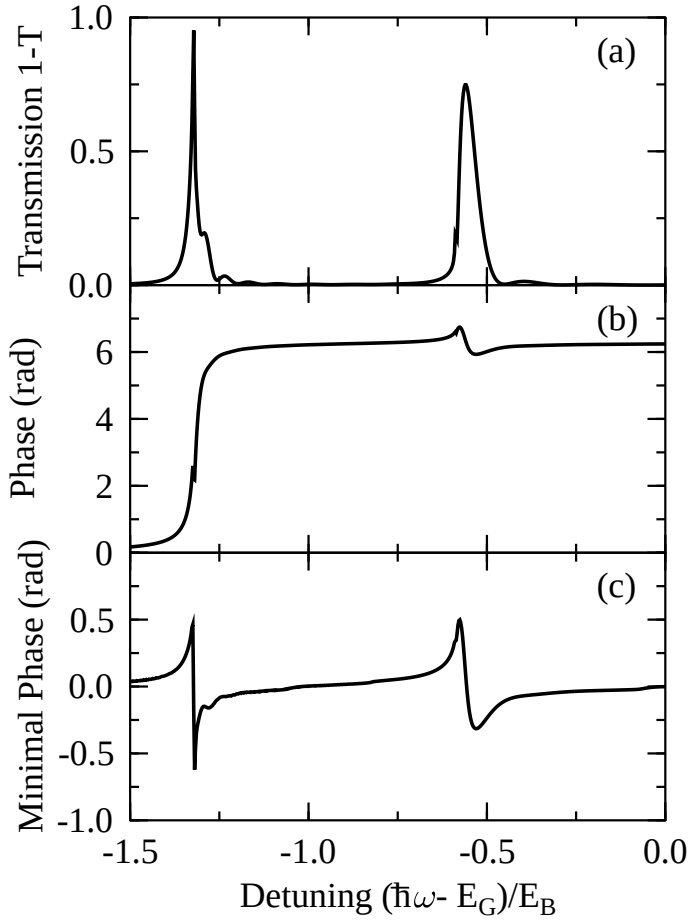

Figure 3.8.: Transmission spectrum (a) obtained with the Henneberger approach using artificial mass parameters and an enlarged phenomenological dephasing time $T = 150\,\mathrm{ps}$, and corresponding phase spectrum (b). The minimal phase spectrum (c) is calculated from the transmission spectrum via a Hilbert transform, cf. equation (2.42).

In the context of approximative solutions, the free choice of material parameters can lead to wrong results if one chooses a macroscopic model which, in comparison to Pekar's ABC, has an entirely different dependence on the physical quantities entering the calculation, like the Henneberger model. One often encounters situations where the material or growth parameters are not known. Then hole mass, the sign of the strain energy, which is opposite for compressive and tensile strain, and oscillator strength for a given excitonic resonance can only be obtained by a fit based on a model calculation. Figure 3.8(a) shows the calculated transmission spectrum obtained from the Henneberger approach where,

in comparison to figure 3.7, the *heavy* hole mass parameters and dipole coupling have been used for the *light* hole excitonic resonance and vice versa. Also, the phenomenological dephasing time T has been increased by more than a factor of 10 to $T = 150\,\mathrm{ps}$. With this unphysical choice of parameters the Henneberger approach roughly reproduces both the double peak structure of the lower resonance and the asymmetry of the higher resonance. Note that the main difference between experimental and calculated spectra occurs as a narrow peak at the energetically lowest resonance. Due to the finite experimental resolution this does not rule out a qualitative agreement between experiment and calculation and allows an explanation in terms of wrong parameters and a strongly overestimated dephasing time. Certainly, the discrepancy between the experimental and calculated transmission spectrum is much smaller than one would expect from the wrong choice of fitting parameters. The situation is different for the phase spectrum as can be seen in figure 3.8(b) where we show the corresponding calculated phase. The dominating feature here is an increase of the phase by about 2π. Also, the phase spectrum shows a very weak dip at the lower resonance and the signature of the ususal anomalous dispersion at the higher resonance. Since the overall behavior deviates drastically from the experimental spectrum over the whole frequency range, it completely rules out the explanation of the experiment in terms of Henneberger's model and the chosen parameters. This decisive information can only be obtained by a separate phase measurement for the transmitted optical field because the transmission alone does not contain this information. To illustrate this point further we have calculated the Hilbert transform of $\log|t(\omega)|$, see equation (2.42), which yields the "minimal phase"[31] but not the additional contributions of the Blaschke factors. The resulting phase spectrum is shown in figure 3.8(c). Its overall resemblance to the experimental spectrum is much better than that of the full phase. Moreover, the deviations are concentrated to small regions of the frequency range which could be difficult to detect because of the finite experimental resolution.

4. Coherent Dynamics in Transverse Magnetic Fields

4.1. Introduction

In this chapter we present an investigation of semiconductor quantum well materials under the influence of a magnetic field. In principle, one has two choices for the alignment of the magnetic field with respect to the growth direction of the quantum well. One possibility is the so-called Faraday geometry, in which the magnetic field is directed perpendicular to the quantum well, i.e., in the growth direction. Then the geometrical confinement of the carriers in the quantum-well, which leads to a quasi two-dimensional electron gas, is combined with the confinement of the carriers on Landau levels introduced by the electromagnetic field. This is useful if one wishes to achieve maximal confinement for the carriers.[40,41]

The other possibility is the so-called Voigt geometry, which is the only configuration discussed in the following. Here, the magnetic field is oriented parallel to the quantum-well plane, i.e., transverse to the growth direction. Then the magnetic field does not contribute to the carrier confinement but instead breaks the rotational symmetry along the growth direction. The carrier states in the quantum well are described by mixtures of angular momentum states defined with respect to the growth direction as natural quantization axis. Because of the magnetic moment associated with the angular momentum the transverse magnetic field induces carrier transitions between electron bands with different spin quantum numbers. This carrier dynamics will be discussed theoretically in the present chapter.

The transitions between electronic bands caused by the magnetic field lead to an interplay with electron-hole transitions caused by optical fields. These effects will be discussed in the subsequent chapter. Therefore the following theoretical development is already directed towards taking also the interaction with optical fields into account.

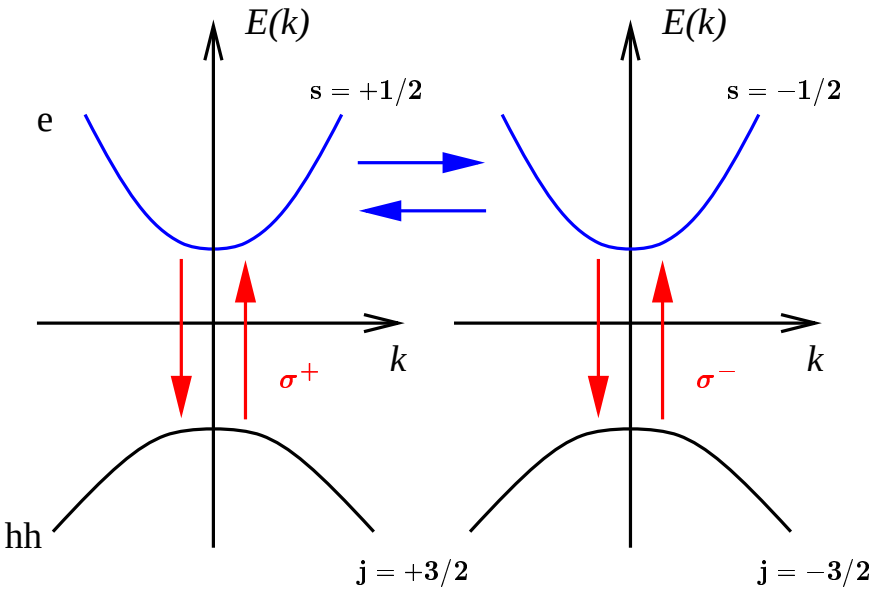

Figure 4.1.: Schematic band structure. The energetically degenerate electron and hole bands are drawn side by side. The two polarizations of the light field interact with different subsystems of bands, the transitions are indicated as vertical arrows marked by σ_+ and σ_-, respectively. The transverse magnetic field couples the electron bands of both subsystems, as indicated by the horizontal arrows.

4.2. 2D-Carrier System with Magnetic Field

In quantum wells the confinement in z direction introduced by different material layers breaks the full rotational symmetry. In the majority of cases, though, it is a good approximation to assume that the heterostructure is still invariant with respect to rotations around the z axis and this makes the z axis the natural quantization axis for angular momenta. Thus the definition of electron and hole band states given in section 2.1, which uses the angular momentum projection quantum numbers in z direction, can also be used for quantum-well bandstructures. Due to the confinement in growth direction the band structure is qualitatively modified leading, for instance, to the emergence of subbands.

For sufficiently narrow wells and excitation energies close to the fundamental bandgap higher subbands are not excited. In quantum wells, the heavy and light hole bands are energetically separated due to the reduction of symmetry[5] which lifts the degeneracy present in bulk structures without strain.

Our model bandstructure including the heavy-hole and electron bands is depicted in figure 4.1: The bands are labeled according to their angular momentum

projection quantum numbers in z direction by by $|s\rangle$ and $|j\rangle$, respectively. Electron states are described by the total spin $S = \frac{1}{2}$ and spin projection $s = \pm\frac{1}{2}$.* The heavy hole states carry the total angular momentum $J = \frac{3}{2}$ and the projection $j = \pm 3/2$. Throughout the following we will use parabolic bands described by dispersions $\varepsilon_{\mathrm{e}}(k)$ and $\varepsilon_{\mathrm{h}}(k)$ with corresponding effective masses for electrons and holes, respectively.

The Hamiltonian for the carriers is given by equation (2.1) together with the magnetic field interaction Hamiltonian

$$\widehat{H}_{\mathrm{mag}} = -\widehat{\boldsymbol{\mu}} \cdot \mathbf{B}, \tag{4.1}$$

where $\widehat{\boldsymbol{\mu}}$ is the operator of the magnetic moment. Using the electron and hole band states discussed above, the Hamiltonian takes the form

$$\widehat{H}_{\mathrm{mag}} = \sum_{ss'=\pm\frac{1}{2}} \sum_{\mathbf{k}} \langle s|\mu_x|s'\rangle B c^{\dagger}_{s'}(\mathbf{k}) c_s(\mathbf{k}) + \sum_{jj'=\pm\frac{3}{2}} \sum_{\mathbf{k}} \langle j|\mu_x|j'\rangle B c^{\dagger}_{j}(\mathbf{k}) c_{j'}(\mathbf{k}) \; . \tag{4.2}$$

Again $c^{\dagger}_s(\mathbf{k})$ denotes the creation operator for an electron with crystal momentum $\mathbf{k}$ and spin component $s = \pm\frac{1}{2}$ in z-direction; $c^{\dagger}_j(\mathbf{k})$ represents the corresponding creation operator for heavy holes with the projection quantum number $j = \pm\frac{3}{2}$. Since we will only deal with quantum-wells in the following we have written the *two-dimensional* crystal momentum simply as k and have omitted the "$\perp$" used in chapter 2 because no three-dimensional momenta will occur from now on.

For free electrons the magnetic moment is connected to the spin via

$$\widehat{\boldsymbol{\mu}} = g_0 \mu_{\mathrm{B}} \widehat{\mathbf{S}} \tag{4.3}$$

where $g_0 = 2$ is the numerical value of the electron vacuum Landé factor (without corrections from quantum electrodynamics) and

$$\mu_{\mathrm{B}} = \frac{\hbar |e|}{2 m_0} \tag{4.4}$$

is the Bohr magneton, defined using the electronic charge e and electronic vacuum mass m_0.

For carriers in crystal lattices, the Landé factor is not a fundamental quantity as for the free electron, but is a quasi-particle property like the effective mass and is therefore drastically influenced by details of the band-structure. Caculations via $\mathbf{k} \cdot \mathbf{p}$ perturbation theory[5] tend to be complicated since higher electron bands need to be taken into account[42,43] to explain experimental data.[44] Therefore we take the commonly accepted[45] effective electron Landé factor for GaAs $g_{\mathrm{e}} = -0.44$

*We also use $s = \uparrow, \downarrow$ instead.

in the same spirit in which we use the empirical Luttinger mass parameters. Then the electronic magnetic moment is given in terms of the spin **S** by

$$\widehat{\boldsymbol{\mu}} = g_{\mathrm{e}}\mu_{\mathrm{B}}\,\widehat{\mathbf{S}}. \tag{4.5}$$

Since the x component of the electron spin operator is related to the spin raising and lowering operators $\widehat{S}_{\pm}$ via

$$\widehat{S}_x = \frac{1}{2}(\widehat{S}_+ + \widehat{S}_-) \tag{4.6}$$

we find from equation (4.5)

$$\langle s|\widehat{\mu}_x|s'\rangle\, B = \hbar\omega_{\mathrm{L}} \begin{cases} \frac{1}{2} & \text{if } s \neq s' \,, \\ 0 & \text{if } s = s' \,, \end{cases} \tag{4.7}$$

with the Larmor energy defined by

$$\hbar\omega_{\mathrm{L}} \equiv g_{\mathrm{e}}\mu_{\mathrm{B}}B. \tag{4.8}$$

In the geometry chosen here, the heavy holes are not influenced by the magnetic field since using $\widehat{J}_x = \frac{1}{2}(\widehat{J}_+ + \widehat{J}_-)$ on angular momentum states with total angular momentum $J = \frac{3}{2}$ and projection quantum number $j = \pm\frac{3}{2}$ yields always

$$\left\langle j|\widehat{\mu}_x|j'\right\rangle = 0. \tag{4.9}$$

Electron-hole transitions are not driven by the magnetic field either since states with different total angular momenta $S \neq J$ are orthogonal. Therefore, the magnetic dipole interaction equation (4.2) becomes

$$\widehat{H}_{\mathrm{mag}} = -\frac{\hbar\omega_{\mathrm{L}}}{2} \sum_{s=\pm 1/2} \sum_{\mathbf{k}} c_s^{\dagger}(\mathbf{k})\, c_{-s}(\mathbf{k}) \,. \tag{4.10}$$

4.3. Carrier Dynamics with Magnetic Field

In Chapter 2 the electric dipole Hamiltonian acted as a driving field for the coherent electron-hole transition amplitude. In much the same way the static magnetic field drives a coherent transition amplitude between the two electron bands. In order to distinguish between the two transition amplitudes we refer to the electron-electron coherence as "Larmor polarization". The Larmor polarization is defined in generalization of the interband case, equation (2.7), by the off-diagonal element of the electronic density matrix $\rho_{ss'}(\mathbf{k})$

$$\psi_{ss'}(\mathbf{k}) = \rho_{ss'}(\mathbf{k}) \equiv \langle c_s^{\dagger}(\mathbf{k}) c_{s'}(\mathbf{k})\rangle \qquad (\text{for } s \neq s') \,. \tag{4.11}$$

Here, no spatial dispersion is present and the transition amplitude depends only on the relative wavevector variable $\mathbf{k}$. Since $\psi_{s\bar{s}} = (\psi_{\bar{s}s})^*$ for $\bar{s} = -s$ we keep only one complex dynamical Larmor polarization $\psi \equiv \psi_{\uparrow\downarrow}$.

The dynamical Hartree-Fock approximation yields then the equation of motion for the transition amplitude

$$i\hbar\frac{\partial}{\partial t}\psi(\mathbf{k}) = [\varepsilon_{\mathrm{L}}(\mathbf{k}) + i\gamma_{\mathrm{spin}}]\psi(\mathbf{k}) - \hbar\Omega_{\mathrm{L}}(\mathbf{k})\left[f_{\uparrow}(\mathbf{k}) - f_{\downarrow}(\mathbf{k})\right] \tag{4.12}$$

with the renormalized Larmor frequencies

$$\hbar\Omega_{\mathrm{L}}(\mathbf{k}) = \frac{1}{2}\hbar\omega_{\mathrm{L}} - \frac{1}{\mathscr{A}}\sum_{\mathbf{k}'} V(|\mathbf{k}-\mathbf{k}'|)\,\psi(\mathbf{k}'). \tag{4.13}$$

and the free polarization rotation due to the Coulomb Potential:

$$\varepsilon_{\mathrm{L}}(\mathbf{k}) = -\frac{1}{\mathscr{A}}\sum_{\mathbf{k}'} V(|\mathbf{k}-\mathbf{k}'|)\left[f_{\uparrow}(\mathbf{k}') - f_{\downarrow}(\mathbf{k}')\right]. \tag{4.14}$$

Here we have used the quasi two-dimensional Coulomb-potential for the ideal quantum-well case

$$V(q) = \frac{e^2}{2\varepsilon_0 n_{\mathrm{bg}}^2}\frac{1}{q} \tag{4.15}$$

with the normalization area $\mathscr{A}$ of the quantum well and the refractive index of the semiconductor material n_{bg}. Also, a phenomenological spin dephasing rate γ_{spin} has been added. The carrier distribution functions are defined as the diagonal elements of the spin density matrix

$$f_s(\mathbf{k}) = \rho_{ss}(\mathbf{k}) \equiv \langle c_s^\dagger(\mathbf{k})c_s(\mathbf{k})\rangle\ . \tag{4.16}$$

To obtain a closed set of equation we also need to derive the Hartree-Fock equations for these carrier distributions:

$$\frac{\partial}{\partial t}f_{\uparrow}(\mathbf{k})\bigg|_B = -\frac{\partial}{\partial t}f_{\downarrow}(\mathbf{k})\bigg|_B = 2\,\mathrm{Im}\left[\Omega_{\mathrm{L}}^*(\mathbf{k})\,\psi(\mathbf{k})\right]. \tag{4.17}$$

Here, the subscript B indicates that this is the contribution to the dynamics from the transverse magnetic field.

Note again, that the Larmor polarization $\psi(\mathbf{k})$ is a correlation which couples only the electronic distribution functions (4.16). When there are coherent optical transitions from electrons to hole bands these are described in the framework of

the Semiconductor Bloch equations (SBE).[5,28] For the interband polarization we obtain here the local k space version of equation (2.8)

$$i\bar{h}\frac{\partial}{\partial t}\Psi_{js}(\mathbf{k}) = [\varepsilon_{js}(\mathbf{k}) + i\gamma_{\mathrm{opt}}]\Psi_{js}(\mathbf{k}) + \bar{h}\Omega_{sj}(\mathbf{k})[1 - f_s(\mathbf{k}) - f_j(\mathbf{k})] \tag{4.18}$$

with the renormalized Rabi energy

$$\bar{h}\Omega_{sj} \equiv \mathbf{d}_{sj}\cdot\mathbf{E}_{\mathrm{QW}} + \frac{1}{\mathscr{A}}\sum_{\mathbf{k}'} V(|\mathbf{k}-\mathbf{k}'|)\Psi_{js}(\mathbf{k}') \tag{4.19}$$

and the interband energies

$$\varepsilon_{js}(\mathbf{k}) = E_{\mathrm{G}} + \varepsilon_{\mathrm{e}}(k) + \varepsilon_{\mathrm{h}}(k) - \frac{1}{\mathscr{A}}\sum_{\mathbf{k}'} V(|\mathbf{k}-\mathbf{k}'|)[f_s(\mathbf{k}) + f_j(\mathbf{k})] \tag{4.20}$$

with the gap energy E_{G} and the electron and hole dispersions, $\varepsilon_{\mathrm{e}}(k)$ and $\varepsilon_{\mathrm{h}}(k)$, respectively. In equation (4.19) the confinement of the quantum well has been taken into account using the quantum-well envelope functions $\xi(z)$ by defining

$$\mathbf{E}_{\mathrm{QW}} \equiv \int dz\,|\xi(z)|^2\mathbf{E}(z) \simeq \mathbf{E}(z=0) \tag{4.21}$$

if the quantum well is located at $z = 0$. The Coulomb potential is again given by equation (4.15) and a corresponding optical dephasing constant γ_{opt} has been added. The system of differential equations is again closed by the equations for the electron and hole carrier distributions

$$i\frac{\partial}{\partial t}f_s(\mathbf{k})\big|_E = i\frac{\partial}{\partial t}f_j(\mathbf{k})\big|_E = -2\mathrm{Im}[\Omega^*_{js}\Psi_{js}]\,. \tag{4.22}$$

The formal similarities of the equations for the intra-electron-band dynamics described by equations (4.12) and (4.17) on the one hand and equations (4.18) and (4.22) on the other hand are striking. For a coherent optical field, equations (4.18) and (4.22) describe the excitation of electrons from the valence band to the conduction band during one half of an optical cycle and the reabsorption of the energy by the field leading to the reverse effect for the carriers during the next half of the optical cycle. In the same way, equations (4.18) and (4.22) describe the depopulation of one of the electron bands and an increased population of the other by the magnetic field during the first half of the cycle and the reverse effect during the second half. This can be seen in figure 4.2 (top) where the computed total density for both electron bands $s = \pm\frac{1}{2}$ is shown after the excitation of the quantum well and a Larmor precession period $T_{\mathrm{L}} \equiv 2\pi/\omega_{\mathrm{L}} = 70\,\mathrm{ps}$. The optical pump pulse has a full width at half maximum of 2 ps and is centered at $t = 0$. The phenomenological spin dephasing rate is taken to be zero.

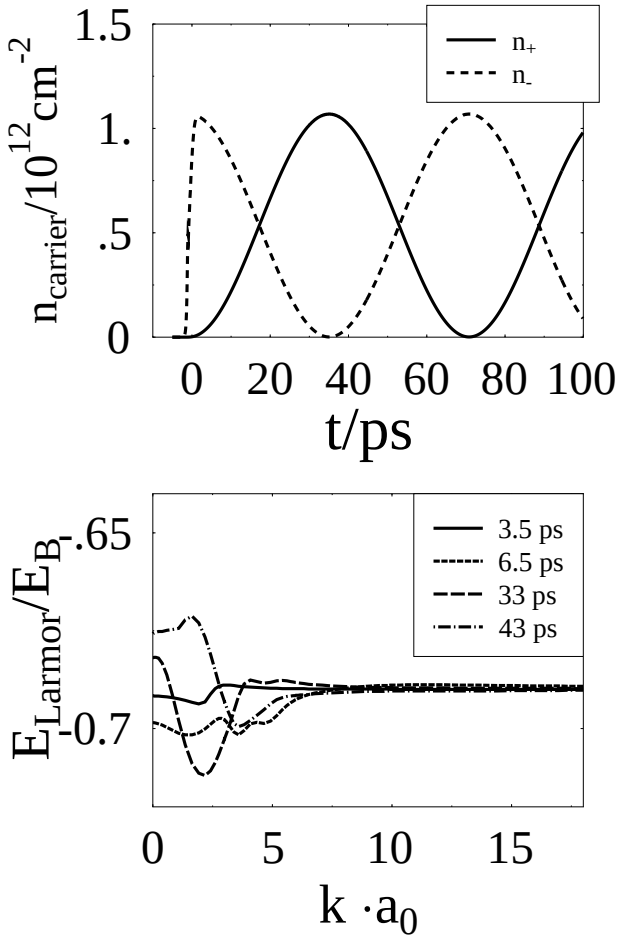

Figure 4.2.: Top: Computed time evolution of carrier densities in the electron bands after short-pulse excitation. Bottom: Wave-vector dependence of the renormalized Larmor energy (4.13) at various times.

In equation (4.19), the optical Rabi energy is renormalized by the Coulomb interaction and the Coulomb effects dominate the dynamics of the optical transition amplitude. For instance, excitonic resonances and the enhancement of the absorption at the band edge in the low density regime and the enhancement of the optical gain in the high density regime[5] are entirely due to Coulomb effects. Thus one would expect that the equivalent renormalizations lead to qualitative changes of the Larmor frequency. However, studying the time evolution of the densities in figure 4.2(top) shows that for the Larmor polarization the Coulomb effects are not as drastic as in the case of the electron-hole amplitude and modifications of the time-dependent carrier density shown in figure 4.2 remain small. This can also be seen in the bottom part of figure 4.2 where the renormalized

Larmor frequency is plotted as a function of the electron momentum for various times: The k resolved difference between the Larmor frequency and the renormalized Larmor frequency does not become appreciable during the time evolution, in contrast to the optical polarization where this renormalization is dominant. The reason for the difference is the energy dispersion of the carrier states involved with the respective polarizations. For optical transitions, i.e., the electron-hole interband polarization, this dispersion is present leading to a free "rotation" of Ψ. For magnetic transitions between the electron bands, which involve the Larmor polarization (4.11), there is no dispersion entering equation (4.12). That is, in the magnetic case, the Coulomb interaction does not couple *different* resonance energies as it does in the optical case. Therefore the resulting Coulomb contributions to the Larmor frequency are not as important as for optical transitions. Qualitatively this behavior can be illustrated using the Fourier transformed Larmor polarization $\psi(\omega, \mathbf{k})$. Neglecting all Coulomb contributions the Fourier transformation of equation (4.12) results in

$$\psi(\omega, \mathbf{k}) = \frac{\hbar\omega_{\mathrm{L}}}{\hbar\omega + i\gamma_{\mathrm{spin}}}[f_{\uparrow}(\mathbf{k}) - f_{\downarrow}(\mathbf{k})]. \tag{4.23}$$

Since the denominator in equation (4.23) does not have an intrinsic $\mathbf{k}$ dependence the Coulomb sum over $\mathbf{k}'$ in equation (4.13) does not couple different resonances of the system. For the optical polarization this is the case because there $\hbar\omega$ is replaced by $\hbar\omega - \varepsilon_{\mathrm{e}}(\mathbf{k}) - \varepsilon_{\mathrm{h}}(\mathbf{k})$. Therefore the resonances of the Larmor polarization are not altered to the same extent as the resonances of the optical polarization are altered by Coulomb effects.

The results derived here will be applied in the next chapter to the emission dynamics of a microlaser in a transverse magnetic field. In the remainder of this chapter we will present a method[12] to determine the Landé factor in semiconductor heterostructures because it furnishes an extremely simple example for the application of the Larmor polarization.

4.4. Perpendicular Optical Excitation in Voigt Geometry

As discussed above, in semiconductors the electronic Landé factor, denoted by g_{e}, is not a fundamental quantity but varies from large negative values to $g_0 = 2$ of the free electron. The carrier dynamics in magnetic fields is therefore not only determined by the direction of the magnetic field but also by the detailed material properties of the semiconductor which influence both the magnitude and the sign of the Landé factor. In particular, it is not sufficient to determine the magnitude of g_{e} but one also must have access to its sign.

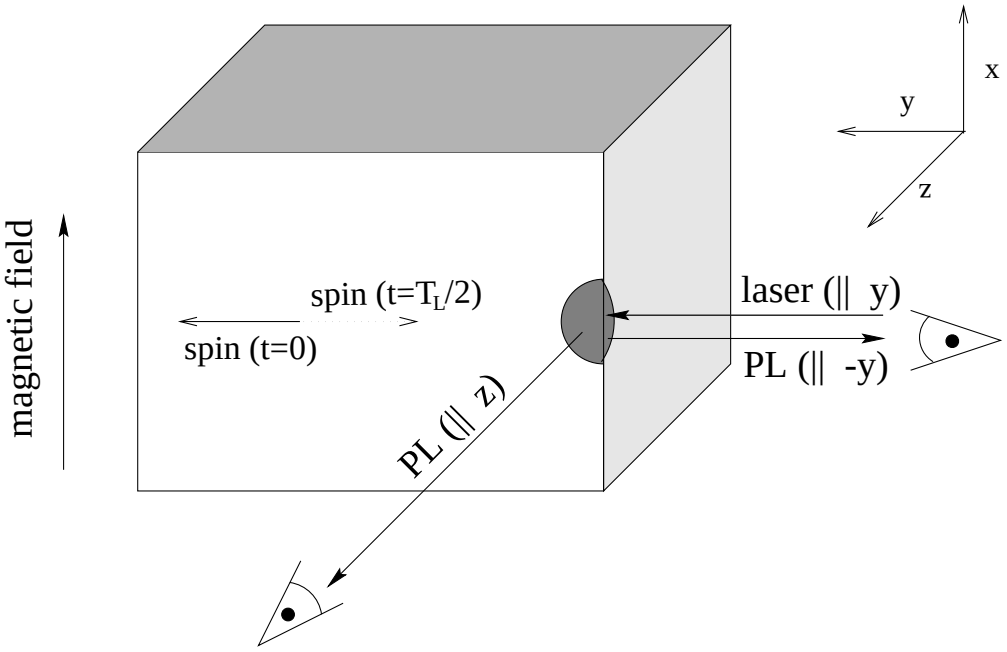

Figure 4.3.: Voigt geometry for perpendicular optical excitation with circularly polarized light along the $+y$ direction creating a mean spin $\langle \hat{s}_y \rangle (t = 0)$. Observation in $-y$ direction antiparallel to the excitation does not yield photoluminescence oscillations since $\langle \hat{s}_y \rangle (t)$ is the same for both $\pm g_e$. However, observation in $+z$ direction *perpendicular* to the excitation yields a phase difference of π in $\langle \hat{s}_z \rangle (t)$ for different signs of g_e. This is directly visible as a phase shift of the emitted luminescence.[12]

While the determination of the absolute value of g_e is straightforward by measuring the Zeeman splitting, the sign of g_e proved to be more difficult. For example, the sign of g_e at the conduction band minimum Γ_c^6 in GaAs has been discussed controversially for a long time.[46]

We will illustrate here how to calculate the electronic spin dynamics in a magnetic field after perpendicular optical excitation. The resulting spin polarization which is connected to the optical polarization of the emitted luminescence then directly yields the direction of the spin precession in semiconductors. Figure 4.3 shows the Voigt geometry with perpendicular optical excitation. The growth direction of the sample is along the *z* axis, i.e., the quantum-well is parallel to the *x*-*y* plane. The magnetic field is aligned perpendicular to the growth direction along the *x* axis. Optical excitation and detection is along the *y* axis. The important new feature of this configuration is that detection is performed *perpendicular to both* magnetic field and excitation.

We will first discuss the optical electron-hole excitation process in this con-

figuration taking into account the optical dipole selection rules for the various transitions. We then calculate the spin dynamics under the influence of the magnetic field in bulk and quantum well structures and use the result to analyze the luminescence emitted from the sample after excitation.

4.4.1. Optical Excitation

Since the conduction-band degeneracy is only due to its spin degree of freedom the dynamics of the electron spins in a magnetic field is not influenced by the different symmetries of bulk and quantum well materials. However, as discussed in chapter 2 and above, the definition of the hole states involves the angular momentum projection quantum number j, which is defined with respect to a definite quantization direction. In bulk materials we could choose this quantization axis arbitrarily, but for quantum wells the rotational symmetry around the growth axis leads to the natural choice of the growth axis (z axis) as the quantization axis. In particular, the usual optical dipole selection rules for quantum wells are defined only with respect to angular momentum projection quantum numbers in z direction. Working with z as the quantization axis the following discussion applies equally well to bulk and quantum well structures. For definiteness, we choose the more intriguing quantum-well case for the calculation and comment on differences in the bulk case later.

We first establish the initial conditions for the magnetic field dynamics, which are created by the polarized optical excitation. The applied optical pulse drives the interband polarization $\Psi_{js}(\mathbf{k})$ of the light-hole bands and the electrons.[5] The vectorial dipole matrix elements $\mathbf{d}_{sj}$, as shown in figure 4.4, lie in the x-y plane for both electron to light-hole (e-lh) and electron to heavy-hole (e-hh) transitions

$$\mathbf{d}_{\uparrow,3/2} = \sqrt{3}\mathbf{d}_{\downarrow,+1/2} = -d_{\mathrm{cv}}\boldsymbol{\sigma}_{+} \tag{4.24}$$

$$\mathbf{d}_{\downarrow,-3/2} = \sqrt{3}d_{\uparrow,+1/2} = d_{\mathrm{cv}}\boldsymbol{\sigma}_{-} \ , \tag{4.25}$$

or are directed along the z axis

$$\mathbf{d}_{\downarrow,-1/2} = \mathbf{d}_{\uparrow,1/2} = \sqrt{\frac{2}{3}}d_{\mathrm{cv}}\mathbf{e}_z \tag{4.26}$$

for e-lh transitions only. Here, $\boldsymbol{\sigma}_{\pm} = \frac{1}{\sqrt{2}}(\mathbf{e}_x \pm i\mathbf{e}_y)$ denote the polarization vectors in the x-y plane and d_{cv} is the magnitude of the microscopic Cartesian dipole moment. In our configuration, the electron-hole transitions are induced by a laser field that is circularly polarized in the x-z plane and propagating along the y axis. Hence, the exciting laser field is given by

$$\mathbf{E}(t) = E_{\mathrm{exc}}(t)\frac{\mathbf{e}_x - i\mathbf{e}_z}{\sqrt{2}} \equiv E_{\mathrm{exc}}(t)\,\boldsymbol{\sigma}_{-}^{(y)} \ . \tag{4.27}$$

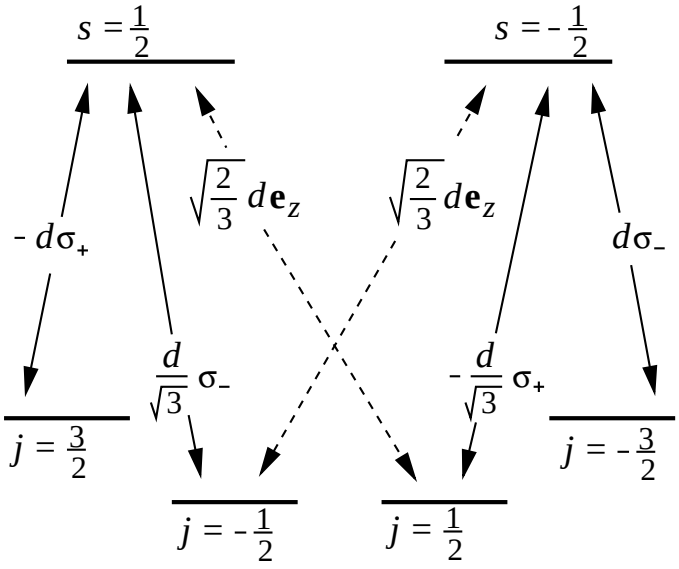

Figure 4.4.: Selection rules for optical transitions between light hole ($j = \pm\frac{1}{2}$), heavy hole ($j = \pm\frac{3}{2}$) and electron ($s = \pm\frac{1}{2}$) bands. Here, $d \equiv d_{\mathrm{cv}}$ is the magnitude of the microscopic dipole moment and $\boldsymbol{\sigma}_\pm \equiv \frac{1}{\sqrt{2}}(\mathbf{e}_x \pm i\mathbf{e}_y)$ the complex basis vectors describing $\sigma_\pm$ polarizations in the *x*-*y* plane.

We determine the excitation of the electrons by a coherent conservation law[27] valid in the low-density limit which connects the electron density matrix $\rho_{ss'}(\mathbf{k})$ to the interband transition amplitude $\Psi_{js}(k)$ via :

$$\rho_{ss'}(\mathbf{k}) = \sum_j \Psi_{js}(\mathbf{k})\Psi^*_{s'j}(\mathbf{k}). \tag{4.28}$$

Using equations (4.11) and (4.16) we obtain the electron density in the bands *s*

$$n_s = \sum_{\mathbf{k}} \rho_{ss}(\mathbf{k}) \tag{4.29}$$

and the Larmor polarization

$$p \equiv \sum_{\mathbf{k}} \psi_{\uparrow\downarrow}(\mathbf{k}) = \sum_{\mathbf{k}} \rho_{\uparrow\downarrow}(\mathbf{k}). \tag{4.30}$$

Note that $\psi_{\downarrow\uparrow} = \psi^*$. In the following we expand the electron-hole transition amplitude

$$\Psi_{js}(\mathbf{k}) = \sum_n \Psi^{(n)}_{js}\, \varphi_n(\mathbf{k}) \tag{4.31}$$

with respect to exciton basis functions $\varphi_n(\mathbf{k})$, which are analogous[5] to the eigenfunctions defined in equation (3.4) but depend here on the two-dimensional momentum vector $\mathbf{k}$. Retaining only the $n = 0$ (1s-exciton) components, $\Psi^{(0)}_{js}$, we obtain for the observable spin density-matrix

$$\rho_{ss'} \equiv \sum_{\mathbf{k}} \rho_{ss'}(\mathbf{k}) \approx \frac{1}{\mathscr{N}} \sum_{j} \Psi^{(0)}_{js} \left(\Psi^{(0)}_{s'j}\right)^{*} \sum_{\mathbf{k}} |\varphi_0(\mathbf{k})|^2 \,, \tag{4.32}$$

where we have included a normalization factor $\mathscr{N}$ for the density matrix. Using the equation of motion for the 1s-exciton polarization[5] we obtain for times t longer than the pulse duration τ

$$\Psi^{(0)}_{js}(t) = i \sum_{\mathbf{k}} \varphi_0(\mathbf{k})\, \Theta_{sj}(t) \qquad (\text{for } t > \tau) \,, \tag{4.33}$$

where

$$\hbar\Theta_{sj}(t) = \int_{-\infty}^{t} \mathbf{d}_{sj} \cdot \mathbf{E}(t')dt' \tag{4.34}$$

is the area of the excitation pulse for the transition $j \to s$. The most important information contained in equations (4.33) and (4.34) is the coupling of the electric field vector (4.27) to the vectorial dipole moments. Therefore, we write equation (4.33) as

$$\Psi^{(0)}_{js} = i\big(\mathbf{d}_{sj} \cdot \boldsymbol{\sigma}^{(y)}_{-}\big)\, \frac{1}{d_{\mathrm{cv}}} \sum_{\mathbf{k}} \varphi_0(\mathbf{k})\, \hbar\Theta \tag{4.35}$$

with the area of the excitation pulse $\hbar\Theta(t) = d_{\mathrm{cv}} \int_{-\infty}^{t} E_{\mathrm{L}}(t')dt'$.

The calculation of the coherent optical excitation and of the spin dynamics can be decoupled to a good approximation since the relevant time scales are very different, i.e., the excitation pulse duration $\tau = 1\mathrm{ps} \ll T_L \simeq 100\mathrm{ps}$, where T_{L} is the Larmor precession time. We now use equation (4.35) in equation (4.32) to determine the initial values of the electron distributions

$$n_{\uparrow}(t=0) = n_{\downarrow}(t=0) = \frac{1}{2} \qquad (\text{for arbitrary excitation}) \tag{4.36}$$

and the Larmor polarization

$$p_0 \equiv p(t=0) = -\frac{2}{5}i \qquad (\text{for e-lh excitation}) \,, \tag{4.37}$$

valid for the *light-hole to electron transition.*

For the *heavy-hole to electron transition*, we obtain again equation (4.36), i.e., equal distributions for spin-up and spin-down electrons but

$$p_0 \equiv p(t=0) = 0 \qquad \text{(for e-hh excitation)}\,, \tag{4.38}$$

i.e., a vanishing magnetic polarization for the e-hh transition. For excitation of both light-hole and heavy-hole transition the normalization of the density matrix ensures that equation (4.36) still holds but the Larmor polarization is now given by

$$p_0 \equiv p(t=0) = -\frac{i}{10} \qquad \text{(for e-lh and e-hh excitation)}\,. \tag{4.39}$$

These values for $n_\uparrow$, $n_\downarrow$ and p are taken as the $t = 0$ initial values for the spin dynamics. Using equations (4.12) and (4.17) we obtain after $\mathbf{k}$ summation and neglection of the Coulomb renormalizations

$$\frac{d}{dt} n_\uparrow(t) = -\frac{d}{dt} n_\downarrow(t) = \operatorname{sign}(g_\mathrm{e})\, \omega_\mathrm{L}\, \operatorname{Im} p(t) \tag{4.40}$$

$$i\frac{d}{dt} p(t) = \operatorname{sign}(g_\mathrm{e}) \frac{\omega_\mathrm{L}}{2} (n_\uparrow(t) - n_\downarrow(t)). \tag{4.41}$$

Equations (4.40) and (4.41) are just a disguised oscillator equation for the inversion $\Delta n(t) = n_\uparrow(t) - n_\downarrow(t)$ which is independent of the sign of g_e

$$\frac{d^2}{dt^2} \Delta n(t) = -\omega_\mathrm{L}^2 \Delta n(t). \tag{4.42}$$

The solution is for the given initial conditions

$$\Delta n(t) = \operatorname{sign}(g_\mathrm{e})\ (-2ip_0) \sin(\omega_\mathrm{L} t) \tag{4.43}$$

$$p(t) = p_0 \cos(\omega_\mathrm{L} t)\,. \tag{4.44}$$

4.4.2. Spin Polarization

The semiconductor luminescence equations[47,48] yield the photoluminescence that is emitted in the photon modes $\mathbf{q}$. Ignoring all Coulomb renormalization effects, we obtain from these equations that the time evolution of the σ_+ (σ_-) photoluminescence-component emitted in an arbitrary direction is governed by the average number of electrons with spin parallel (anti-parallel) to that direction and the dipole matrix elements. On the time scales considered here, there is no hole contribution since the holes lose their angular momentum in a magnetic

field due to the strong spin-orbit coupling significantly faster than the electrons.[49] Under these conditions, the degree of optical polarization in z direction

$$P_{\mathrm{opt},z} = \frac{I_+ - I_-}{I_+ + I_-} \tag{4.45}$$

is determined only by the electronic spin polarization

$$P_{\mathrm{spin},z}(t) \equiv \frac{n_\uparrow(t) - n_\downarrow(t)}{n_\uparrow(t) + n_\downarrow(t)} = \Delta n(t). \tag{4.46}$$

Since the inversion Δn from equation (4.43) is proportional to the sign of g_e the time evolution of $P_{\mathrm{opt},z}$ shows directly the sign of g_e. Equation (4.46) together with equation (4.43) yield an extremal polarization for $T_L/4$, where $T_\mathrm{L} = 2\pi/\omega_\mathrm{L}$ is the Larmor period. Depending on the respective excitation conditions (4.38), (4.37) or (4.39), we obtain $|P_{\mathrm{spin},z}(T_L/4)| = 0\%$, i. e. no effect, for resonant e-hh excitation, $|P_{\mathrm{spin},z}(T_L/4)| = 80\%$ for resonant e-lh excitation, and $|P_{\mathrm{spin},z}(T_L/4)| = 20\%$ for excitation into the hh and lh continuum.

This method has been used to show directly the reversal of the electron Landé factor in quantum wells of different thickness. For this purpose a sample was fabricated consisting of two GaAs quantum wells with a well width of 5 nm and 10 nm, respectively, and 30 nm $Al_{0.3}Ga_{0.7}As$ barriers. The widths were chosen because previous experiments indirectly yielded a negative g_e for quantum wells wider than 5.5 nm and a positive g_e for quantum wells narrower than 5.5 nm.[50] Excitation was performed into the continuum of the quantum wells with circularly polarized light propagating perpendicular to the growth direction and magnetic field. The photoluminescence was detected perpendicular to the magnetic field and excitation direction and parallel to the growth direction. Figure 4.5 depicts the time-resolved $P_{\mathrm{opt},z}$, cf. equation (4.45), for both quantum wells. A phase difference of π is clearly visible shortly after excitation, demonstrating the opposite signs of g_e in the different quantum wells. The measurement proves that the experiment together with its theoretical interpretation presented here makes the determination of g_e factors feasible in low dimensional systems.

Finally, we would like to comment on the bulk case for which the analysis given here is also valid. In addition to the results derived above, one can explore easily the dynamics of the expectation values $\langle s_\alpha \rangle$ of the Cartesian spin component $\alpha = x, y, z$. The connection between these mean spins and the magnetic polarization is given by

$$p = \langle \widehat{s}_x \rangle + i \langle \widehat{s}_y \rangle \tag{4.47}$$

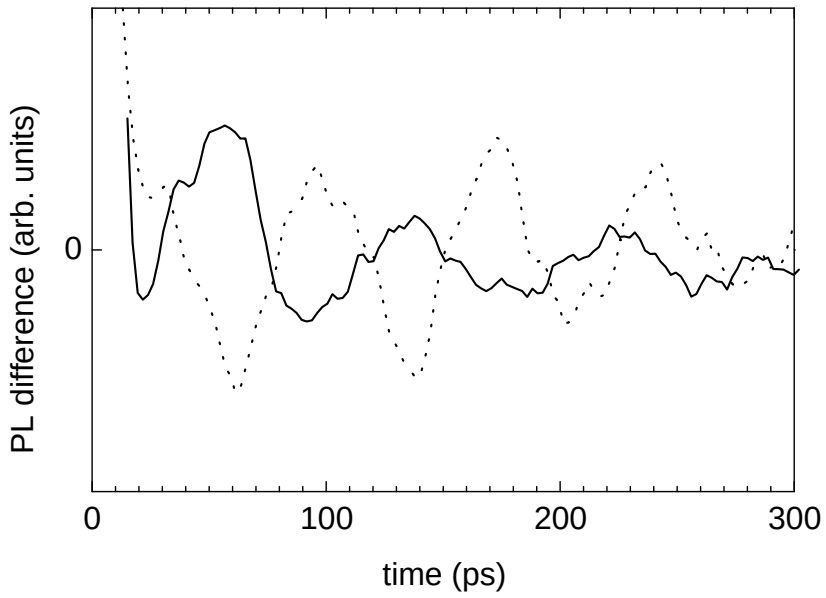

Figure 4.5.: Experimental luminescence (from Ref. 12): Difference signal of σ^+ and σ^- photoluminescence in a 5 nm (solid line) and 10 nm quantum well (dotted line) at a magnetic field of 6 T. The phase difference of π between the photoluminescence oscillations results from the different sign of g_e. The oscillation frequencies are slightly different because the absolute values of g_e are not the same ($g_e = 0.143$ in the 5 nm quantum well and $g_e = -0.165$ in the 10 nm quantum-well). The large signal at $t = 0$ is due to scattered laser light.

since we have, by definitions (4.11) and (4.30), $p = \langle \widehat{s}_+ \rangle$ with $\widehat{s}_+ = \widehat{s}_x + i\widehat{s}_y$. Therefore

$$\langle \widehat{s}_x \rangle(t) = \mathrm{Re}\, p(t), \tag{4.48}$$

$$\langle \widehat{s}_y \rangle(t) = \mathrm{Im}\, p(t) \tag{4.49}$$

and $\langle \widehat{s}_z \rangle$ is simply given by

$$\langle \widehat{s}_z \rangle(t) = \frac{1}{2}\left[n_\uparrow(t) - n_\downarrow(t) \right] \equiv \frac{1}{2}\Delta n(t)\ . \tag{4.50}$$

Because the connection between the inversion δ, the magnetic polarization p and the average spin is given by equations (4.48)–(4.50) our solutions (4.43) and (4.44) describe a mean spin $\langle \widehat{\mathbf{s}} \rangle(t)$ precessing in the y-z plane as indicated in figure 4.3.

Using equations (4.46) and (4.50) we first obtain

$$P_{\mathrm{spin},z}(t) = 2\langle \widehat{s}_z \rangle(t) \tag{4.51}$$

and exploiting the full rotational symmetry of a bulk configuration yields that the photoluminescence in direction $\alpha = x, y, z$ is determined by the spin polarization

$$P_{\mathrm{spin},\alpha}(t) = 2\langle \widehat{s}_\alpha \rangle(t) \ . \tag{4.52}$$

Therefore, the sign of g_e is visible in the optical polarization for observation in z direction, but not in y direction, as can be seen by calculating the spin polarization in y direction

$$P_{\mathrm{spin},y}(t) = 2\langle \widehat{s}_y \rangle(t) = 2\,\mathrm{Im}\, p(t) = -\frac{4}{5}\cos(\omega_L t), \tag{4.53}$$

which is independent of the sign of g_e. These consideration also show that the photoluminescence emitted in the direction backward to the excitation is, in the bulk case and even without applied magnetic field, also partially circularly polarized. The photoluminescence perpendicular to the excitation without applied magnetic field is not circularly polarized since the average spin projection in x direction is always zero,

$$P_{\mathrm{spin},x}(t) = 2\langle \widehat{s}_x \rangle(t) = 2\,\mathrm{Re}\, p(t) = 0 \ . \tag{4.54}$$

5. Laser Dynamics with Magnetic Field

In this chapter we will analyze the emission dynamics of a quantum well in a microresonator in the presence of a transverse magnetic field. We therefore briefly discuss the microlaser and its physical properties first, leaving the details of the laser model to Appendix C. Next, the carrier-carrier interaction and the interaction of carriers with the crystal lattice is examined because these complicated mechanisms are crucial for the laser dynamics but make the problem numerically very demanding. For the purposes of the present chapter we therefore need to introduce some approximations to make the problem tractable.

We then use these ingredients to present numerical results for the microlaser dynamics in a transverse magnetic field after pulse excitation. The physical processes are discussed and it is shown how the dynamics of the laser can be controlled by higher magnetic fields and different excitation conditions. A comparison to experimental results is also included.

5.1. Outline of Microlaser Theory

The Voigt geometry for the quantum-well laser with magnetic field is shown in figure 5.1. The static magnetic field points in x-direction, $\mathbf{B} = B\mathbf{e}_x$, and is *perpendicular* to the growth direction z of the quantum well. Because of its small resonator and the high reflectivities of the distributed Bragg structures, which form the cavity mirrors, microlasers can be designed to operate on a single longitudinal-mode. That is, due to the large mode spacing only one longitudinal mode lies the spectral region where optical gain is produced by the carrier system.

We are interested here in the laser dynamics over a few hundred picoseconds in experimentally accessible magnetic field strengths, which lead to Larmor periods of several tens of picosends. On these timescales it is not numerically feasible to apply a microlaser theory which describes the microscopic non-equilibrium carrier dynamics and the interaction with a quantized field in the resonator.[51,52] Such a theory can explain the microlaser action down to very short timescales and, in particular, the switch-on behavior after ultrashort-pulse excitation.[53,54]

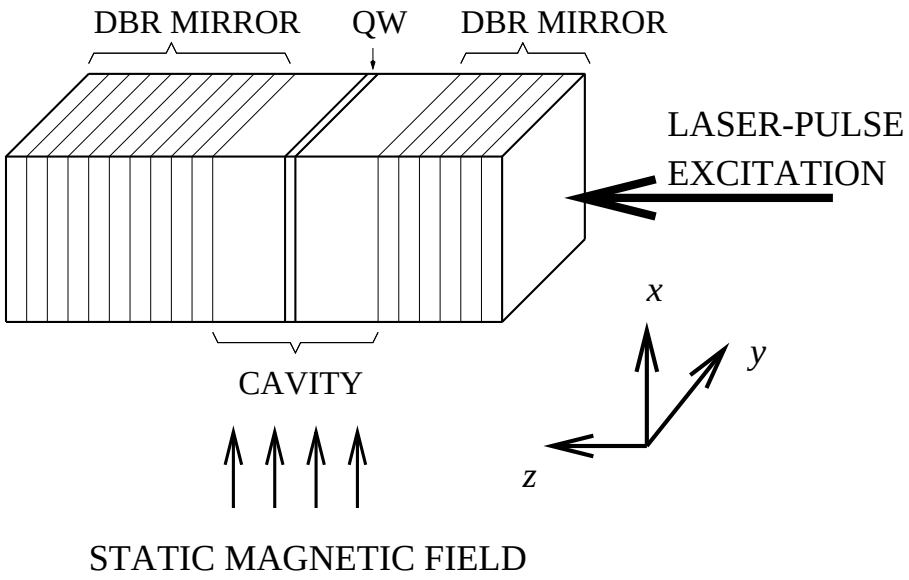

Figure 5.1.: Schematic picture of a surface-emitting quantum-well microlaser in a magnetic field. The length of the cavity is typically on the order of an optical wavelength. The distributed Bragg-reflectors, which serve as cavity mirrors, consist of quarter-wave layers of alternating refractive index. Excitation of the structure and laser emission is along the z axis. The magnetic field is aligned perpendicular to the growth direction.

Also luminescence properties are included by treating the electromagnetic field quantum-mechanically.

For the present purposes, therefore, we use a simpler semi-classical model for the microlaser summarized in Appendix C. In this model, the laser dynamics is described by the intensity at the cavity resonance $I(t)$. The stimulated contribution to the intensity is given by

$$\frac{\partial}{\partial t} I(t)\bigg|_{\text{stim}} = g_{\text{cav}}(t) I(t) - \kappa I(t) \tag{5.1}$$

where g_{cav} is the gain at the cavity resonance, cf. equation (C.10), and the constant κ models the cavity losses. The computation of the gain from the carrier distributions is a complicated many-body problem. Here, the gain is calculated by an integral equation derived from the semiconductor Bloch equations. For stimulated emission to occur, it is necessary that the gain overcompensates the cavity loss. This is only possible if the carriers reach inversion at the cavity resonance. Technically speaking, we must have $f_{\text{e}}(k) - f_{\text{h}}(k) - 1 > 0$, for interband energies $E_{\text{g}} + \varepsilon_{\text{e}}(k) + \varepsilon_{\text{h}}(k)$ in the vicinity of the cavity resonance before stimulated emission can set in. The discussion of the laser behavior in a magnetic field will be based on this fact to a large extent.

5.2. Incoherent Carrier Dynamics

The time evolution of the laser emission is dominated by incoherent processes, such as carrier scattering and thermalization. The fast electron-electron scattering drives the non-equilibrium carrier distributions towards an equilibrium state described by Fermi functions. Furthermore the electron-hole scattering process redistributes the kinetic energy of the carriers between electron and hole bands. Both processes, however, do not dissipate energy from the carrier system. Only the interaction of the carrier system with the crystal lattice transfers energy from the electron-hole system to the lattice. Since the fast scattering processes take place on picosecond and sub-picosecond timescales but we are interested here in the dynamics on the ten-picosecond timescale set by the magnetic field, we approximate the complicated microscopic scattering and thermalization mechanisms by scattering rates. That is, we assume that the fast Coulomb scattering leads to an equilibration of carriers between all the bands on the timescale τ_{scatt} and the interaction with the crystal lattice leads to a thermalization on a timescale τ_{therm}

$$\frac{\partial}{\partial t} f(\mathbf{k},t)\Big|_{\text{inc}} = -\frac{f(\mathbf{k},t) - f_{\text{scatt}}(\mathbf{k},t)}{\tau_{\text{scatt}}} - \frac{f(\mathbf{k},t) - f_{\text{therm}}(\mathbf{k},t)}{\tau_{\text{therm}}} \,. \tag{5.2}$$

Here, f_{scatt} and f_{therm} are *Fermi distributions* which are computed from the non-equilibrium carrier distributions at any given time t. Technically, we first compute the temperatures and chemical potentials of Fermi distributions with the same number and energy density as the non-equilibrium carrier distributions. From this we determine the average temperature T_{scatt} and calculate f_{scatt} as the Fermi function with temperature T_{scatt} and the number density of the non-equilibrium distribution f in the corresponding band. This is an effective model for electron-electron and electron-hole scattering. The Fermi function f_{therm} is computed using the number density of f together with a temperature T_{therm}. We do not assume the lattice temperature for T_{therm} since the carriers never come near to equilibrium with the lattice before and during the laser action.[55] As can be seen by calculating

$$\frac{\partial}{\partial t} n(t)\Big|_{\text{inc}} = \sum_{\mathbf{k}} \frac{\partial}{\partial t} f(\mathbf{k},t)\Big|_{\text{scatt}} = 0 \tag{5.3}$$

$$\frac{\partial}{\partial t} E(t)\Big|_{\text{inc}} = \sum_{\mathbf{k}} \varepsilon(k) \frac{\partial}{\partial t} f(\mathbf{k},t)\Big|_{\text{scatt}} \neq 0 \tag{5.4}$$

the approximation (5.2) for the incoherent processes preserves the number density in each band but changes the kinetic energy in qualitatively the same way as the microscopic Coulomb scattering and thermalization processes would.

In addition to these scattering mechanisms there is a fast relaxation of hole spins.[49] This is due to the mixing of valence band states, i.e., hole states with different momenta $\mathbf{k}$ are different superpositions of angular momentum eigenstates so that intraband hole scattering processes lead to equal carrier distributions for the two hole bands. This relaxation process is also approximated by using a rate τ_{hole}. In the following numerical evaluation these rates will always be taken as $\tau_{\text{hole}} = \tau_{\text{scatt}} = 5\,\text{ps}$, $\tau_{\text{therm}} = 30\,\text{ps}$, and the effective lattice temperature $T_{\text{scatt}} = 80\,\text{K}$.

5.3. Microlaser-Emission Dynamics

Here we present numerical results for the laser emission after excitation with circularly polarized picosecond optical pulses. Both excitation and emission are in the z direction, as shown schematically in figure 5.1. Theoretically it is possible to study a spin polarization of the electron bands

$$P_{\text{spin}} \equiv \frac{n_{\uparrow} - n_{\downarrow}}{n_{\uparrow} + n_{\downarrow}} \tag{5.5}$$

which is exactly one by including only the light-hole to electron transition and assuming excitation by σ_+ light. The experimentally feasible spin polarization, however, is limited by the excitation process in the specific experiment. For the experiments discussed below a spin polarization of $P_{\text{spin}} = 0.5$ was reached. This is modelled by adjusting the Rabi energy of the $j = -\frac{3}{2} \rightarrow s = \downarrow$ transition for the excitation process so that $P_{\text{spin}} = 0.5$ is obtained.

Figure 5.2 shows the results for excitation of a microcavity with a 2 ps Gaussian pulse where the excitation energy is $\hbar\omega_{\text{exc}} = 20E_{\text{B}}$ above the band gap. This creates a carrier density $n_{\uparrow} = 1.3 \times 10^{12}\,\text{cm}^{-2}$ in a magnetic field of $B = 2\,\text{T}$. Even though the carrier density is excited almost instantaneously (on the 10ps time scale shown in figure 5.2) laser action does not set until 70 ps. This delay is explained by the cooling dynamics of carriers in the quantum well: The initial excitation creates carrier distributions with high kinetic energies. For lasing to occur these carrier distributions must show inversion, i.e., $f_{\text{e}}(k) - f_{\text{h}}(k) - 1 > 0$ must hold for interband energies $E_{\text{g}} + \varepsilon_{\text{e}}(k) + \varepsilon_{\text{h}}(k)$ in the vicinity of the cavity resonance. The carrier scattering and energy dissipation process, i.e., the interaction with other carriers and the lattice, is responsible for populating carrier states with small k and the delayed onset of lasing action after short pulse excitation. For a theoretical discussion using a fully microscopic approach to scattering mechanisms and comparison to experiments, see references 53, 54.

When stimulated emission sets in the total laser intensity in figure 5.2(a) begins with σ_- polarization, as shown in figure 5.2(b), because the σ_- transition

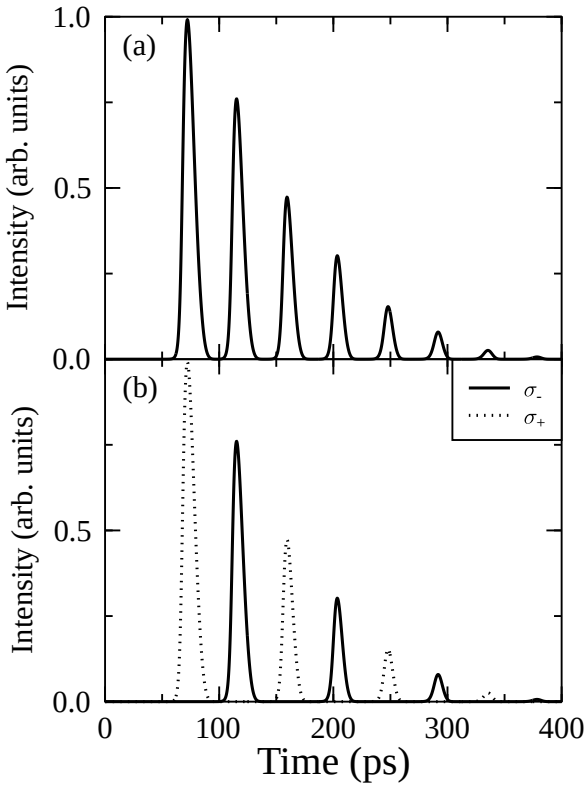

Figure 5.2.: Computed laser emission: (a) Total emission, (b) σ_+ and σ_- components.

first experiences gain. Then the total laser emission oscillates with twice the frequency of the σ_+ and σ_- polarized intensity components and its polarization alternates between subsequent emitted pulses as is apparent from figure 5.2(b). The "clock" of the oscillatory dynamics in figure 5.2(a) is set by the electrons' Larmor frequency whereas the shape of the emitted pulses is determined by the resonator quality and carrier thermalization. This macroscopic pulse emission is a consequence of the fact that stimulated emission with a definite light polarization sets in *whenever inversion for the corresponding electron-hole transition is reached*. Since the electron distributions oscillate with the Larmor frequency between the $s = \uparrow$ and $s = \downarrow$ bands the inversion is directly controlled by the magnetic field and carrier scattering processes.

Thus the magnetic field "switches" between σ_+ and σ_- polarizations of the light by its coupling to the electron spin which is of a purely quantum-mechanical nature. The modulation of the macroscopic laser emission can therefore be regarded as the macroscopic manifestation of microscopic quantum-mechanical dynamics.

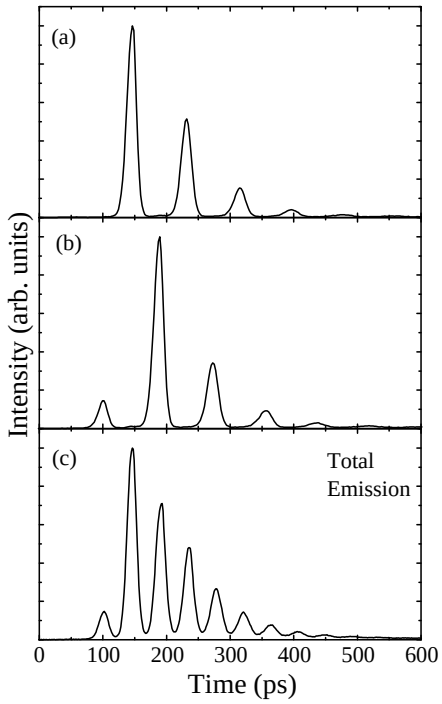

Figure 5.3.: Experimental emitted laser intensity after short pulse excitation in a 2 Tesla magnetic field (from reference 56): (a) σ^+-polarized and (b) σ^--polarized emission; (c) total emission.

The light emission of a microlaser in a transverse magnetic field was studied experimentally[13,57] using a semiconductor microcavity laser consisting of a $\frac{3}{2}\lambda$ cavity with two 8 nm $In_{0.04}Ga_{0.96}As$ quantum wells separated by GaAs barriers. The wells were placed in the antinodes of the intracavity electric field, which is formed by two GaAs/AlAs distributed Bragg reflectors with 99.6% reflectivities. This reflectivity is maintained over a whole frequency range around the emission wavelength which acts as a stop band for light. This makes excitation of the quantum-wells inside the cavity along the z direction only possible with frequencies outside of the stop-band high-reflection region. Here, the pump wavelength was *above the microcavity stop-band*, so that in addition to the quantum wells the barriers inside the cavity and the DBR layers were excited. Excitation was performed with circularly polarized pulses of a Ti:Sapphire laser with 2 ps pulse length, 80 MHz repetition rate and 780 nm wavelength. The microcavity emission at 835 nm was detected in reflection geometry, analyzed with a circular polarizer, spectrally dispersed, and temporally resolved in a streak camera with a time resolution of 7 ps. Throughout the experiment, the sample was kept at a temperature of 15 K in a superconducting magnet.

The behavior described theoretically above is present in experimental results for the microlaser emission. Figure 5.3 shows the pulsed emission with alternating polarization after an initial delay of several ten picoseconds. Due to the specific experimental situation, the initial excitation leading to the laser emission is above the microcavity stop-band, and the barriers and distributed Bragg reflectors are also excited. Therefore the actual excitation conditions *in the quantum well* are difficult to determine theoretically. As a consequence, the pulse delay, which sensitively depends on the intial excitation in the quantum-well, can be different for simulation and experiment, whereas the dynamics due to the magnetic field is not influenced.

5.4. Controlling the Microlaser

In this section we analyze how the pulse emission behavior of the microlaser emission can be controlled. We first focus on larger magnetic fields. Figure 5.4 shows the emitted laser intensity for various magnetic fields up to $B = 11\,\mathrm{T}$. The carrier density excited by the 2 ps pulse is $n_{\uparrow} = 1.2 \times 10^{12}\,\mathrm{cm}^{-2}$, and the spin polarization $P_{\mathrm{spin}} = 0.5$. For lower magnetic fields (B =2 T and 4 T) the emission shows clearly resolved pulses synchronized to the electron spin dynamics. For higher magnetic fields (B =8 T and 11 T) the resolution is washed out by the intrinsic laser dynamics because the cycle lengths of about 10 ps become comparable to the time the laser needs to "switch off" emission of one polarization and "switch on" emission of the other polarization. That is, the emission of laser light with $\sigma_+(\sigma_-)$ polarization has not ceased completely when stimulated emission with $\sigma_-(\sigma_+)$ polarization sets in. This behavior is shown in the computed result because the cavity quality has been modelled according to the experiment[56] by a phenomenological cavity loss of κ =1/(2 ps). In general, for better cavity qualities shorter pulses and pulse delays are to be expected.[53]

The experimental results for the laser emission in increasing magnetic fields are shown in figure 5.5. As discussed above, the delay of the first pulse is different due to the excitation of the cladding layers. The changing modulation of the emission is observed experimentally as well as theoretically, as shown in figure 5.4. As argued theoretically above, the incomplete modulation for the high magnetic fields is a property of the specific laser design and not an intrinsic limitation for the resolution of single pulses.

Next, the influence of different excitation conditions on the emission dynamics is analyzed. In figure 5.6, the magnetic field has been kept constant at B =2T but the Rabi energy of the optical excitation is varied from $\mathscr{R} \equiv d_{\mathrm{cv}}E = 0.5E_{\mathrm{B}}$ to $\mathscr{R} = 2.5E_B$, where the excitation intensity is proportional to the Rabi energy squared.

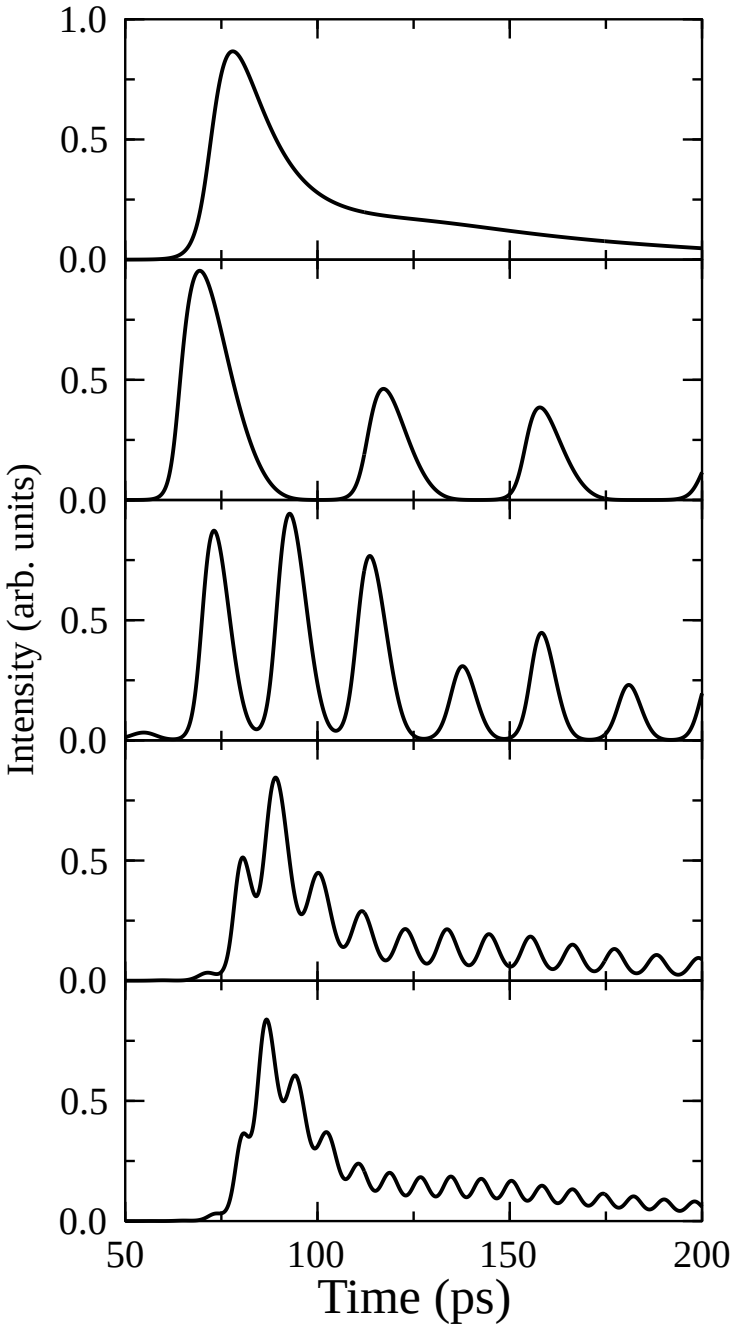

Figure 5.4.: Computed laser emission for various magnetic fields; from top to bottom: $B = 0$T, 2T, 4T, 8T, and 11T.

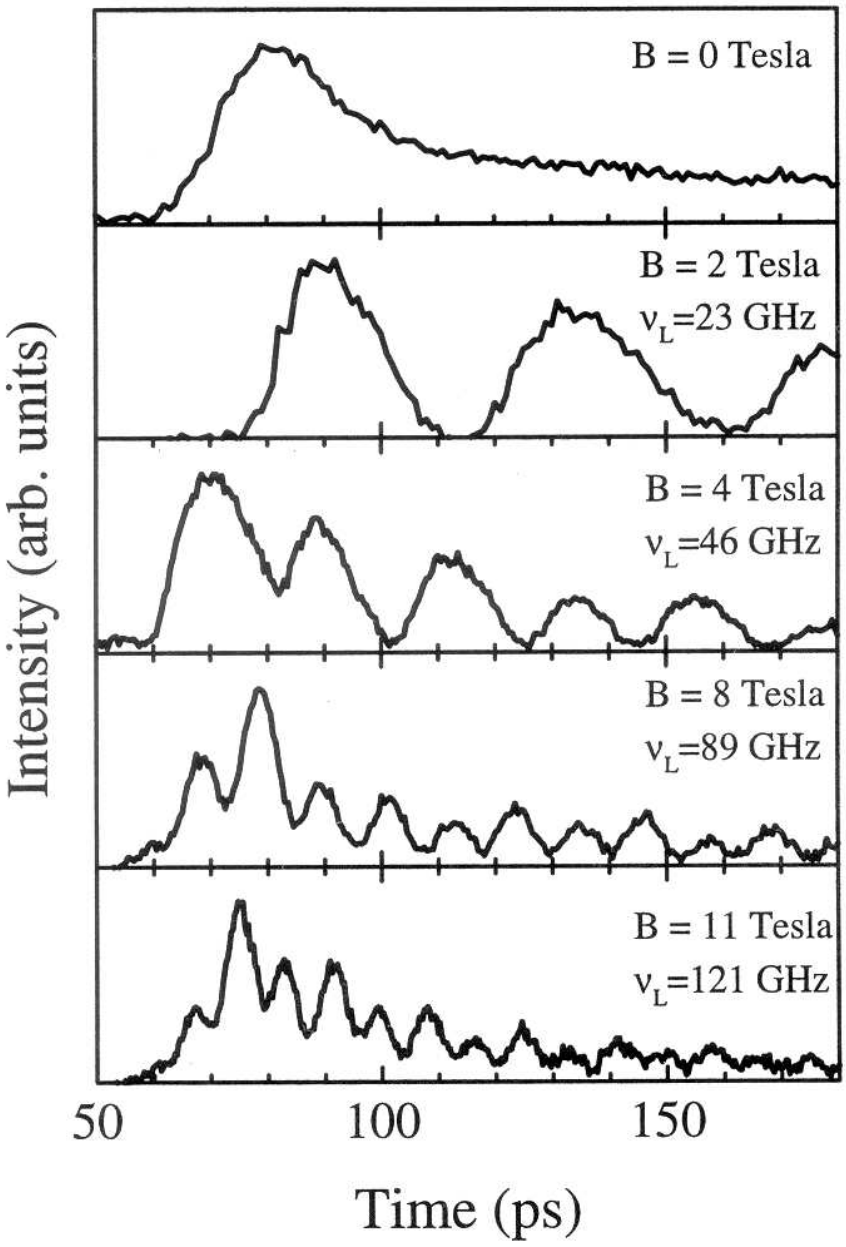

Figure 5.5.: Experimental laser emission for different magnetic fields[56] and the corresponding Larmor frequencies ν_L.

For the lowest excited carrier density the emitted intensity is luminescence without spontaneous contribution because the laser threshold is not reached. Here, the magnetic field dynamics does not show any influence because the amplification by the stimulated emission is missing. For higher excited carrier densities the stimulated emission, which is sensitive to the electrons' dynamics in the B field, becomes more pronounced. First the stimulated emission is just a weak modulation of the spontaneous background but the modulation becomes stronger as the threshold is approached. Well over the threshold, the stimulated emission exceeds the spontaneous emission by several orders of magnitude and the emitted signal shows a modulation depth of 100%. The modulation depth in the total emission depends so strongly on the excited carrier density because the oscillations arise from a switching from luminescence to lasing, and the behavior of the laser switch-on is controlled by the inversion at the cavity resonance.

Experimental results for different pump intensities and constant magnetic field are shown in figure 5.7. The emission dynamics of the microlaser above the threshold shows the same modulation behavior as the computed results, except for the above-mentioned difference of the laser onset. Below the threshold, however, one has a continuous rise of the measured intensity over a few hundred picoseconds, in contrast to the falling-off of the computed curve in figure 5.6. This is due to the fact that in the present theory spontaneous emission is only included in the simplified treatment according to Fermi's Golden Rule which is a good approximation only for a carrier plasma at high densities. The luminescence properties at low and intermediate densities require a quantum treatment of the electromagnetic field and the inclusion of Coulomb correlations leading to the semiconductor-luminescence equations.[48] There it is shown that the important quantity determining the emission in the spectral vicinity of the exciton resonance is the overlap of the carrier distributions with the excitonic wave functions. The experimental data presented here were taken from a sample which shows strong normal-mode coupling which makes matters even more complicated. A discussion of these points can be found in reference 58, where the luminescence properties of the same sample are analyzed. A detailed analysis of these effects in connection with the magnetic field dynamics is beyond the scope of our present theory, which has therefore only limited validity in the low-density regime.

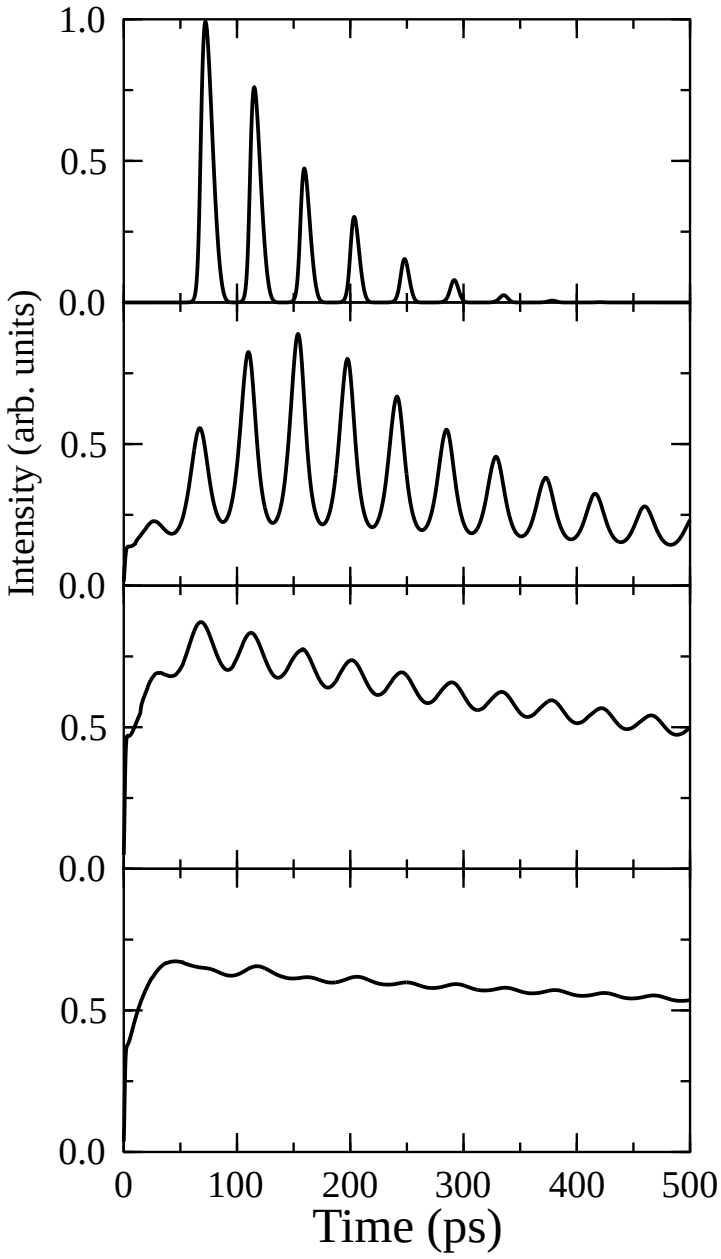

Figure 5.6.: Computed light emission for various pulse excitation energies at a magnetic field of 2 Tesla. From bottom to top the Rabi energies for the pulse excitation are $\mathscr{R} \equiv d_{\mathrm{cv}}E = 0.5E_{\mathrm{B}}$, $1.0E_{\mathrm{B}}$, $1.5E_{\mathrm{B}}$ and $2.5E_{\mathrm{B}}$. Laser emission is only present in the two upper figures; the lower curves correspond to excitation below the laser threshold.

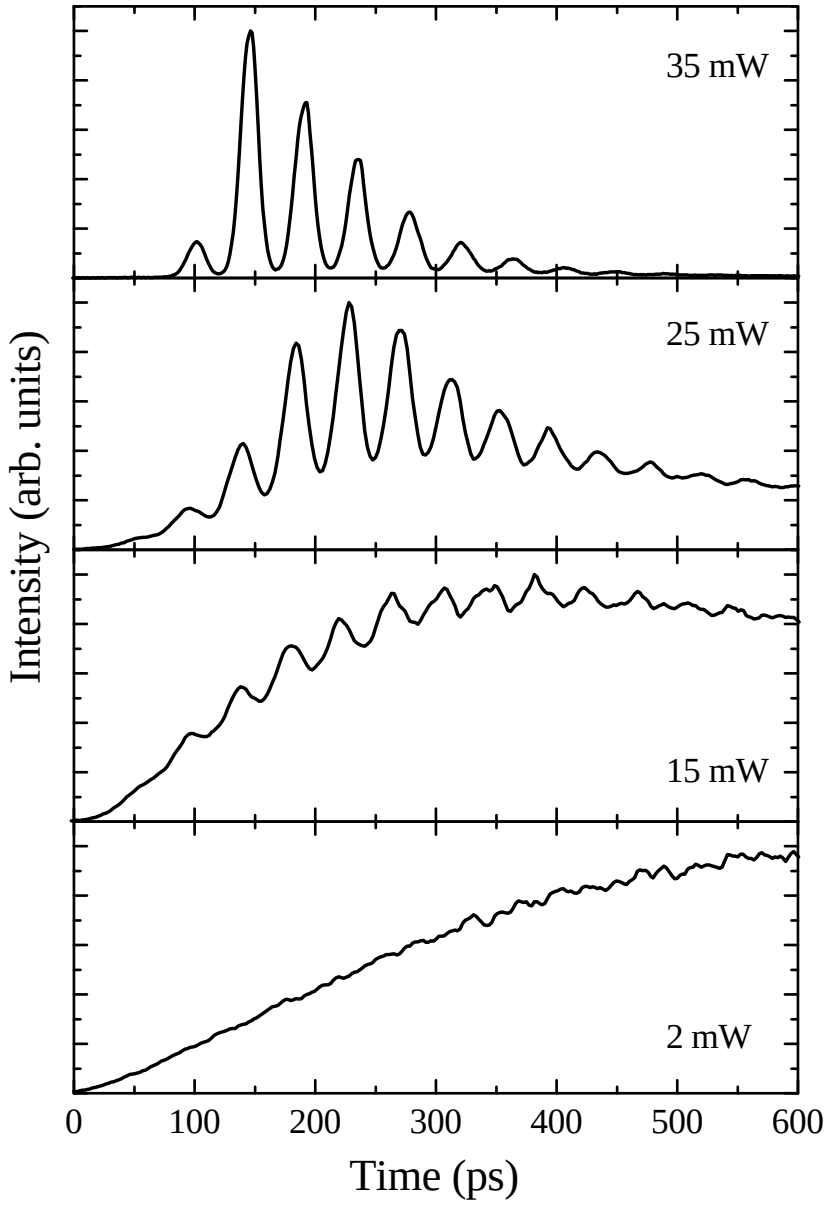

Figure 5.7.: Experimental light emission[56] for increasing excitation intensities at a magnetic field of 2 Tesla. The two lower curves show luminescence below the lasing threshold.

6. Conclusions and Outlook

In this thesis, the dynamics of coherences introduced in semiconducting materials by external fields is analyzed theoretically. We have presented a solution to the polariton propagation in bulk semiconductors in the first part of this work and discussed the spin dynamics in transverse magnetic fields in the second part.

The microscopic theory of polariton propagation presented here constitutes the first full solution of the polariton problem with spatial dispersion in media with surfaces since the introduction of the problem over forty years ago. Our theory takes the multi-band structures of realistic materials into account and its only phenomenological parameter is a polarization dephasing time. The results are in quantitative agreement with precision measurements on very high-quality GaAs material.

The solution of the polariton problem presented here is very involved and makes use of present-day supercomputers. Because of this complexity, many approximate approaches have been developed over the past forty years. It has long been noted that these approximations yield contradicting results, and the debate over their foundations has been renewed only recently with the introduction of a new analysis of the problem.[9] With our full solution we have been able to investigate approximations to the polariton problem in detail: Numerical results obtained from various approximations have been compared to the full calculation. While for the intermediate sample lengths considered here the macroscopic approximations did not yield satisfactory agreement, Pekar's original additional boundary condition[8] consistently led to better results than other approximations.

The microscopic solution of the polariton problem as developed in chapter 2 has other interesting applications. First, within the present approach the calculation of quantum-well transmission spectra is possible which include the full sub-band structure with confinement energies and excitonic binding energies. This is an improvement over conventional theoretical treatments using an expansion in subband eigenfunctions which can only determine the change of binding energies.[22] Second, the application of our results to resonant tunneling[11] is also directly possible since the theoretical description of tunneling processes is very similar to the one in chapter 2.

The second part of the thesis deals with the theoretical description of the

electron-electron coherence induced in semiconductors by transverse magnetic fields. The equations governing the electronic dynamics are formally very similar to those governing the electron-hole dynamics induced by optical fields. This similarity has been discussed and a simplified version of the theory has been applied to the direct determination of the electronic Landé factor in arbitrary semiconductor structures in a novel geometry.[12] Here, we have used the semiconductor Bloch-equations to determine the excitation conditions of a quantum-well by including the dipole matrix elements of the electron-hole transitions involved. We then have calculated the dynamics of the spin polarization which, for different Landeé factor signs, results in different phases of the luminescence which is experimentally directly visible.

An application to the emission of a microlaser in a transverse magnetic field after short pulse excitation has been made by combining the microscopic theory for the electronic coherence with a semiclassical microlaser theory. Here, we were able to explain the modulation of laser emission in magnetic fields and show that it constitutes a macroscopic manifestation of the microscopic electronic spin dynamics. We have examined ways to control the laser modulation, i.e., how to make shorter laser pulses, and compared our results to experiments which prove the technical feasibility of controlling the microlaser emission using magnetic fields.

Since the dynamics of the electronic coherence for which the theory was presented here, is "visualized" with the help of the laser, the inclusion of the carrier interaction with the light field and with other carriers is also important for a consistent description. The carrier-carrier interaction has been treated approximately in this microlaser model to demonstrate the possibility of modulating the laser emission. For higher magnetic fields, i.e., shorter emitted pulses, or for experiments probing the magnetic field dynamics on timescales comparable to the scattering times this simplified treatment should be replaced by a microscopic description.[51,53]

A. Luttinger Hamiltonian

For the description of the hole-band structure we have employed a phenomenological approach due to Luttinger and Kohn[59,60] which is widely used in semiconductor physics.[5,29,61] Instead of presenting a derivation using $\mathbf{k}\cdot\mathbf{p}$ theory we will introduce the Hamiltonian directly using symmetry considerations because this is the important aspect here.

The information needed to construct the Hamiltonian is that the hole-band states at the zone center ($\mathbf{k}=0$) are made up from atomic p orbitals. Because of the spin-orbit interaction, therefore, the zone center basis-states are eigenstates of the total angular momentum, i.e., their quantum numbers are $J=\frac{3}{2}$ and $j=\pm\frac{3}{2}, \pm\frac{1}{2}$, or $J=\frac{1}{2}$ and $j=\pm\frac{1}{2}$. Since the states belonging to $J=\frac{1}{2}$ are energetically shifted to lower energies the hole states in the vicinity of the fundamental absorption edge are the $J=\frac{3}{2}$ states.

We will consider here the Luttinger Hamiltonian only in its *spherically symmetric form* which can be obtained from the most general expression using the crystal momentum $\mathbf{k}$ and the total angular momentum operator

$$\mathscr{H}(\mathbf{k}) = \frac{\hbar^2}{2m_0}\left[\left(\gamma_1+\frac{5}{2}\gamma_2\right)k^2 - 2\gamma_2(\mathbf{k}\cdot\widehat{\mathbf{J}})\right] \tag{A.1}$$

which is invariant under rotations. This invariance is guaranteed because $\mathbf{k}$ is a vector and $\widehat{\mathbf{J}}$ is a vector operator. We have written equation (A.1) using the phenomenological parameters γ_1, γ_2, and γ_3 introduced originally by Luttinger ($\gamma_2=\gamma_3$, in our case). Already from equation (A.1) it is apparent that $\mathscr{H}(\mathbf{k})$ is rotationally invariant only under symmetry transformations involving both $\mathbf{k}$ and $\widehat{\mathbf{J}}$. Therefore, even the so-called spherically symmetric Luttinger Hamiltonian must have eigenenergies $\varepsilon(\mathbf{k})$, which generally do not depend on the modulus k alone, that is, the energy dispersions do not show a rotational symmmetry in $\mathbf{k}$ space.

Evaluating equation (A.1) for the basis states $\{|j\rangle\}$, which are labeled by their angular momentum projection quantum number in z direction $j=\frac{3}{2},-|\frac{1}{2},\frac{1}{2},-\frac{3}{2}$,

one obtains the 4×4 Luttinger matrix

$$\mathscr{H}(\mathbf{k}) = \begin{pmatrix} P+Q & R & -S & 0 \\ R^* & P-Q & 0 & R \\ -S^* & 0 & P-Q & S \\ 0 & S^* & R^* & P+Q \end{pmatrix} \tag{A.2}$$

with*

$$P(k_\perp, k_z) = \frac{\hbar^2}{2m_0}\gamma_1(k_\perp^2 + k_z^2) \ , \tag{A.3}$$

$$Q(k_\perp, k_z) = \frac{\hbar^2}{2m_0}\gamma_2(k_\perp^2 - 2k_z^2) \ , \tag{A.4}$$

$$R(\mathbf{k}_\perp) = -\frac{\hbar^2}{2m_0}\sqrt{3}\gamma_2(k_x^2 - k_y^2 - 2ik_xk_y)^2 = \frac{\hbar^2}{2m_0}\sqrt{3}\gamma_2 k_\perp^2 e^{-2i\phi_\perp} \ , \tag{A.5}$$

$$S(\mathbf{k}_\perp, k_z) = \frac{\hbar^2}{2m_0}2\sqrt{3}\gamma_3 k_z(k_x - ik_y) = \frac{\hbar^2}{2m_0}2\sqrt{3}\gamma_3 k_z k_\perp e^{-i\phi_\perp} \ . \tag{A.6}$$

Note that the diagonal matrix elements only depend on the modulus of k_z and $k_\perp \equiv |\mathbf{k}_\perp|$, whereas the off-diagonal elements also depend on the angle $\phi_\perp \equiv \tan^{-1}(k_y/k_x)$ of the in-plane vector $\mathbf{k}_\perp$. The energy dispersion of the Hamiltonian (A.2) describes two doubly degenerate hole bands, which are commonly designated as "light" and "heavy holes". Including elastic strain in the Hamiltonian matrix (A.2) leads to an energy shift ΔE in the diagonal elements of the Luttinger matrix,[61] which has the same magnitude but a different sign for the $P+Q$ and $P-Q$ terms.

We will extract the important symmetry information directly by expanding $\mathscr{H}$ with respect to the functions $e^{-im\phi_\perp}$, that is,

$$\mathscr{H}^{(m)}(k_\perp, k_z) = \frac{1}{2\pi}\int_0^{2\pi} d\phi_\perp \, e^{im\phi_\perp}\mathscr{H}(\mathbf{k}_\perp, k_z) \ . \tag{A.7}$$

Because of the phase factors only the diagonal terms, equation (A.3) and (A.4) are proportional to $\delta_{m,0}$. The off-diagonal terms, on the other hand, equation (A.6) and (A.5) are proportional to $\delta_{m,\pm 2}$ and $\delta_{m,\pm 1}$, respectively. The contributions to $\mathscr{H}^{(0)}$ are only from diagonal elements of the Hamiltonian (A.2). This important result is used in chapter 2 and we will be only concerned with these $m = 0$ contri-

*In the spherical approximation to the original Luttinger approach, γ_2 in the matrix element R is replaced by $\gamma_{23} \equiv (\gamma_2 + \gamma_3)/2$.

butions. Defining

$$\varepsilon_{\mathrm{HH}}(k_\perp, k_z) \equiv \frac{\hbar^2}{2m_{\mathrm{HH}\perp}} k_\perp^2 + \frac{\hbar^2}{2m_{\mathrm{HHz}}} k_z^2 \tag{A.8}$$

$$\varepsilon_{\mathrm{LH}}(k_\perp, k_z) \equiv \frac{\hbar^2}{2m_{\mathrm{LH}\perp}} k_\perp^2 + \frac{\hbar^2}{2m_{\mathrm{LHz}}} k_z^2 \tag{A.9}$$

we obtain for the $m = 0$ component of equation (A.7)

$$\mathscr{H}^{(0)}(k_\perp, k_z) = \begin{pmatrix} \varepsilon_{\mathrm{HH}} - \Delta E & 0 & 0 & 0 \\ 0 & \varepsilon_{\mathrm{LH}} + \Delta E & 0 & 0 \\ 0 & 0 & \varepsilon_{\mathrm{LH}} + \Delta E & 0 \\ 0 & 0 & 0 & \varepsilon_{\mathrm{HH}} - \Delta E \end{pmatrix} \tag{A.10}$$

with the anisotropic light hole and heavy hole masses given by the Luttinger parameters

$$m_{\mathrm{LHz}} = \frac{m_0}{\gamma_1 + 2\gamma_{23}}\,, \qquad m_{\mathrm{HHz}} = \frac{m_0}{\gamma_1 - 2\gamma_{23}}\,, \tag{A.11}$$

$$m_{\mathrm{LH}\perp} = \frac{m_0}{\gamma_1 - \gamma_{23}}\,, \qquad m_{\mathrm{HH}\perp} = \frac{m_0}{\gamma_1 + \gamma_{23}}\,. \tag{A.12}$$

B. Numerical Techniques

In this Appendix we outline the numerical treatment of the coupled equations (2.31), (2.37), (2.38) and (2.32). We first transform the dynamical quantities in order to eliminate the explicit occurence of the gap energy in equation (2.31) because the numerically large value necessitates very small timesteps. Therefore we define, e.g.,

$$\widetilde{\Psi}(t) = e^{-i\omega_0 t}\Psi(t), \tag{B.1}$$

$$\widetilde{E}(z,t) = e^{-i\omega_0 t}E(z,t). \tag{B.2}$$

Here we have specialized ω_0 to be the gap frequency, $\hbar\omega_0 \equiv E_G$. Since this transformation affects all dynamical variables, i.e., polarizations electromagnetic fields, and currents, we will omit the tilde in the following.

B.1. Schrödinger Equation

To focus on the discretization in the time domain we suppress space and momentum variables and rewrite the Schrödinger type equation (2.31) symbolically as

$$i\hbar\frac{\partial}{\partial t}\Psi(t) = \widehat{H}\Psi(t) + \hbar\Omega(t) \tag{B.3}$$

where $\hbar\Omega(t)$ is a genereralized external driving term and $\widehat{H}$ includes both the kinetic Hamiltonian and the Coulomb interaction. For the numerical integration of equation (B.3) we have used the explicit second-order differencing scheme[11,62]

$$\Psi(t+\Delta t) \approx \Psi(t-\Delta t) - i(2\Delta t)\left[\frac{1}{\hbar}\widehat{H}\Psi(t) + \Omega(t)\right]. \tag{B.4}$$

This differencing scheme has two advantages. First, it is explicit, i.e., the "new" $\Psi(t+\Delta t)$ can be computed directly from values at earlier times without solving a system of linear equations. Second, it respects the time-reversal symmetry of the Schrödinger equation and therefore conserves the energy and the norm of the

complex wavefunction.[62] Also, if the chosen time step exceeds the stability limit for equation (B.4), exponential solutions become dominant and lead to divergent results which allows the empirical determination of the stability limit.

The amplitude Ψ in equation (B.4) depends on two space and one momentum variables. The space dependence is discretized using a two-dimensional equidistant grid (z_α, z_β) with spacing Δz_Ψ. For the momentum space variable $k \equiv k_\perp$ a Gaussian quadrature with grid points k_κ indexed by κ are used. This leads to the discretized quantity

$$\Psi^n_\kappa(\alpha,\beta) = \Psi(k_\kappa, z_\alpha, z_\beta, t_n). \tag{B.5}$$

The singularity of the Coulomb potential is removed numerically[5] and we typically use 90 $k_\perp$ Gaussian quadrature points which are accumulated below $k_\perp = 4a_B^{-1}$. Choosing the spacing of $\Delta z_\Psi = 0.1 a_B$ we reach the stability limit of the scheme (B.4) at $\Delta t \simeq 2.0$ fs. We used for our computations $\Delta t = 1.5$fs. Choosing a smaller time step $\Delta t = 1.0$fs for test purposes led to the same results.

Writing $\Psi^n(\alpha,\beta)$ in the following always refers to the whole "vector" formed by the $\Psi^n_\kappa(\alpha,\beta)$. Derivatives are approximated on the space grid by using a second order scheme,[63] i.e., the terms in equation (2.31) containing derivatives become

$$\begin{aligned}\left[\frac{1}{m_{\mathrm{ez}}}\frac{\partial^2}{\partial z_{\mathrm{e}}^2} + \frac{1}{m_{\mathrm{hz}}}\frac{\partial^2}{\partial z_{\mathrm{h}}^2}\right]\Psi(z_{\mathrm{e}}, z_{\mathrm{h}}, t) \approx \\ \frac{1}{m_{\mathrm{ez}}}\frac{\Psi^n(\alpha+1,\beta) - 2\Psi^n(\alpha,\beta) + \Psi^n(\alpha-1,\beta)}{(\Delta z)^2} \\ + \frac{1}{m_{\mathrm{hz}}}\frac{\Psi^n(\alpha,\beta+1) - 2\Psi^n(\alpha,\beta) + \Psi^n(\alpha,\beta-1)}{(\Delta z)^2}.\end{aligned} \tag{B.6}$$

Consequently, for the computation of $\Psi^{n+1}(\alpha,\beta)$ at time $t_{n+1} = t_n + \Delta t$ we need only $\Psi^n(\alpha,\beta)$ together with the four neighboring values $\Psi^n(\alpha+1,\beta)$, $\Psi^n(\alpha-1,\beta)$, $\Psi^n(\alpha,\beta+1)$, and $\Psi^n(\alpha,\beta-1)$. Note also that the Coulomb matrix element in equation (2.31) only couples $\Psi^n_\kappa(\alpha,\beta)$ values with the same spatial (α,β) but different momentum (κ) indices. For numerical purposes, therefore, this index dependence makes it effective to regard $\Psi^n(\alpha,\beta)$ as defined on a two-dimensional space grid where (α,β) numbers the grid points. Each grid point is now a vector with the discrete momentum index κ.

Grouping the grid points into square cells in a checkerboard pattern leads to a two dimensional mesh of cells such that every grid point belongs to only one cell, as shown in figure B.1. The numerical computation is very well suited for parallel computers if each of these cells is assigned to one processor. Since a space grid point needs only its four neighboring points, the calculation of the RHS of (B.4) using (B.6) for a time step can be carried out directly for all *inner* points, i.e., for

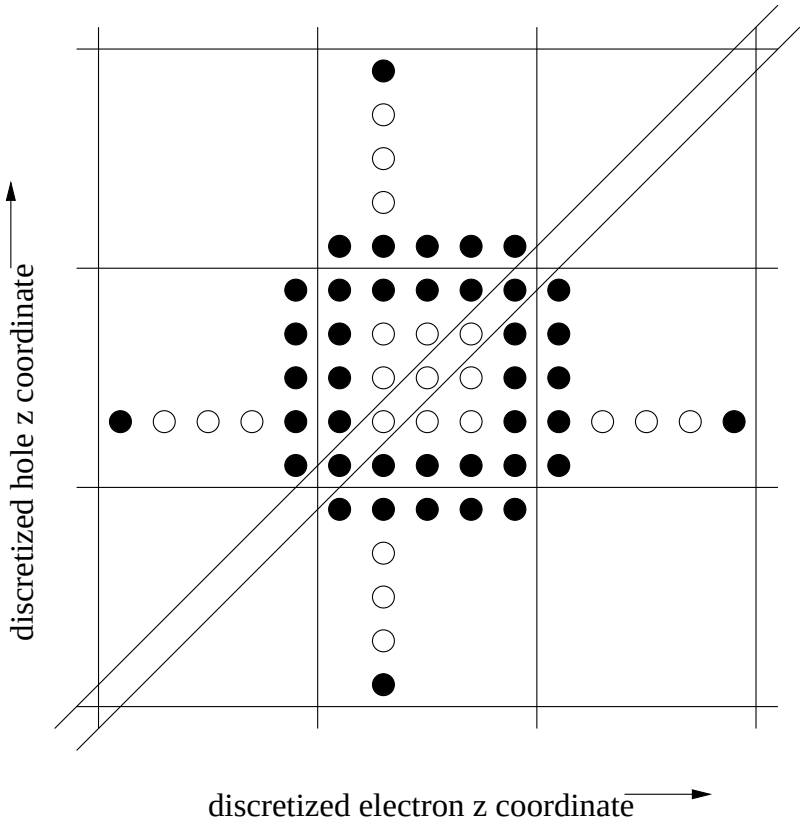

Figure B.1.: Partioning of z grid points on the two-dimensional processor topology, shown for the case of $3 \times 3 = 9$ processors. Each square represents a processor and each dot a grid point with coordinate (α, β). Inner points are drawn as open, boundary points as solid circles. The diagonal points $z_e = z_h$ have also been marked; they are used for the computation of the polarization, cf. equation (2.39).

points whose four neighbors belong to the same cell. The points that require the values of $\Psi^n(\alpha, \beta)$ from *another cell* for the computation of $\Psi^{n+1}(\alpha, \beta)$ are lined up along the square-shaped boundaries of each cell because the discretization (B.6) makes only use of α and β values incremented or decremented by 1. Therefore each processor must receive the values of the adjacent boundary points from the four neighboring cells before equation (B.4) can be computed for the boundary points of its own cell. This data exchange between all processors must occur in each time step.

The grid structure outlined above can be implemented using the message passing interface (MPI).[64,65] Technically, nonblocking send and receive commands handle the data exchange necessary for the boundary points *while* the $\Psi^{n+1}(\alpha, \beta)$ values are computed for all inner points. When the data exchange is complete, $\Psi^{n+1}(\alpha, \beta)$ is computed for the boundary points of each cell.

B.2. Electromagnetic field

When treating the time evolution of the electromagnetic field one faces the problem that the space grid encompasses the sample and a finite space outside the sample where the electromagnetic field is produced and detected. Now, the time development must be computed for several picoseconds to monitor the radiation from the slowly decaying polarization in the slab. Therefore, the initial pulse has long reached the end of the computational domain before the computation has finished and the spectrum can be computed. Thus multiple reflections occur at the ends of the space grid if one discretizes Maxwell's equation straightforwardly and chooses a boundary condition for the computational domain because any boundary condition will lead to at least partial reflection. This difficulty is avoided by discretizing the equations for the electomagnetic field (2.37) and (2.38) on a one-dimensional grid using Hartree's method. Since this method is described comprehensively in reference 63 (Sec. 4-15), we omit a detailed discussion and only quote the results here: The characteristic curves for Maxwell's equations are straight lines, $\Delta z = c\Delta t$, and the partial differential equations (2.37) and (2.38) reduce to ordinary differential equations along these lines. These are used to derive the discretized versions of the transformed equations (2.37) and (2.38)

$$\begin{aligned} E_j^{n+1} =& \frac{1}{2n_{\mathrm{bg}}}\eta(B_{j-1}^n - B_{j+1}^n) + \frac{1}{2}\eta(E_{j-1}^n + E_{j+1}^n) \\ &+ \frac{\Delta t}{4n_{\mathrm{bg}}\xi}(2J_j^{n+1} + J_{j-1}^n + J_{j+1}^n), \end{aligned} \tag{B.7}$$

$$\begin{aligned} B_j^{n+1} =& \frac{1}{2n_{\mathrm{bg}}}\eta(B_{j-1}^n + B_{j+1}^n) + \frac{1}{2}\eta(E_{j-1}^n - E_{j+1}^n) \\ &+ \frac{\Delta t}{4n_{\mathrm{bg}}\xi}(J_{j-1}^n - J_{j+1}^n). \end{aligned} \tag{B.8}$$

Here, we have discretized $E_j^n \equiv E(z_j, t_n)$, $B_j^n \equiv B(z_j, t_n)$, $J_j^n \equiv J(z_j, t_n) + \frac{\partial}{\partial t}P(z_j, t_n)/\varepsilon_0$. Also, we have defined $\xi = 1 - i\omega_0\Delta t/2$ and $\eta \equiv \xi^*/\xi$. These additional factors are due to the transformation (B.2), the discretized versions of the original equations (2.37) and (2.38) are obtained by letting $\omega_0 = 0$.

The space grid for equations (B.7) and (B.8), Δz_E, is chosen such that $\Delta z_E = c\Delta t$ holds after Δt is determined according to the stability limit of equation (B.4). Typically, we obtain Δz_E on the order of one Bohr radius. This method is capable of handling semiconductor heterostructures of arbitrary composition via the z dependent background refractive index $n(z)$. Since we are only interested in polaritonic effects due to the excitonic polarization, we use the constant GaAs value for the refractive index $n(z) \equiv n_{\mathrm{bg}} = 3.71$ in equations (B.7) and (B.8).

C. The Microlaser

C.1. Introduction

Microcavity lasers, as shown schematically in Fig. 5.1, are fabricated using layers of semiconductor material with alternating refractive indices. The cavity lengths are very small, typically only a few microns, and the active material is formed by one or several quantum wells in the cavity. Light emission occurs through the surfaces parallel to the quantum wells. Because the quantum wells are thin in comparison to the gain region of conventional semiconductor lasers, mirrors with very high reflectivities are needed in order to achieve laser action. These are provided by the distributed Bragg reflectors which reach reflectivities of more than 99.9% in a spectral region ("stop band") around the cavity resonance.

The physics of these lasers which makes them a well-defined test case for basic investigations of the light-matter interaction and an important tool for optical switches and fiber communications is reviewed extensively in Ref. 19 and will not be discussed here. We only need the fact that the resonator length is chosen so that there is a single resonator mode in the spectral region where optical gain occurs. Therefore in our semiclassical treatment, which uses the laser mainly as a tool to investigate the spin dynamics, we will not compute gain and intensity spectra but work with optical gain and intensities evaluated at the cavity resonance ω_{cav}.

C.2. Model of the Microlaser

The computations below are exactly the same for both the σ_+ and σ_- subsystems shown in Fig. 4.1 and are formulated using the electromagnetic fields in the cavity for σ_+ and σ_- polarization, together with the carrier distribution functions corresponding to the transitions. For notational simplicity we will therefore omit the $\pm$ for the electromagnetic quantities like intensities and susceptibilities and denote the carrier distributions belonging to the electromagnetic transition simply by "e" and "h".

C.2.1. Electromagnetic Field in the Cavity

We start by combining equations (2.37) and (2.38) to the one-dimensional wave equation

$$-\nabla^2 E + \frac{n^2}{c_0^2}\frac{\partial^2}{\partial t^2}E = -\frac{1}{\varepsilon_0 c_0^2}\frac{\partial^2}{\partial t^2}P \tag{C.1}$$

which describes the electromagnetic field with the polarization as source term. We now express the time and space dependence of the electromagnetic field in the microresonator

$$E(\mathbf{r},t) = \mathscr{E}(t)e^{-i\omega_{\mathrm{cav}}t}u(\mathbf{r}) + \text{complex conjugate} \tag{C.2}$$

using the complex coefficients $\mathscr{E}$ and the mode function $u(\mathbf{r})$ for the microresonator. The mode functions $u(\mathbf{r})$ satisfy

$$\nabla^2 u(\mathbf{r}) + \left(\frac{n_{\mathrm{bg}}^2\omega_{\mathrm{cav}}}{c_0}\right)^2 u(\mathbf{r}) = 0 \tag{C.3}$$

with the appropriate boundary condition which is, in principle, determined by the cavity design.

In the following we keep only the positive frequency parts

$$E(z,t) \simeq \mathscr{E}(t)e^{-i\omega_{\mathrm{cav}}t}u(\mathbf{r}), \tag{C.4}$$

that is we will always work in the rotating-wave approximation (RWA) which neglects terms rotating with twice the relevant cavity frequency. Using equations (C.4) and (C.3) in the wave equation (C.1) we perform the slowly-varying envelope approximation[32] which amounts to neglecting the second order spatial and time derivatives. Then equation (C.1) becomes a simple first order differential equation which relates the time evolution of the complex electric field to the polarization

$$\frac{\partial}{\partial t}\mathscr{E}(t) = -2i\,\frac{\omega_{\mathrm{cav}}}{n_{\mathrm{bg}}^2\varepsilon_0}\mathscr{P}(t). \tag{C.5}$$

Here we have used P in the form analogous to (C.4)

$$P(\mathbf{r},t) \simeq \mathscr{P}(t)e^{-i\omega_{\mathrm{cav}}t}u(\mathbf{r})\ . \tag{C.6}$$

Assuming that the space dependence of the quantum-well polarization $P(\mathbf{r},t)$ is described by an independent function $f(\mathbf{r})$ we obtain

$$\mathscr{P}(t) = \Gamma\frac{1}{\mathscr{A}}\sum_{\mathbf{k}} d_{\mathrm{cv}}^{*}\Psi(\mathbf{k},t) \tag{C.7}$$

where the overlap between mode function and quantum-well is defined by

$$\Gamma = \int d^3r\, f(\mathbf{r}) u^*(\mathbf{r}). \tag{C.8}$$

It is taken to be $\Gamma = 0.6$ in all numerical computations. Defining the susceptiblity

$$\chi(t) \equiv \frac{\mathscr{P}(t)}{\mathscr{E}(t)}\,, \tag{C.9}$$

equation (C.5) yields an equation for the laser intensity $I(t) \equiv |\mathscr{E}(t)|^2$ by differentiating the product $\mathscr{E}(t)\mathscr{E}^*(t)$

$$\frac{\partial}{\partial t} I(t)\bigg|_{\text{stim}} = g_{\text{cav}}(t) I(t) - \frac{\omega_{\text{cav}}}{2Q} I(t) \tag{C.10}$$

with the gain at the cavity resonance

$$g_{\text{cav}}(t) \equiv -2\Gamma \frac{\omega_{\text{cav}}}{n_{\text{bg}}^2} \,\text{Im}\chi(t) \tag{C.11}$$

and a phenomenological decay term $\kappa \equiv \omega_{\text{cav}}/(2Q)$ which models losses due to the cavity quality Q. For the numerical evaluation we have used $\hbar\omega_{\text{cav}} = 1E_{\text{B}}$ and $\kappa = 1/(2\text{ps})$.

C.2.2. Polarization of the Active Medium

Since the polarization dephasing used in equation (C.9) occurs on a very short timescale due to polarization and carrier scattering it is given by its value in a quasi-equilibrium state which is determined by the carrier distributions and electromagnetic field.[5] To obtain the quasi-equilibrium susceptibility one regards the dependence of equation (4.18) on the distribution functions $f_{\text{e}}(k) \equiv f_{\text{e}}(k,t)$, $f_{\text{h}}(k) \equiv f_{\text{h}}(k,t)$ and $\mathscr{E} \equiv \mathscr{E}(t)$ as parametric and perfoms a Fourier transformation for time dependence of the polarization. The result is a self-consistency equation for $\widetilde{\chi}(k,\omega) = \Psi(k,\omega)/\mathscr{E}$

$$\widetilde{\chi}(k,\omega) = -\frac{1 - f_{\text{e}}(k) - f_{\text{h}}(k)}{\hbar\omega - \varepsilon_{\text{eh}}(k) + i\gamma} \left[d_{\text{cv}} + \sum_{\mathbf{k}'} V_{\text{s}}(|\mathbf{k} - \mathbf{k}'|) \widetilde{\chi}(k',\omega) \right]\,. \tag{C.12}$$

The interband energy $\varepsilon_{\text{eh}}(k)$ is given by equation (4.20). The Coulomb potential V_{s} is screened due to the high carrier density present in the quantum-well. This plasma screening is computed here using a single plasmon-pole approximation[5] for the longitudinal dielectric function. Evaluating the result of equation (C.12)

at $\omega = \omega_{\text{cav}}$ yields $\chi(k,t) = \widetilde{\chi}(k, \omega_{\text{cav}})$ at time t given the non-equilibrium carrier distributions at that time. Technically the computation is performed by replacing

$$\frac{1}{\mathscr{A}} \frac{1}{(2\pi)^2)} \sum_{\mathbf{k}} \rightarrow \int_0^\infty dk k \int_0^{2\pi} d\phi \tag{C.13}$$

in equation (C.12) and solving the resulting integral equation using matrix computation techniques.[66] Having obtained $\chi(t) = \sum_{\mathbf{k}} \chi(k,t)$ the gain (C.11) and the time evolution of the intensity can be computed.

The carrier dynamics due to the coherent intracavity field is also determined by $\chi(k,t)$, as follows from equation (4.22),

$$\frac{\partial}{\partial t} f_{\text{e/h}}(t) \bigg|_{\text{stim}} = 2\,\text{Im}\Big[\big(d_{\text{cv}} + \sum_{\mathbf{k}'} V_{\text{s}}(|\mathbf{k} - \mathbf{k}'|) \chi(k',t) \big)^* \chi(k,t) \Big] I(t). \tag{C.14}$$

C.2.3. Spontaneous Contributions

It remains to determine the spontaneous contributions which cannot be derived in the framework of Maxwell's equations. We use here simplified rate-equation forms of a quantum treatment of the microlaser.[51,52] The spontaneous recombination is described by

$$\frac{\partial}{\partial t} f_{\text{e/h}}(k,t) \bigg|_{\text{spont}} = \frac{f_{\text{e}}(k)\, f_{\text{e}}(k)}{\tau_{\text{spont}}} \tag{C.15}$$

where the spontaneous decay rate $\tau_{\text{spont}}(\mathbf{k}) \equiv \tau_{\text{spont}}$ has been assumed to be k independent. That is, we have lumped together the Coulomb corrections of the spontaneous recombination into an effective spontaneous decay constant. The spontaneous emission into the cavity mode is given by

$$\frac{\partial}{\partial t} I(t) \bigg|_{\text{spont}} = \frac{\beta}{\tau_{\text{spont}}} \sum_{\mathbf{k}} \frac{\gamma}{(\hbar\omega - \varepsilon_{\text{eh}}(k))^2 + \gamma^2} f_{\text{e}}(k)\, f_{\text{h}}(k) \tag{C.16}$$

where $1 - \beta$ models the fraction of the total emission into non-lasing modes. In the numerical evaluations we have used $\tau_{\text{spont}} = 800\,\text{ps}$, $\beta = 10^{-3}$, and $\gamma = 5 E_{\text{B}}$.

Bibliography

[1] K. Cho, editor, *Excitons*, Springer, New York, 1979.

[2] E. I. Rashba and M. D. Sturge, editors, *Excitons*, volume 2 of *Modern Problems in Condensed Matter Science*, North-Holland, Amsterdam, 1982.

[3] A. Stahl and I. Balslev, *Electrodynamics of the Semiconductor Band Edge*, volume 110 of *Springer Tracts in Modern Physics*, Springer, New York, 1987.

[4] P. Halevi, *Spatial Dispersion in Solids and Plasmas*, North-Holland, Amsterdam, 1992.

[5] H. Haug and S. W. Koch, *Quantum Theory of the Optical and Electronic Properties of Semiconductors*, World Scientific, Singapore, 3rd edition, 1995.

[6] J. J. Hopfield, Phys. Rev. **112**, 1555 (1958).

[7] J. Tignon, T. Hasche, D. S. Chemla, H. C. Schneider, F. Jahnke, and S. W. Koch, unpublished, 1999.

[8] S. I. Pekar, Sov. Phys. JETP **6**, 785 (1958).

[9] K. Henneberger, Phys. Rev. Lett. **80**, 2889 (1998).

[10] C. S. Ting, M. J. Frankel, and J. L. Birman, Solid State Commun. **17**, 1285 (1975).

[11] M. Kira, I. Tittonen, and S. Stenholm, Phys. Rev. B **52**, 10972 (1995).

[12] M. Oestreich et al., Solid State Commun. **108**, 753 (1998).

[13] S. Hallstein et al., Phys. Rev. B **56**, R7076 (1997).

[14] H. C. Schneider, F. Jahnke, S. W. Koch, J. Tignon, T. Hasche, and D. S. Chemla, unpublished, 1999.

[15] L. Schultheis et al., in *Excitons in Confined Systems*, edited by R. Del Sole, A. D'Andrea, and A. Lapiccirella, page 110, Springer, New York, 1987.

[16] D. F. Nelson and B. Chen, Phys. Rev. Lett. **83**, 1263 (1999).

[17] R. Zeyher, Phys. Rev. Lett. **83**, 1264 (1999).

[18] K. Henneberger, Phys. Rev. Lett. **83**, 1265 (1999).

[19] S. W. Koch, F. Jahnke, and W. W. Chow, Semicond. Sci. Technol. **10**, 739 (1995).

[20] V. M. Axt and A. Stahl, Solid State Commun. **77**, 189 (1991).

[21] K. Victor, V. M. Axt, and A. Stahl, Z. Phys. B **92**, 35 (1993).

[22] S. Bischoff, A. Knorr, and S. W. Koch, Phys. Rev. B **55**, 7715 (1997).

[23] K. Cho, J. Phys. Soc. Japan **55**, 4113 (1986).

[24] H. Ishihara and K. Cho, Phys. Rev. B **41**, 1424 (1990).

[25] A. D'Andrea and R. Del Sole, Phys. Rev. B **41**, 1413 (1990).

[26] B. Chen and D. F. Nelson, Phys. Rev. B **48**, 15372 (1993).

[27] F. Steininger, A. Knorr, T. Stroucken, P. Thomas, and S. W. Koch, Phys. Rev. Lett. **77**, 550 (1996).

[28] R. Binder and S. W. Koch, Progress in Quantum Electronics **19**, 307 (1995).

[29] Y. Z. Hu, R. Binder, and S. W. Koch, Phys. Rev. B **47**, 15679 (1993).

[30] L. Lepetit, G. Chériaux, and M. Joffre, J. Opt. Soc. Am. B **12**, 2467 (1995).

[31] J. Perina, *Coherence of Light*, Reidel, Dordrecht, 2nd edition, 1985.

[32] P. Meystre and M. Sargent III, *Elements of Quantum Optics*, Springer, New York, 2nd edition, 1991.

[33] J. J. Hopfield and D. G. Thomas, Phys. Rev. **132**, 563 (1963).

[34] V. M. Agranovich, V. E. Kravtsov, T. A. Leskova, A. G. Mal'shukov, G. Hernández-Cocoletzi, and A. A. Maradudin, Phys. Rev. B **29**, 976 (1984).

[35] R. Ruppin and R. Englman, Phys. Rev. Lett. **53**, 1688 (1984).

[36] R. Zeyher, J. L. Birman, and W. Brenig, Phys. Rev. B **6**, 4613 (1972).

[37] R. Zeyher, Polaritons in a bounded spatially dispersive medium, in *Recent Developments in Condensed Matter Physics*, edited by J. T. Devreese, volume I, page 807, Plenum Press, 1981.

[38] A. Tredicucci, Y. Chen, F. Bassani, J. Massies, C. Deparis, and G. Neu, Phys. Rev. B **47**, 10348 (1993).

[39] F. Bassani, M. Dressler, and G. Czajkowski, Nuovo Cimento D **20**, 1355 (1998).

[40] J. B. Stark, W. H. Knox, D. S. Chemla, W. Schäfer, S. Schmitt-Rink, and C. Stafford, Phys. Rev. Lett. **65**, 3033 (1990).

[41] C. Stafford, S. Schmitt-Rink, and W. Schäfer, Phys. Rev. B **41**, 10000 (1991).

[42] P. Pfeffer and W. Zawadzki, Phys. Rev. B **41**, 1561 (1990).

[43] P. Pfeffer and W. Zawadzki, Phys. Rev. B **53**, 12813 (1996).

[44] C. Hermann and C. Weisbuch, Phys. Rev. B **15** (1977).

[45] O. Madelung, M. Schulz, and H. Weiss, editors, *Landolt-Börnstein Tables*, volume 17a, Springer, Berlin, 1982.

[46] V. L. Vekua, R. I. Dzhioev, B. P. Zakharachenya, E. L. Ivchenko, and V. G. Fleĭsher, Sov. Phys. JETP **39**, 879 (1975).

[47] M. Kira, F. Jahnke, W. Hoyer, and S. W. Koch, Progress in Quantum Electronics (1999), accepted for publication.

[48] M. Kira, F. Jahnke, and S. W. Koch, Phys. Rev. Lett. **81**, 3263 (1998).

[49] L. J. Sham, J. Phys.: Condens. Matter **5**, A51 (1993).

[50] R. M. Hannak, M. Oestreich, A. P. Heberle, W. W. Rühle, and K. Köhler, Solid State Commun. **93**, 313 (1995).

[51] H. C. Schneider, F. Jahnke, and S. W. Koch, Quantum Semiclass. Opt. **9**, 693 (1997).

[52] F. Jahnke and S. W. Koch, Phys. Rev. A **52**, 1712 (1995).

[53] F. Jahnke, H. C. Schneider, and S. W. Koch, Appl. Phys. Lett. **69**, 1185 (1996).

[54] M. Hilpert et al., Appl. Phys. Lett. **71**, 3761 (1997).

[55] F. Jahnke and S. W. Koch, Optics Lett. **18**, 1438 (1993).

[56] S. Hallstein, *Spin-Quantenschwebungen in Halbleitern*, PhD thesis, Max-Planck-Institut für Festkörperforschung, Stuttgart, 1997.

[57] M. Oestreich et al., Festkörperprobleme (Advances in Solid-State Physics) **37**, 245 (1998).

[58] G. Khitrova, H. M. Gibbs, F. Jahnke, M. Kira, and S. W. Koch, Rev. Mod. Phys. **71** (1999).

[59] J. M. Luttinger and W. Kohn, Phys. Rev. **97**, 869 (1955).

[60] J. M. Luttinger, Phys. Rev. **102**, 1030 (1956).

[61] S. L. Chuang, *Physics of Optoelectronic Devices*, Wiley, New York, 1995.

[62] C. Leforestier et al., J. Comput. Phys. **94**, 59 (1991).

[63] W. F. Ames, *Numerical Methods for Partial Differential Equations*, Computer Science and Scientific Computing, Academic Press, San Diego, 3rd edition, 1992.

[64] W. Gropp, E. Lusk, and A. Skjellum, *Using MPI*, MIT Press, Cambridge, MA, 1994.

[65] E. F. Van de Velde, *Concurrent Scientific Computing*, volume 16 of *Texts in Applied Mathematics*, Springer, New York, 1994.

[66] W. W. Chow, S. W. Koch, and M. Sargent III, *Semiconductor-Laser Physics*, Springer, New York, 1994.

Danksagung

An dieser Stelle möchte ich mich zuerst bei meinen Eltern bedanken und ihnen diese Arbeit widmen.

Ich danke herzlich meinem Doktorvater Professor Stephan Koch für die Förderung dieser Arbeit und viele, wichtige Diskussionen. Mit Dr. Frank Jahnke, „meinem“ Privat-Dozenten, habe ich während meiner gesamten Zeit in der Marburger Halbleitertheorie-Gruppe freundschaftlich zusammengearbeitet. Seiner ständigen Bereitschaft, physikalischen Problemen im Detail auf den Grund zu gehen, verdankt diese Arbeit mehr, als ich im Text hervorheben kann. Professor Peter Thomas, Dr. Andreas Knorr und Dr. Mackillo Kira gebührt mein Dank, daß sie sich jederzeit bereitwillig in hilfreiche physikalische Diskussionen verwickeln ließen.

Den Experimentatoren Dr. Michael Oestreich, Daniel Hägele und Professor Wolfgang Rühle aus Marburg sowie Dr. Sascha Hallstein aus Stuttgart danke ich für die reibungslose Zusammenarbeit bei den Mikrolaser-Projekten mit und ohne Magnetfeld. Professor Rühle danke ich zudem für die Übernahme des Zweitgutachtens.

Die Ergebnisse zur Theorie der Polariton-Propagation wären nicht zustande gekommen ohne den intensiven Austausch mit Dr. Jerome Tignon (Paris), Dr. Tom Hasche (Dresden) und Professor Daniel Chemla (Berkeley), wofür ich mich herzlich bedanke.